Doping Homogeneity of Paramagnetic Ions Studied via NMR Visibility

Dissertation

zur Erlangung des Grades

eines Doktors der Naturwissenschaften

vorgelegt von

Wenyu Li, M. Sc.

eingereicht bei der Naturwissenschaftlich-Technischen

Fakultät der Universität Siegen

Siegen 2020

Betreuer und erster Gutachter

Prof. Dr. Jörn Schmedt auf der Günne

Universität Siegen

Zweiter Gutachter

Prof. Dr. Leo van Wüllen

Universität Augsburg

Tag der mündlichen Prüfung

23. Juni 2020

Erklärung

Ich erkläre hiermit an Eides statt, dass ich die vorliegende Arbeit ohne unzulässige Hilfe Dritter und ohne Benutzung anderer, nicht angegebener Hilfsmittel angefertigt habe. Die aus anderen Quellen direkt oder indirekt übernommenen Daten und Konzepte sind unter Angabe der Quelle gekennzeichnet. Die Arbeit wurde bisher weder im In- noch im Ausland in gleicher oder ähnlicher Form einer anderen Prüfungsbehörde vorgelegt. Es wurden keine Dienste eines Promotionsvermittlungsinstituts oder einer ähnlichen Organisation in Anspruch genommen.

Siegen, den 04.05.2020

TO MY FAMILY AND FRIENDS

Acknowledgments

Table of contents

Table of abbreviations

A	area
A_{con}	Fermi-contact coupling constant
B	magnetic field
CL	cathodoluminescence
δ	chemical shift
δ_{iso}	isotropic chemical shift
EPR	electron paramagnetic resonance
EDX	energy dispersive X-ray spectroscopy
FID	free induction decay
FWHM	full width at half-maximum
$\Delta\nu_{1/2}$	spectral linewidth at FWHM
γ	gyromagnetic ratio
h	Planck constant
$\hbar$	reduced Planck constant, $\hbar = h/2\pi$
IUPAC	international union of pure and applied chemistry
k	Boltzmann constant
Ln	lanthanide
$M_0,\ M_1,\ M_2$	zeroth moment, first moment, second moment
M_{eq}	macroscopic magnetization
MAS	magic angle spinning
NMR	nuclear magnetic resonance
ω_0	Larmor frequency
Ξ	frequency ratio in per cent
μ	magnetic moment
μ_{B}	Bohr magneton
ppm	parts per million
r_0	blind sphere radius
RE	rare earth
SBM	Solomon–Bloembergen–Morgan theory
SEM	scanning electron microscopy
τ	correlation time

t	time
T	temperature
T_1	nuclear longitudinal relaxation time
T_2	nuclear transverse relaxation time
$T_{1\,e}$	electron longitudinal relaxation time
$T_{2\,e}$	electron transverse relaxation time
TMS	tetramethylsilane
XPS	X-ray photoelectron spectroscopy
XRD	X-ray diffraction

Abstract

In this work a solid state NMR methodology based on the "NMR visibility" and the concept of NMR blind sphere was established. This method can be used for the study of doping homogeneity of paramagnetic ions, and the resulting "NMR homogeneity" was shown to correlate to the functional material performance. The method has been successfully applied in the model sample series and NMR blind sphere radii for paramagnetic dopants could be obtained.

First, in section 3.1, the correlation between NMR signal and the dopant distribution was established, via the development of the "NMR visibility" and the NMR visibility function $f(x)$ curve, which is the visibility f as a function of the doping level x. Such "NMR visibility" was defined as the molar peak area of paramagnetic doped sample normalized by that of the diamagnetic host. The NMR visibility model was tested on $Sr_{1-x}Eu_xH_2$ sample series and the formula of the NMR visibility function for homogeneous sample series was developed to be $f(x) = \exp(-ar_0^3 x)$, where the r_0 is the NMR blind sphere radius and a is a number density parameter related to the host. The visibility curve calculated from ^{1}H MAS NMR experimental data was consistent with the visibility function $f(x)$ as well as the results calculated by a home-written Fortran90 program based on a random distribution model.

Subsequently, in section 3.2, the method was tested in different model compounds series including hopeite $(Zn_{1-x}Mn_x)_3(PO_4)_2 \cdot 4H_2O$ with the paramagnetic dopant Mn^{2+} and NMR nuclei ^{1}H and ^{31}P, $Sr_{1-x}Eu_xGa_2S_4$ with the paramagnetic dopant Eu^{2+} and NMR nucleus ^{71}Ga, and monazite $La_{1-x}Ln_xPO_4$ with paramagnetic dopants Ln^{3+} (Ln = Nd, Gd, Dy, Ho, Er, Tm, Yb) and NMR nucleus ^{31}P. For all homogeneously doped sample series the NMR visibility method could be applied and the NMR blind sphere radii were obtained, which lay typically in the Å to nm range. Additionally, the theoretical study of the NMR blind sphere radii was shown.

In section 3.3, the NMR visibility function was shown to be able to differentiate a heterogeneous doping scenario from a homogeneous one, as for heterogeneously doped samples a deviation from the visibility function was observed. The term "NMR homogeneity" was thus introduced for homogeneous samples tested by the NMR visibility method. Samples with higher NMR homogeneity were also shown to be positively correlated to better luminescence performance, including intensity and decay time.

Furthermore, in section 3.4, the NMR visibility function was extended to co-doped systems including $La_{1-x-y}Gd_xDy_yPO_4$, $La_{1-x-y}Nd_xTm_yPO_4$ and $La_{1-x-y}Nd_xHo_yPO_4$. For $La_{1-x-y}Nd_xHo_yPO_4$, a 3D NMR visibility map instead of the 2D NMR visibility curve was developed. As the radii of NMR blind spheres were in Å to nm range, the NMR homogeneity determined by the NMR visibility model was also on a similar length scale. Together with SEM-EDX mapping and SEM-CL techniques, co-doping homogeneity or heterogeneity can be systematically studied from Å to μm range.

Overall, the NMR visibility method has been shown to be useful both for theoretical NMR blind sphere studies and for applications in paramagnetic systems as long as NMR nuclei are present.

Zusammenfassung

In dieser Arbeit wurde eine Festkörper-NMR-Methode, welche auf der „NMR-Sichtbarkeit" und dem Konzept der NMR-Blindkugeln basiert, etabliert. Dieses Verfahren kann für die Untersuchung der Homogenität der Dotierung paramagnetischen Ionen verwendet werden. Es wurde gezeigt, dass die resultierende „NMR-Homogenität" mit der Effizienz des funktionellen Materials korreliert. Das Verfahren wurde erfolgreich in einer Modellproben-Serie angewendet und Blindkugel-Radien für paramagnetische Dotierstoffe konnten erhalten werden.

In Abschnitt 3.1 wurde die Korrelation zwischen NMR-Signal und der Dotierungsverteilung etabliert, indem die „NMR-Sichtbarkeit" und die NMR-Sichtbarkeitsfunktion-$f(x)$-Kurve, welche die Sichtbarkeit f als Funktion des Dotierniveaus x beschreibt, entwickelt wurde. Diese „NMR-Sichtbarkeit" wurde als die molare Peakfläche der paramagnetisch dotierten Probe definiert, welche durch die des diamagnetischen Wirts normalisiert ist. Das NMR-Sichtbarkeits-Modell wurde an $Sr_{1-x}Eu_xH_2$-Probenserien getestet und die Formel der „NMR-Sichtbarkeits"-Funktion für homogene Probenserien wurde als $f(x)=\exp(-ar_0^3 x)$ entwickelt, wobei r_0 den Radius der NMR-Blindkugeln und a einen Parameter der Zahlendichte, welcher sich auf den Wirt bezieht, beschreibt. Die aus experimentellen ^{1}H-MAS-NMR-Daten berechnete Sichtbarkeitskurve war konsistent mit der Sichtbarkeitsfunktion $f(x)$ sowie mit den Ergebnissen aus Berechnungen mit einem selbst geschriebenen Fortran90-Programm, welches auf einem Zufallsverteilungsmodell basiert.

Anschließend wurde in Abschnitt 3.2 das Verfahren in verschiedenen Modellverbindungs-Reihen, einschließlich Hopeit $(Zn_{1-x}Mn_x)_3(PO_4)_2 \cdot 4H_2O$ mit dem paramagnetischen Dotierstoff Mn^{2+} und den NMR-Kernen ^{1}H und ^{31}P, $Sr_{1-x}Eu_xGa_2S_4$ mit Eu^{2+} und dem NMR-Kern ^{71}Ga, und Monazit $La_{1-x}Ln_xPO_4$ mit Ln^{3+} (Ln = Nd, Gd, Dy, Ho, Er, Tm, Yb) und dem NMR-Kern ^{31}P. Für alle homogen dotierte Probenserien konnte die NMR-Sichtbarkeits-Methode angewendet werden, und die Radien der NMR-Blindkugeln, welche typischerweise im Å bis nm-Bereich liegen, wurden erhalten. Zusätzlich wurde die theoretische Untersuchung der Radien von NMR-Blindkugeln gezeigt.

In Abschnitt 3.3 wurde gezeigt, dass die NMR-Sichtbarkeitsfunktion ein heterogenes von einem homogenen Dotierungsszenario unterscheiden kann, da bei heterogen dotierten Proben eine Abweichung von der Sichtbarkeitsfunktion beobachtbar war. Der Begriff „NMR-Homogenität" wurde daher für homogene Proben eingeführt, welche mit der NMR-Sichtbarkeits-Methode getestet wurden. Es wurde auch gezeigt, dass Proben mit höherer NMR-Homogenität bessere Lumineszenzleistung zeigen, einschließlich Intensität und Abklingzeit.

Darüber hinaus wurde in Abschnitt 3.4 die NMR-Sichtbarkeitsfunktion auf co-dotierte Systeme erweitert, einschließlich $La_{1-x-y}Gd_xDy_yPO_4$, $La_{1-x-y}Nd_xTm_yPO_4$ and $La_{1-x-y}Nd_xHo_yPO_4$. Für $La_{1-x-y}Nd_xHo_yPO_4$, wurde anstelle der 2D-NMR-Sichtbarkeitskurve eine 3D-NMR-Sichtbarkeitskarte entwickelt. Da die Radien der NMR-Blindkugeln im Å- bis nm-Bereich erschienen, lag die durch das NMR-Sichtbarkeits-Modell bestimmte NMR-Homogenität ebenfalls auf einer ähnlichen Längenskala. Zusammen mit SEM-EDX-Mapping- und SEM-CL-Techniken wurde gezeigt, dass die Homogenität oder Heterogenität von Co-Dotierungen systematisch vom Å- bis zum µm-Bereich untersucht werden kann.

Insgesamt hat sich gezeigt, dass die NMR-Sichtbarkeits-Methode sowohl für theoretische Studien der NMR-Blindkugeln als auch für Anwendungen in paramagnetischen Systemen nützlich ist, solange NMR-Kerne vorhanden sind.

1   Introduction

The aim of this work is to establish a NMR methodology to investigate the doping homogeneity of paramagnetic ions. Doping is one of the most versatile tools to influence properties of solids as it introduces defects and tunes charge carrier concentrations.[1] The standard definition of doping according to the IUPAC[2] refers to an action of adding a small amount of foreign atoms (dopants) to form a solid solution in the lattice. In materials science, doping is used rather uncritically and in general refers to an impurity effect that influences the defect structure without changing the ground structure.[1] Doping is not restricted to one kind of dopant, instead, it is possible to incorporate more than one species. For example, co-doping is a strategy which potentially enhances the solubility of dopants and improves the stability of desired defects. As a result, the dopant populations, electronic properties and magnetic properties are effectively tuned.[3]

Among various choices of dopant species, the rare earth (RE) elements are of great importance, as they find various applications[4,5] in mature markets ranging from electronics[6] such as cellphones and computers, optical materials[7] such as lasers and phosphors, over medical science such as magnetic resonance imagery (MRI)[8] contrast agents, to the field of renewable energy[9,10] such as magnets in wind turbines. In recent years, the RE elements have also shown large potential in modern advanced technologies for example in quantum nanophotonics,[11,12] in electrode materials for advanced energy storage[13] as well as in frontier biological discoveries.[14] Typical examples of RE doped solid functional materials[4,15] are glass lasers[16] and luminescent materials.[4,17] While playing important roles in numerous fields with large consumption, the RE elements are in fact non-renewable natural resources. According to the report from the European union, the RE elements is in the group of critical minerals[18] and its import reliance is 100%.[19] Therefore, the rational utilization of RE elements is an important issue and should be addressed.[20]

As by adding only a small amount of RE elements aimed properties can be tuned and controlled,[1] doping is an effective strategy for making use of RE resources,

as long as the dopants are well implemented in the host as designed, which leads to the question of dopant distribution. It is of particular interest because where and how the dopants involved in the material can make dramatic difference in the material property.[1,3,21] Taking luminescent materials for example, good spacial separation of dopants is often required to avoid or alleviate concentration quenching[21–23] in order to achieve optimized luminescent performance.[21,24,25] One of the simple and effective solutions is homogeneous doping,[21,24] which means ensuring spatial separation while saving the consumption and making the best use of RE elements.

As for the studies by solid state nuclear magnetic resonance (NMR), which is the main research technique in this work, the paramagnetic lanthanide ions from the RE group are also good candidates for the study of paramagnetic NMR effects. This is because the 4f electrons are well shielded by 5s and 5p electrons and not available for covalent bonding, which leads to smaller crystal field effects for lanthanides as compared to transition metal ions.[26–28] Therefore, the NMR research on the dopant distribution with RE elements is both of academic value and practical significance.

Tuning of material properties by doping can be achieved in homogeneous or designed heterogeneous way.[1] In both ways the determination of dopant distribution is essential. However, in actual usage the circumscription for homogeneity or heterogeneity is rather vague, because homogeneity is not a unique metric unit. Therefore, it is important to first clarify the concept of "homogeneity".

The IUPAC gold book defines the term "homogeneity"[29] as "the degree to which a property or a constituent is uniformly distributed throughout a quantity of material". Accordingly, a material can be both homogeneous and heterogeneous, with respect to different length scales. For example, a piece of clear window glass is often taken for granted as homogeneous by naked eyes in centimeters or meters, but under electron microscope phase separations can be detected and in atomic scale glass lacks the long-range periodic arrangement.[30] Therefore,

homogeneity or heterogeneity should always be clarified with respect to a specific length or volume.

Various techniques contribute to the study of homogeneity, for example diffraction methods,[31] electron microscopy[32] with energy dispersive X-ray analysis (EDX),[33] X-ray photoelectron spectroscopy (XPS)[34] and so forth. However, it turned out to be nontrivial to ''prove'' doping homogeneity, instead, the usual approach is to disprove heterogeneity on different length scales. To name a few examples, SEM, SEM-EDX and SEM-CL provide information typically on μm or sub-μm scale[32,35,36] and TEM on nm to Å (or atomic) scale.[37] The studied sample volumes could also be different, for example laboratory powder XRD and neutron diffraction sense bulk properties,[31] while in comparison, techniques such as XPS[34] and EDX[38] are more surface sensitive,[32,34,39] which means smaller analyzed volume. Consequently, same sample could appear to be homogeneous or inhomogeneous depending on the chosen technique.

As for magnetic resonance, there is the option of directly focusing on the paramagnetic centers, as for example electron paramagnetic resonance (EPR) and electron spin echo envelope modulation (ESEEM), or the option of studying the diamagnetic host, such as NMR. Magnetic resonance techniques such as NMR[40–55] and EPR[56,57] have the characteristics that bulk properties as well as low doping level can be studied on the atomic range, which is nontrivial.

Solid state NMR has been used to investigate the paramagnetic dopant distribution of a single kind of dopant (''mono-doped'') in different ways. For example, the T_1 relaxation times of a series of doped samples[51,50,42] can be used to study the doping homogeneity based on the exponential dependence of T_1 on doping level with the factor -1 or $-4/3$, depending on whether spin diffusion is present or not.[49] Besides, a NMR T_1-T_2 correlation map[52] was also shown to be useful in studying a paramagnetic site distribution at the surface of porous materials. In addition, the line broadening or change of lineshape[42,40,41] can be used as indication of homogeneity of heterogeneity. Also, the spinning sideband

envelopes can be sensitive to the location of paramagnetic dopants in batteries.[48] For example, ^{6}Li MAS NMR spinning sideband manifolds[47] and shifts[45] are sensitive to the nearest coordination sphere of Mn ions. Last but not least, in glasses, rotational-echo double resonance (REDOR) is shown to be a useful tool to determine the homogeneous distribution of diamagnetic dopants, and the monotonic shift of center of gravity with increasing doping level is also indicative of a random dopant distribution.[56,57]

Although it is commonly assumed that the homogeneity obtained by magnetic resonance corresponds to the distance range of the studied interaction, for the previous methods the length scale by numerical values was not explicitly stated or highlighted. In addition, the majority of the previous studies focus on the relaxation,[49–52] shift,[45,46] lineshape[40–44] or sideband manifolds[47,48] analysis, which naturally requires a reasonably good signal visibility. At this stage, a series of ensuing questions have motivated this research. Is there a direct connection between the doping homogeneity and the observed peak area? If the signal loss is severe, which can be possible for paramagnetic systems, could the doping homogeneity still be studied? Is it possible to make use of the "lost signals" to this end?

The invisibility of NMR signal originated from the signal quenching phenomenon inside a blind sphere, which refers to a volume around a paramagnetic ion inside which no NMR signal can be observed.[58] Previous studies related to blind spheres have been mainly focused on metalloproteins[27,59–64] and magnetic systems[65–69] in which different terminologies are used. For example, for the studies of metalloproteins by solution NMR and dynamic nuclear polarization (DNP), the terms of "blind sphere" or "quenching/bleaching" are often used, as the blind sphere plus the detectable paramagnetic effects are useful information for structure constrains.[27,58] For the studies of magnetism the term "wipeout" or "critical radius" has been used and the research interests lean towards relaxation rate and temperature dependence, as such studies gives hint to the stripe order.[70] To the best of my knowledge, the usage of blind spheres on doping homogeneity study especially in inorganic systems has not been published before.

Based on the previous motivations with respect to doping and the questions with respect to NMR methods, the aim of this work was to establish a novel NMR methodology for doping homogeneity analysis of paramagnetic species. Such method was expected to fulfill the following requirements. Firstly, it should be applicable for paramagnetic dopants especially RE dopants. Secondly, via the method, homogeneous doping scenario could be differentiated from heterogeneous ones. In particular, not only the visible signal but also the invisible signal from NMR nuclei inside blind spheres should be made use of. Thirdly, by applying this method, the homogeneity related length scale could be specified and in the end the correlation between the determined homogeneity and the material performance should be checked.

2 Theoretical Background

2.1 Solid State NMR Spectroscopy

Nuclear Magnetic Resonance (NMR) spectroscopy is an isotope specific technique, whose application heavily relies on the fact that the local magnetic fields experienced by the nuclei are sensitive to the local electronic environments.[71] In this work typical NMR parameters involved are: isotropic chemical shift δ_{iso}, which indicates signal position; spin-lattice relaxation time T_1 and peak area A, which are useful information for NMR quantification; and linewidth $\Delta\nu_{1/2}$ that relates to second moment M_2 analysis of the lineshape.

2.1.1 Chemical Shift

In NMR, the magnetic fields experienced by the nuclei are sensitive to the local electronic environments.[71,72] The dependence of the nuclear Larmor frequency on the local electronic environment can be described as the chemical shift effect.[71,72] A standalone nucleus with nonzero nuclear spin should precess with an angular frequency ω_0 in external magnetic field B_0 (equation 2.1.1-1, with γ being the gyromagnetic ratio). ω_0 is the Larmor frequency and is nucleus specific.

$$\omega_0 = -\gamma B_0 \qquad (2.1.1\text{-}1)$$

When taking into account the electron clouds surrounding the nucleus, the external magnetic field will induce circular currents into the electron clouds, which generates an induced field B_{ind}. The local magnetic field that the nucleus with electron clouds experienced is then the effective magnetic field B_{eff}, which is the sum of B_{ind} and B_0 (equation 2.1.1-2).[71]

$$B_{eff} = B_0 + B_{ind} \qquad (2.1.1\text{-}2)$$

The strength of the induced field B_{ind} is linearly dependent on the external field

B_0 and the tensor which describes this linear dependence is the chemical shift tensor δ (equation 2.1.1-3).[71]

$$B_{ind} = \delta \cdot B_0 \qquad (2.1.1\text{-}3)$$

In diamagnetic material the magnitude of B_{ind} is much smaller than that of B_0, which makes the chemical shift a small value.[71] In paramagnetic materials, due to the presence of unpaired electrons, the corresponding shift can be large and is called the paramagnetic shift (or hyperfine shift).[71] In particular, the term Knight shift is usually used in metals and superconductors.[71] The paramagnetic part is further discussed in section 2.2.

The magnitude of the precession frequency ω_j of a nucleus j surrounded by electron clouds is proportional to the strength of effective magnetic field B_{eff} (equation 2.1.1-4).[71–73]

$$\omega_j = \gamma_j B_{eff} = \gamma_j \left(B_0 + B_{ind} \right) = \gamma_j B_0 \left(1 + \delta \right) \qquad (2.1.1\text{-}4)$$

The IUPAC defined the chemical shift δ for nucleus X as equation 2.1.1-5.[74,75]

$$\delta_{X,sample} = \frac{\nu_{X,sample} - \nu_{X,reference}}{\nu_{X,reference}} \qquad (2.1.1\text{-}5)$$

The $\nu_{X,sample}$ and $\nu_{X,reference}$ refer to the resonance frequency of nucleus X in sample and reference compound, respectively. For example, the reference compound for ^1H is tetramethylsilane(TMS) in dilute solution (volume fraction 1% in $CDCl_3$).

In some cases reference compounds for X are unavailable or hard to measure, thus IUPAC offers a conversion possibility between X and ^1H, using Ξ as the ratio of the X frequency to that of ^1H in TMS in the same magnetic field. Ξ is expressed as a percentage (equation 2.1.1-6).

$$\nu_{\mathrm{X,reference}} = \varXi \cdot \nu_{^1\mathrm{H,TMS}} \qquad (2.1.1\text{-}6)$$

In this way, chemical shift becomes a relative quantity which is field independent, which facilitates the comparisons among studies.

In solution, due to the fast averaging of anisotropic interactions, the chemical shift can be specified as an isotropic parameter.[71] In solids or liquid crystals, the chemical shift tensor can be described as a 3×3 matrix of real numbers. In the laboratory frame, its anisotropic contribution can be described by a rank two tensor with components δ_{ij}, i,j being x,y or z. By diagonalization of the chemical shift tensor, the isotropic chemical shift δ_{iso} can be obtained as a scalar quantity as one third of the trace or the average of three principle values in the diagonal.

2.1.2 Relaxation

In the absence of external magnetic field, the spins in a sample are a quantum mixture of "spin-up" and "spin-down" eigenstates which shows overall macroscopic magnetization of zero.[27] By bringing a sample into a static magnetic field, a spin population difference of energy levels following the Boltzmann law is induced, which results in a net nonzero magnetization along z axis.[27,71]

The return of the magnetization into thermal equilibrium from non-equilibrium conditions can be described with a set of rate equations.[71] The corresponding exponential time constants along z-axis (applied field direction) and in the xy-plane are called longitudinal relaxation time T_1 and transverse relaxation time T_2, respectively.[71] The corresponding relaxation rate constants T_1^{-1} and T_2^{-1} are R_1 and R_2, respectively. Such notation of nuclear relaxation also applies to electronic relaxation. For simplicity, the nuclear relaxation time constants are written as T_1 and T_2, while the electronic longitudinal and transverse relaxation times are denoted as T_{1e} and T_{2e}, respectively. Through the process of reaching thermal equilibrium from non-equilibrium conditions, energies are exchanged between the spin systems and the surroundings which were historically assumed

as lattices, therefore the T_1 is also named spin-lattice relaxation time.

To measure the relaxation times, perturbation of the naturally equilibrium state spin system is necessary and this is achieved by radio frequency (RF) pulses in NMR. A common way to measure T_1 is performing the saturation recovery experiment. The build up of magnetization along z-axis for such experiment can be written as equation 2.1.2-1.[71]

$$M_z(t) = M_{eq}\left(1 - e^{-t/T_1}\right) \tag{2.1.2-1}$$

The T_1 is not the time constant at which the magnetization reaches thermal equilibrium but $M_z \approx 63\% M_{eq}$. At $t \approx 5T_1$, M_z reaches approximately $99\% M_{eq}$. Therefore, a repetition delay of $5T_1$ is used for quantitative NMR measurements in this work.

The T_1 relates to the magnetization buildup along z-axis. On the other hand, T_2 corresponds to the exponential decay of magnetization in the xy-plane, whose cosine Fourier transformation gives a Lorentzian frequency function (equation 2.1.2-2) with spectral linewidth of $\Delta\nu_{1/2} = (\pi T_2)^{-1}$, which is the full width at half-maximum (FWHM) (equation 2.1.2-3).[27]

$$\int_0^\infty e^{-t/T_2}\cos(\omega t)\,\mathrm{d}t = \frac{T_2}{1 + \omega^2 T_2^2} \tag{2.1.2-2}$$

$$\Delta\nu_{1/2} = \frac{1}{\pi T_2} \tag{2.1.2-3}$$

2.1.3 NMR Signal and Peak Area

In mathematics, by performing a Fourier transform (FT), a function of time $f(t)$ can be transformed to a function of frequency $F(\omega)$ (equation 2.1.3-1).[73]

$$f(t) \overset{\text{FT}}{\longleftrightarrow} F(\omega) = \int_{-\infty}^{\infty} f(t) e^{-i\omega t} \mathrm{d}t \qquad (2.1.3\text{-}1)$$

In modern NMR the FT plays an important role because it helps to obtain the frequency domain signal from the detected time domain signal, which is the free induction decay (FID). For pulsed NMR experiments, the FID is sampled over the acquisition time t_{aq} point by point with the time interval of the dwell time t_{dw}. Assuming that N points have been collected, then $t_{\text{aq}} = Nt_{\text{dw}}$ and the frequency $\omega = 2\pi/t_{\text{aq}} = (1/\text{N})2\pi/t_{\text{dw}}$, the general formula of equation 2.1.3-1 can thus be written as equation 2.1.3-2.[73]

$$j = 0, \dots, N-1 \qquad k = 0, \dots, N-1$$

$$f_j \overset{\text{discrete FT}}{\longleftrightarrow} F_k = \frac{1}{N} \sum_{j=0}^{N-1} f_j e^{-i\omega kj t_{\text{dw}}} \qquad (2.1.3\text{-}2)$$

According to the integral relation that the value of a function at zero equals the integral over its Fourier transform, the corresponding formula for pulsed NMR can be written as equation 2.1.3-3.[73]

$$f(0) = \sum_{k=0}^{N-1} F_k \qquad (2.1.3\text{-}3)$$

This is of importance for the NMR quantification as well as the NMR visibility function method in this work, because the peak area is related to the intensity of first point of the FID (see section 3.2).

2.1.4 Lineshape Analysis

For Gaussian lineshapes, the zeroth, first and second moment can be calculated in turn according to equation 2.1.4-1, 2.1.4-2 and 2.1.4-3.[76–78] The $I(v)$ is the

lineshape function and v is the nuclear resonance frequency. The zeroth moment M_0, the first moment M_1 and the second moment M_2 are related to the peak area A, the isotropic chemical shift δ_{iso} and the line broadening, respectively.[79]

$$M_0 = \int\limits_{-\infty}^{\infty} I(v)\, dv = A \tag{2.1.4-1}$$

$$M_1 = \frac{1}{M_0} \int\limits_{-\infty}^{\infty} v\, I(v)\, dv = \delta_{iso} \tag{2.1.4-2}$$

$$M_2 = \frac{1}{M_0} \int\limits_{-\infty}^{\infty} (v - M_1)^2 I(v)\, dv \tag{2.1.4-3}$$

2.2 Paramagnetic NMR

The origin of paramagnetic NMR effects is the hyperfine interaction between the NMR nucleus and the unpaired electrons. The term "hyperfine" was named after the hyperfine splitting structure in the electron paramagnetic resonance (EPR).[28] The consequences of hyperfine interactions are typically categorized into hyperfine shift, paramagnetic relaxation enhancement (PRE) and residual dipolar coupling (RDC).[27,28] For inorganic solids in this thesis, the important ones are the hyperfine shift and paramagnetic relaxation, which can be sub-categorized into for example contact coupling (Fermi-contact interaction) or dipolar coupling (pseudocontact interaction).[27,28] A basic overview of such interactions are presented in the following subsections and the treatment of lanthanides is depicted in more details, as in this work the main subject is solids doped with lanthanide ions.

2.2.1 Hyperfine Shift

In the section 2.1.1, the chemical shift effect in diamagnetic materials was described. The induced magnetic field is rather small as compared to the external

field, therefore the magnitude of chemical shift is small.

On the other hand, in paramagnetic systems, due to the presence of unpaired electrons, the magnitude of hyperfine shift can be much larger. The origin of hyperfine shift corresponds to the coupling of nuclei to unpaired electrons, which have a much faster relaxation rate $1/T_{1e}$ than the nuclei relaxation rate $1/T_1$. As a result of such a time scale difference, a nucleus will "sense" not an electronic magnetic moment but rather the average of it.[28] Therefore, T_{1e} is important in paramagnetic NMR. Typical T_{1e} range is 10^{-8}-10^{-14} s.[28,80]

2.2.2 Paramagnetic Enhanced Relaxation

Dipolar, Curie-spin and Fermi-contact relaxation are in principle three possible contributions for paramagnetic relaxation enhancement (PRE).[27,28] For solids with negligible rotational motion of large molecules, Curie-spin relaxation can be neglected, therefore is not further discussed here.[27,28]

The general model for PRE in solution is the Solomon-Bloembergen-Morgan (SBM) theory.[81–84] The SBM theory uses the point-dipole assumption, takes into account only contact and dipolar interactions while neglecting cross correlation, and treats all correlation functions as exponential functions.[28] As Solomon published his work on the dipolar interaction[81] and Bloembergen and Morgan on contact mechanism[82–84], the Solomon mechanism and Bloembergen or Bloembergen-Morgan mechanism are often mentioned as the principal mechanisms of the dipolar hyperfine interaction, respectively.

2.2.3 Paramagnetic NMR for Lanthanides

The nomenclature of lanthanide elements refers to a group of 15 elements, namely La, Ce, Pr, Nd, Pm, Sm, Eu, Gd, Tb, Dy, Ho, Er, Tm, Yb and Lu.[85] Although according to the IUPAC red book[85] lanthanoid is preferred to lanthanide because the ending "ide" normally indicates a negative ion,[86] for consistency with most cited references as well as publications, in this thesis the terminology "lanthanide" is adopted.

The most common oxidation state for Ln ions is Ln^{3+} which have the electron

configuration of $4f^n$. The 4f electrons are well shielded by 5s and 5p electrons thus not available for covalent bonding and the crystal field effects are rather small as compared to transition metal ions.[26]

For lanthanide ions, the common model is the Bleaney's theory,[87,88] which was originally used to calculate the paramagnetic shifts due to lanthanide ions. Bleaney made the following assumptions[87]: first, the only ground manifold J (total angular momentum, which is the vector combination of S and the orbital angular momentum L) is occupied and its $2J+1$ levels are split by ligand field to an overall amount that does not exceed thermal energy kT; second, unpaired electron density in the 4f orbitals fits the point-dipole model; and third, the spin-orbit coupling effects are much larger than the ligand field effects. Instead of S, the J is used because unlike the transition metal ions, the spin-orbit interactions of lanthanides are large. The point-dipole model assumed in the Bleaney's theory was shown to be a fair approximation for distance larger than 8 Å but may break down at distance smaller than 4 Å.[28]

The general equations of the Bleaney's theory are equation 2.2.3-1, 2.2.3-2 and 2.2.3-3.[27,87] These equations emphasize on the isotropy of the Fermi-contact shift and the anisotropy of the pseudocontact shift (PCS), as the PCS depends on the susceptibility anisotropy.[27] The δ_{PCS} and δ_{con} refer to the pseudocontact and contact shifts, respectively. The g_J is the g-factor in lanthanide free ions, γ_I is the nuclear gyromagnetic ratio, μ_0 is the vacuum permeability and μ_B is the Bohr magneton. The D_x, D_y and D_z are components of the zero field splitting (ZFS) tensor $\boldsymbol{D}$. The $r,\ \vartheta$ and φ are the spherical coordinates of the nucleus with respect to $\boldsymbol{D}$. The reduced Planck constant $\hbar = h/2\pi$ (h is the Planck constant), and χ is the magnetic susceptibility without ligand field splitting. The k is the Boltzmann constant and T is the temperature. The A_{con} is the contact coupling constant, which is usually assumed to be a constant along a series of lanthanide complexes with the same ligand.[27] This may be extended to a doping series due to the analogy to lanthanide dopants in the same host (section 3.2).

$$g_J = 1 + \frac{J(J+1) - L(L+1) + S(S+1)}{2J(J+1)} \tag{2.2.3-1}$$

$$\delta_{\text{PCS}} = -\frac{\mu_0}{4\pi} \frac{g_J^2 \mu_B^2 J(J+1)(2J-1)(2J+3)}{60(kT)^2}$$
$$\times \frac{D_z(3\cos^2\theta - 1) + (D_x - D_y)\sin^2\theta\cos 2\phi}{r^3} \tag{2.2.3-2}$$

$$\delta_{\text{con}} = \frac{A_{\text{con}}}{\hbar} \frac{g_J(g_J - 1)\mu_B J(J+1)}{3\gamma_I kT} \quad \text{or} \quad \delta_{\text{con}} = \frac{1}{\mu_0} \frac{A_{\text{con}}}{\hbar} \frac{g_J - 1}{\gamma_I \mu_B g_J} \chi \tag{2.2.3-3}$$

For the isotropic Fermi-contact relaxation contribution, equation 2.2.3-4 and 2.2.3-5 hold for paramagnetic solutions, according to Bloembergen.[83,84] The correlation time $\tau_{\text{con}} = (\tau_e^{-1} + \tau_M^{-1})^{-1}$, where τ_e relates to the electronic relaxation time and τ_M is the chemical exchange correlation time. The variable ω_S is the electron Larmor frequency.

$$\frac{1}{T_1} = \frac{2}{3} J(J+1) \frac{A_{\text{con}}^2}{\hbar^2} \frac{\tau_{\text{con}}}{1 + \omega_S^2 \tau_{\text{con}}^2} \tag{2.2.3-4}$$

$$\frac{1}{T_2} = \frac{1}{3} J(J+1) \frac{A_{\text{con}}^2}{\hbar^2} \left(\tau_{\text{con}} + \frac{\tau_{\text{con}}}{1 + \omega_S^2 \tau_{\text{con}}^2} \right) \tag{2.2.3-5}$$

According to the Solomon mechanism, for dipole relaxation in solids, the nuclear relaxation time depends on the electronic relaxation time (equation 2.2.3-6 and 2.2.3-7).[50] With negligible dynamics or motion in solids, the correlation time τ is approximately equal to the electronic relaxation time. The ω_I, ω_S, γ_I and γ_S are the nuclear and electronic Larmor frequencies, and the nuclear and electronic gyromagnetic ratios, respectively. The variable r is the distance between NMR nuclei and the unpaired electrons that belong to the paramagnetic ion.

$$\frac{1}{T_1}=\left(\frac{\mu_0}{4\pi}\right)^2\frac{J(J+1)}{15}\frac{\hbar^2\gamma_I^2\gamma_S^2}{r^6}\times\left(\frac{6\,T_{1e}}{1+\omega_I^2\,T_{1e}^2}+\frac{14\,T_{2e}}{1+\omega_S^2\,T_{2e}^2}\right) \qquad (2.2.3\text{-}6)$$

$$\frac{1}{T_2}=\left(\frac{\mu_0}{4\pi}\right)^2\frac{J(J+1)}{15}\frac{\hbar^2\gamma_I^2\gamma_S^2}{r^6}\times\left(4\,T_{1e}+\frac{3\,T_{1e}}{1+\omega_I^2\,T_{1e}^2}+\frac{13\,T_{2e}}{1+\omega_S^2\,T_{2e}^2}\right) \qquad (2.2.3\text{-}7)$$

For lanthanide ions, the effective magnetic moment μ_{eff} is related to the main total angular momentum quantum number J as $\mu_{\text{eff}}^2=g_J^{\;2}\mu_B^2\,J(J+1)$,[26] therefore equation 2.2.3-6 and 2.2.3-7 can be rewritten into equation 2.2.3-8 and 2.2.3-9, respectively.

$$\frac{1}{T_1}=\left(\frac{\mu_0}{4\pi}\right)^2\frac{\gamma_I^2}{15}\frac{\mu_{\text{eff}}^2}{r^6}\times\left(\frac{6\,T_{1e}}{1+\omega_I^2\,T_{1e}^2}+\frac{14\,T_{2e}}{1+\omega_S^2\,T_{2e}^2}\right) \qquad (2.2.3\text{-}8)$$

$$\frac{1}{T_2}=\left(\frac{\mu_0}{4\pi}\right)^2\frac{\gamma_I^2}{15}\frac{\mu_{\text{eff}}^2}{r^6}\times\left(4\,T_{1e}+\frac{3\,T_{1e}}{1+\omega_I^2\,T_{1e}^2}+\frac{13\,T_{2e}}{1+\omega_S^2\,T_{2e}^2}\right) \qquad (2.2.3\text{-}9)$$

From the formula of dipolar relaxation, it may be speculated that the r_0 should correspond to the γ_I and μ_{eff} as $r_0\propto\sqrt[3]{\gamma_I}$ and $r_0\propto\sqrt[3]{\mu_{\text{eff}}}$, on conditions that: if a critical dipolar relaxation rate related to blind sphere exists, and if the electron relaxation times are within similar range for the lanthanide dopants (section 3.2). Similar distance dependence of shifts and relaxation rates have been studied but only outside of the blind spheres.[27]

3 Peer-to-peer Reviewed Articles

3.1 Homogeneity of Doping with Paramagnetic Ions by NMR

Wenyu Li, Vinicius R. Celinski, Johannes Weber, Nathalie Kunkel, Holger Kohlmann and Jörn Schmedt auf der Günne

Contribution to the manuscript:

Based on the discussions and conceptual guidance from Jörn Schmedt auf der Günne, the model development and all NMR related data analysis were done by me. The NMR quantification process including mixing sample with standard compound, weighing on microbalance and rotor packing in the glove box was done by me. The full echo ^{1}H MAS NMR spectra of packed rotors were acquired by Vinicius R. Celinski in Munich with access to a 500 MHz NMR spectrometer. The Fortran90 based computer programs was written by me with help from Johannes Weber. The synthesis and Rietveld refinement of $Sr_{1-x}Eu_xH_2$ samples were done by Nathalie Kunkel in the group of Holger Kohlmann. This paper was drafted by me and perfected by Jörn Schmedt auf der Günne.

CrossMark
←click for updates

Homogeneity of doping with paramagnetic ions by NMR†

Wenyu Li,[a] Vinicius R. Celinski,[a] Johannes Weber,[a] Nathalie Kunkel,[b] Holger Kohlmann[c] and Jörn Schmedt auf der Günne*[a]

In NMR, paramagnetic dopants change the relaxation behavior and the chemical shift of the nuclei in their immediate environment. Based on the concept that the "immediate environment" in a diamagnetic host material can be described as a sphere with radius r_0, we developed a function for the fraction of unperturbed nuclei (the fraction of nuclei outside the sphere) which gives a link between the effective radius and the doping concentration. In the case of a homogeneous doping scenario a characteristic dependence is observed in both theory and experiment. We validated the model on a sample series where paramagnetic Eu(II) ions are doped into crystalline SrH_2. The fraction of unperturbed nuclei was determined from the ^1H NMR signal and follows the predicted curve for a homogeneous doping scenario where the radius r_0 is 17 Å.

Introduction

Doping by paramagnetic ions enables the functionalization of inorganic materials such as phosphors[1–5] and semiconductors.[6–8] For example, one type of phosphor-converted white-light LED is realized with a diamagnetic $SrSi_2O_2N_2$ host doped with only 2% of Eu which yields quantum efficiencies as high as 91%.[9] In the case of long lasting phosphors (LLPs), it has been observed that only a small fraction of the dopants participate in the process of phosphorescence.[10,11] Many long lasting phosphors are based on paramagnetic doping with rare-earth elements. Clearly, the distribution of paramagnetic dopant ions in the host lattice could affect the brightness,[12,13] the emission wavelength,[14] the efficiency[13] and the afterglow duration[15–17] of phosphors. One reason is the concentration quenching effect[10,18] which refers to the phenomenon that the luminescence yield decreases with increasing activator concentration at high concentrations. According to the statistical trap mechanism,[18–21] for the inorganic phosphors, the energy transfer probability increases dramatically if the activator ions are close to each other, due to the D^{-6} dependence (D is the distance between two activator centers) which relates to the electric dipole–dipole interaction nature of this energy transfer.

Therefore, homogeneous doping is often demanded in order to achieve optimal optical properties, and in fact methods such as the sol–gel method[22] and the homogeneous precipitation[23] are often applied in phosphor synthesis to improve doping homogeneity.

What does "homogeneous doping" mean? According to the IUPAC gold book,[24] "homogeneous" refers to "the degree to which a property or a constituent is uniformly distributed throughout a quantity of material". By this definition, a specific scale for the material's quantity is required over which a property is homogeneous. While glass appears homogeneous to the human eye at the wavelength of several hundred nanometers, its refractive index gives evidence of the inner disorder when going to shorter wavelengths, for example, under a scanning electron microscope (SEM) by the electron beam with wavelengths of few nm or Å.[25]

The investigation of doping homogeneity can be achieved by different analytical techniques depending on the required length scale of homogeneity. Homogeneous doping is often assumed if the lattice parameters determined by X-ray diffraction follow Vegard's empirical law.[26,27] While neutron diffraction and some X-ray diffraction devices can be used to determine pair-distribution functions to study doping inhomogeneity,[28–30] this is hardly possible on standard laboratory X-ray diffractometers;[31] optical spectroscopy techniques such as X-ray photoelectron spectroscopy (XPS)[32] can provide the distribution of paramagnetic dopant ions on the surface but not in the bulk; another surface technique to study homogeneity is electron microscopy[33,34] which offers a direct image on spots of the surface of the sample down to the atomic scale. In addition, atomic probe tomography[35] can provide 3D pictures on the distribution of dopants down to nm and atomic scale.

Here we want to focus on magnetic resonance spectroscopy to study doping homogeneity. By electron spin resonance spectroscopy

[a] *Inorganic Materials Chemistry, University of Siegen, Adolf-Reichwein-Str. 2, 57076 Siegen, Germany. E-mail: schmedt_auf_der_guenne@chemie.uni-siegen.de*

[b] *ParisTech-CNRS, Institut de Recherche de Chimie Paris, 11, Rue Pierre et Marie Curie, 75005 Paris, France*

[c] *Inorganic Chemistry, University of Leipzig, Johannisallee 29, 04103 Leipzig, Germany*

† Electronic supplementary information (ESI) available: Error propagation; a comparison of different wipe-out radii with the experimental data; and details of the Fortran program. See DOI: 10.1039/c5cp07606d

9752 | *Phys. Chem. Chem. Phys.*, 2016, **18**, 9752–9757

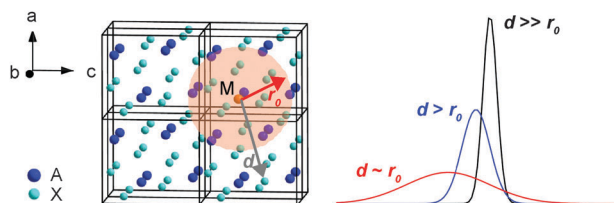This journal is © the Owner Societies 2016

Fig. 1 A schematic sketch of a paramagnetic ion doped inorganic crystal structure and the possible corresponding paramagnetic ion induced effects (paramagnetic shift and broadening) in the solid state NMR spectra of X nuclei. M stands for the paramagnetic dopant ion, A is the to-be-substituted host ion while X refers to the NMR nuclei; d is the distance between the paramagnetic ion and the NMR nuclei, and r_0 is the wipe-out radius. The resonances of X nuclei become apparently non-observable or they "vanish" if $d < r_0$.

(ESR) information about the homogeneity of doping with paramagnetic atoms can be extracted via lineshape analysis[36,37] or by multipulse spectroscopy.[38] In this contribution we use nuclear magnetic resonance spectroscopy (NMR) to analyze the environment of the doped paramagnetic atoms to obtain information about their distribution in the diamagnetic host material. The advantage of this inverse approach as compared to ESR is that non-doped areas which are not visible in the ESR experiment are not overlooked. So far NMR studies of sample homogeneity[37,39–53] have focused on the variation of magnetization with the spin lattice relaxation time T_1. Often combined models are suggested which try to derive the observed relaxation time distribution from models taking into account spin-diffusion between nuclear spins and paramagnetic relaxation pathways of nuclear spin-systems. Models suggest that spin-diffusion only becomes efficient for nuclei outside a certain radius (the so called wipe-out radius[54–56]) around the paramagnetic ion. Owing to the extremely fast relaxation mechanism near typical paramagnetic ions, the detection of the nuclei in their direct environment is technically quite difficult due to significant distortions in the measured relaxation distribution function. In addition, the paramagnetic shift due to Fermi-contact and pseudo-contact interactions might shift the resonance line out of the spectral window thereby rendering it non-observable.

Interestingly, although the effects induced by paramagnetic ions[53,57–59] regarding the paramagnetic shift, relaxation and lineshape (Fig. 1) are well understood, for example, ^{6}Li MAS NMR spinning side band manifolds[60] and shifts[61] are shown to be very sensitive to the nearest coordination sphere of Mn ions, to the best of our knowledge, the approach to simply quantify the signal intensity of the nuclei outside the wipe-out radius to study the doping homogeneity has not been used so far.

Based on the above considerations, the working hypothesis here is that the doping homogeneity on the atomic scale can be accessed by quantitative solid state NMR via the peak area measurements.

Experimental

Synthesis of $Sr_{1-x}Eu_xH_2$ doping series

Eu is incorporated in the Sr metal before contacting with H_2 to make sure that the doping is as homogeneous as possible

within the limit of the lab work. The starting materials and the metal hydride products are very sensitive to air and were therefore handled in an argon filled glove box. Strontium and europium were melted together in order to achieve optimal homogeneity as described in the earlier work.[62] The resulting alloys were hydrogenated in an autoclave made from hydrogen resistant Nicrofer® 5219 alloy (Inconel 718) at 650 K and 100 bar hydrogen pressure. The europium content was determined by ICP-MS analysis. Further details of preparation, X-ray diffraction and chemical analysis can be found in earlier work.[62]

Solid state NMR

The solid state NMR experiments were performed at 11.75 T on a Bruker Avance III NMR spectrometer equipped with a commercial 1.3 mm MAS probe at a ^{1}H frequency of 500 MHz under ambient conditions. The sample spinning frequency was 40 kHz.

The chemical shifts of ^{1}H are reported using the δ scale, relative to 1% tetramethylsilane (TMS) in $CDCl_3$.[63] The peak area quantification is based on the analysis of back-extrapolated spin-echo experiments.[64]

The side bands were taken into consideration when calculating the peak area. An estimated error of 10% for the quantification against the external reference adamantane was taken into account subsequently. Peak areas were obtained by deconvolution with several Gaussian and Lorentzian functions using a home-written program.

Results and discussion

In order to test the hypothesis, we present a case study where we use crystalline SrH_2 as the host material doped with the paramagnetic ions of Eu(II). Strontium hydride and europium hydride form a solid solution $Sr_{1-x}Eu_xH_2$ and show a Vegard[27] like behaviour,[65] which can be expected considering the crystal chemical similarities of strontium and europium hydrides.[66] The unit cell volume shows an approximate linear dependence on x for the full substitution range $0 \leq x \leq 1$ (Fig. 2).

The mole fraction of the paramagnetic dopant is defined as $x_{para} = \dfrac{N_{para}}{N_{host} + N_{para}}$, where N_{para} and N_{host} refer to the number
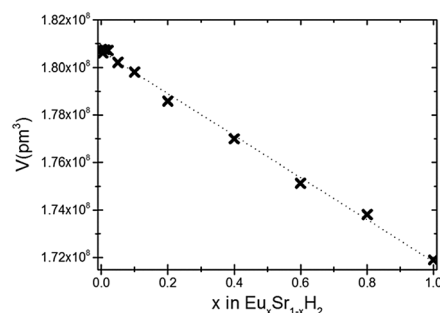

Fig. 2 Unit cell volumes as a function of the substitution degree x in $Sr_{1-x}Eu_xH_2$ as determined by Rietveld refinement based on X-ray powder diffraction data. The dotted line represents a linear fit resulting in $V(Sr_{1-x}Eu_xH_2) = 1.8067(7) \cdot 10^8$ pm^3 $- 8.8(1) \cdot 10^6$ pm$^3 \cdot x$.

of dopant ions and the corresponding host sites that can be occupied by the dopant ions (for simplicity, they are written as the host ions in the rest of the paper). In this case, the dopant ion is Eu^{2+} and the host ion is Sr^{2+}, therefore we specify the doping mole fraction of Eu as x_{Eu} in the figures.

In order to test our hypothesis, the correlation between x_{para} and the visible peak areas is first set up, and the experimentally visible H fraction $f_{visible}$ was introduced. In the ideal case, with a suitable internal reference, the observed peak area fraction is a quantitative reflection of the visible H percentage. On the other hand, in the following sub-chapters, in all theoretical models, the visible H percentage is calculated as the ratio of the number of NMR "visible" ^1H nuclei, which are located outside of the Eu influencing spheres, to the total number of H atoms.

The presented analysis is organized in the following way. In the first part we present the experimental data obtained by quantitative ^1H NMR measurements and an empirical function for describing the observed findings. In the second part we discuss the assumptions made for deriving analytical functions for the fraction of visible ^1H atoms as a function of the doping concentration. In part three analytical functions are derived for describing the obtained NMR data for the statistical doping scenario.

We obtained quantitative ^1H NMR spectra of a doping series of $Sr_{1-x}Eu_xH_2$. The NMR spectra (see ESI†) qualitatively show a decay of signal intensity for the ^1H peak found in the sample with the lowest doping mole fraction $x = 10^{-8}$, and a broadening of the resonance with higher doping concentration x.

From the observed peak area per mole of sample (A/n) of $Sr_{1-x}Eu_xH_2$ we define the ratio $f_{visible}$ as $f_{visible} = \dfrac{A_{doped}/n_{doped}}{A_{non\text{-}doped}/n_{non\text{-}doped}}$. Here visible refers to nuclei whose ^1H NMR peaks remain approximately at the same position in the spectrum as a non-doped sample. For the following treatment we assume that the paramagnetic shift of atoms is the dominant reason why a nucleus becomes "invisible" in the above sense and we neglect the relaxation effects which can make the signal of a nucleus vanish in the dead-time delay of the probehead.

The ratio $f_{visible}$ is experimentally accessible and plotted against x_{Eu} on a logarithmic scale, which, as expected, shows a simple behavior following a monotonous decay (see ESI†). Empirically the following function was found which can describe the experimental data (see ESI†):

$$f_{visible}(x_{para}) = \exp\left[-k_1\left(x_{para}\right)^{k_2}\right]$$

The coefficients k_1 and k_2 were used as fitting parameters which took the values $k_1 = 425 \pm 113$ and $k_2 = 1.00 \pm 0.04$, respectively.

In order to derive analytical functions for $f_{visible} = f_{visible}(x_{para})$ we make a number of assumptions. We assume that all atoms inside a radial sphere of influence (called wipe-out radius r_0) around a paramagnetic atom (Fig. 3) will be shifted to an extreme spectral range which makes them virtually invisible to NMR experiments. The concept of a radial sphere of influence is well established (shell-of-influence model[43,67]) and still questionable
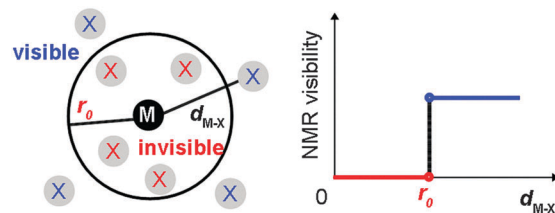

Fig. 3 A schematic drawing of the influence sphere model. M is the paramagnetic center while X represents the NMR nuclei. According to the influence sphere model, if the distance d_{M-X} between an X nucleus and the paramagnetic ion M is smaller than the wipe-out radius r_0, the X nucleus is not visible by NMR. On the other hand, the X nuclei with $d_{M-X} > r_0$ are visible by NMR.

if one takes into account (1) the angular dependence of the hyperfine interaction, (2) the unrealistic, discontinuous consideration at the border between visible and invisible H atoms and (3) the possibility of multiple interactions with different Eu atoms, which could mutually cancel each other. On the other hand, the pseudo-contact shift carries a term with an inverse cubic distance dependence which corresponds to a strong radial dependence.

In order to calculate the visible fraction $f_{visible}$ as the visible volume divided by the total volume, the assumption about the number density of H ions has to be made first. Only in the condition that the number density is already approximately a constant at a distance smaller than the wipe-out radius, the oscillating error induced by the number density variation of the lattice at small distance can be neglected. The following is to show that the calculation system of 5 Å is enough for obtaining a fairly good ($<20\%$ error) number density approximation.

To evaluate the number density of H atoms, a discrete point-model based on the crystal structure may serve as a reference. Such models were implemented in Fortran90 (ESI†) to analyze different doping scenarios, however their analysis always requires full information about the unit cell which is hardly feasible in a general case. A more practical approach is to follow a continuous model, namely to calculate the expected number of observed nuclei around a dopant with the help of the average number density and the volume of a sphere. The difference between these two approaches becomes apparent from the normalized integral of the radial pair distribution function $G(r) = \dfrac{3}{r^3}\int_0^r g(r') \cdot (r')^2 \, dr'$ of $Sr_{1-x}Eu_xH_2$ (Fig. 4). The better the continuous approximation the smaller the difference from 1.0. From the $G_{SrH}(r)$ it becomes obvious that for spheres with a size bigger than 4.7 Å the errors in the number of atoms in the sphere deviates by less than 20% from the value expected from the number density. We conclude that the continuous approximation is acceptable given that the radius r_0 below which the ^1H nuclei become invisible is of the order of 10 to 20 Å.

The visible H fraction is easily counted for a statistical doping scenario for a given wipe-out radius r_0 with the help of a small computer program. By comparing the experimental plot with the calculated data for different assumed radii, the wipe-out radius can be estimated at around 17 Å with a convergence criterion of 3% for the lowest doping level (see ESI†).
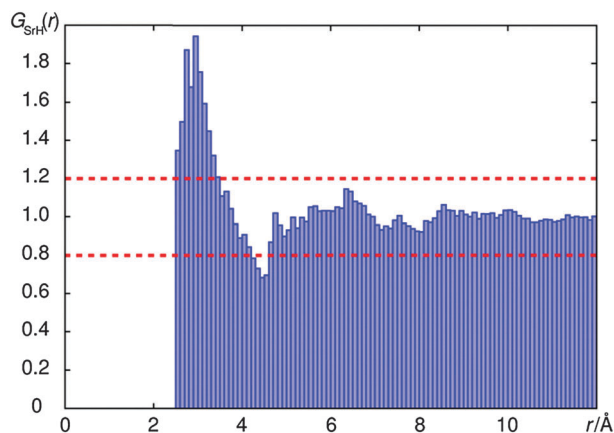
Fig. 4 The integrated pair distribution function $G_{SrH}(r)$ of SrH$_2$ calculated from the crystal structure by counting atoms on a grid of 0.1 Å.

An interesting question is how the empirical fitting function can be given a physical meaning in the sense that becomes a function of the wipe-out radius $f_{visible} = f_{visible}(r_0,x_{para})$ and the average number densities according to the crystal structure.

The approach we took is to calculate the regime of extreme low doping concentrations. For those the function $f_{visible} = f_{visible}(r_0,x_{para})$ should approach values calculated from the total volume $V_{invisible}$ of all wipe-out spheres from the volume of an individual sphere multiplied by the number of dopants. These spheres are not likely to be superimposed at low concentration, which justifies the approach.

$$V_{invisible} = \frac{4}{3}\pi r_0^3 N_{para}$$

Here N_{para} is the number of dopant ions in the total volume of the crystal V_{total}. The doping mole fraction x_{para} helps relate N_{para} and the unit cell volume V_{UC} to the total volume of the crystal V_{total}. The term $N_{host\,UC}$ refers to the number of "dopable" sites in the unit cell, in this example, the number of Sr atoms per unit cell.

$$V_{total} = \frac{N_{host} + N_{para}}{N_{hostUC}}V_{UC}$$

Assuming equal ^{1}H number densities in each volume unit, the invisible fraction is proportional to the invisible volume ratio, which can be described as a function of the wipe-out radius r_0.

$$f_{invisible}(r_0,x_{para}) = \frac{V_{invisible}}{V_{total}} = \frac{4\pi N_{hostUC}}{3V_{UC}}r_0^3 x_{para}$$

$$f_{visible}(r_0,x_{para}) = 1 - \frac{4\pi N_{hostUC}}{3V_{UC}}r_0^3 x_{para}$$

The pre-factor a in the empirical exponential fitting function $f_{visible}(r_0,x_{para}) = \exp(-ar_0^3 x_{para})$ is fitted to be $a = 0.0863 \pm 0.0016$, which shows a resemblance with the theoretical value $\frac{4\pi N_{hostUC}}{3V_{UC}} = 0.0939$, which can be explained mathematically by the Taylor expansion in the small x_{para} range:

$$f_{visible}(r_0,x_{para}) = \exp(-ar_0^3 x_{para})$$

$$\approx 1 - ar_0^3 x_{para} + \frac{1}{2}a^2 r_0^6 x_{para}^2 - \cdots \quad \text{as } x_{para} \rightarrow 0$$

By asymptotic analysis, as x_{para} approaches zero, the higher order terms can be neglected, and the following equation holds

$$f_{visible}(r_0,x_{para}) \sim 1 - ar_0^3 x_{para} \quad \text{as } x_{para} \rightarrow 0$$

or written as $\lim_{x_{para} \rightarrow 0} f_{visible}(r_0,x_{para}) = 1 - ar_0^3 x_{para}$, which shows a resemblance to the formula

$$f_{visible}(r_0,x_{para}) = 1 - \frac{4\pi N_{hostUC}}{3V_{UC}}r_0^3 x_{para}$$

with $a = \frac{4\pi N_{hostUC}}{3V_{UC}}$ as $x_{para} \rightarrow 0$.

Due to the fact that the experimental data fit the calculated curve based on the statistical distribution model (see Fig. 5), we conclude that the SrH$_2$:Eu samples are homogeneously doped on the Å scale and this homogeneity refers to a statistical distribution of Eu^{2+} ions.

A remaining question is if the wipe-out radius r_0 for a paramagnetic dopant ion is a constant or within a certain limit. If so, testing the homogeneity by a single NMR experiment could be feasible and promising. Here we provide an embryo idea for further NMR investigation by introducing a parameter, namely the cut-off mole fraction x_0. Based on the statistical distribution model, x_0 is defined that if a sample is statistically doped at the doping level $x_{para} > x_0$, then the macroscopic signal in the MAS NMR measurement is very weak or non-observable ($f_{visible} < 0.1\%$), see Fig. 5.

To the best of our knowledge, the numeric value for the wipe-out radius r_0 has not been published before, and for the first time, we calculated the r_0 for Eu^{2+} to be around 17 Å. If the wipe-out radius r_0 would be approximately a calculable constant for Eu^{2+} in different host lattices, and if the empirical fitting function could be applied, then the doping homogeneity could be accessible by only one NMR experiment at the cut-off mole fraction x_0 together with a measurement of the non-doped sample.
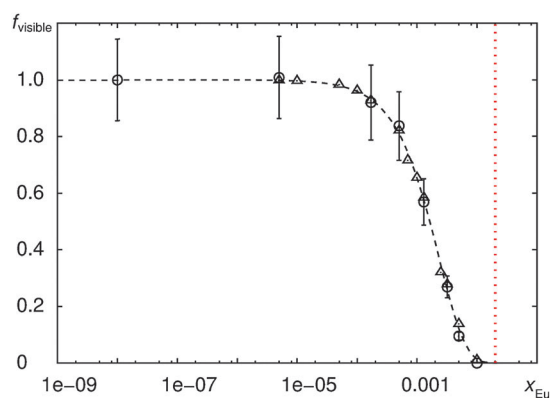
Fig. 5 The comparison of the visible H fraction $f_{visible}$ calculated from the ^{1}H MAS NMR back extrapolated full echo series experiments[63] with error bars, calculated according to the statistical distribution model and the fitted function $f_{visible} = \exp(-ar_0^3 x_{Eu})$ with $a = 0.0863 \pm 0.0016$, plotted against the Eu doping mole fraction x_{Eu} in the log scale. The wipe-out radius r_0 is taken as 17 Å. The hollow circle, the hollow triangle and the dashed line represent the experimental data, the calculated data and the function plot, respectively. The dotted line at $x_{Eu} \approx 0.0163$ is the cut-off concentration x_0 line, at which the $f_{visible}$ approaches zero ($f_{visible} < 0.1\%$).

This journal is © the Owner Societies 2016

Phys. Chem. Chem. Phys., 2016, 18, 9752–9757 | 9755

Conclusions

The main question of this work is whether the paramagnetic doping homogeneity can be quantitatively investigated by solid state NMR. Based on the comparison of the experimental and the calculated data, we conclude that by applying a simple function $f_{visible}(r_0, x_{para}) = \exp(-a r_0^3 x_{para})$ with $a = \dfrac{4\pi N_{hostUC}}{3V_{UC}}$ which connects the wipe-out radius r_0 and the doping mole fraction x_{para} with the NMR visible signal fraction $f_{visible}$, the statistical doping scenario can be described adequately.

The above-mentioned method may serve as an efficient tool for quantitative analysis of the doping homogeneity of an arbitrary paramagnetic dopant in different host lattices, especially for the rare earth and transition metal elements. This may be helpful for applications such as the design of quantum dots and phosphors. The approach is hardly limited by the choice of the isotope as long as a signal can be obtained in 1D NMR spectroscopy. Thus studies even with less common NMR nuclei such as ^{71}Ga, ^{75}As or ^{37}Cl are possible. This method is also applicable to homogeneity analysis of nano-scale materials on an Å scale.

Acknowledgements

References

1 R.-J. Xie, N. Hirosaki, Y. Li and T. Takeda, *Materials*, 2010, **3**, 3777–3793.

2 K. Van den Eeckhout, P. F. Smet and D. Poelman, *Materials*, 2010, **3**, 2536–2566.

3 W. Schnick, *Phys. Status Solidi RRL*, 2009, **3**, A113–A114.

4 R. Mueller-Mach, G. Mueller, M. R. Krames, H. A. Höppe, F. Stadler, W. Schnick, T. Juestel and P. Schmidt, *Phys. Status Solidi A*, 2005, **202**, 1727.

5 C. C. Lin and R.-S. Liu, *J. Phys. Chem. Lett.*, 2011, **2**, 1268–1277.

6 A. Bonanni, *Semicond. Sci. Technol.*, 2007, **22**, R41.

7 R. I. Epstein and M. Sheik-Bahae, *Optical Refrigeration, Science and Applications of Laser Cooling of Solids*, Wiley-VCH, 2009, pp. 1–32.

8 R. Jones, *Opt. Mater.*, 2006, **28**, 718–722.

9 V. Bachmann, C. Ronda, O. Oeckler, W. Schnick and A. Meijerink, *Chem. Mater.*, 2008, **21**, 316–325.

10 G. Blasse and B. C. Grabmaier, *Luminescent Materials*, Springer Berlin Heidelberg, Berlin, Heidelberg, 1994.

11 F. Clabau, X. Rocquefelte, T. Le Mercier, P. Deniard, S. Jobic and M.-H. Whangbo, *Chem. Mater.*, 2006, **18**, 3212–3220.

12 I. Yu and M. Senna, *Appl. Phys. Lett.*, 1995, **66**, 424–426.

13 W. Park, T. C. Jones, W. Tong, S. Schön, M. Chaichimansour, B. K. Wagner and C. J. Summers, *J. Appl. Phys.*, 1998, **84**, 6852–6858.

14 N. C. George, K. A. Denault and R. Seshadri, *Annu. Rev. Mater. Res.*, 2013, **43**, 481–501.

15 D. Poelman, N. Avci and P. F. Smet, *Opt. Express*, 2009, **17**, 358–364.

16 F. Clabau, X. Rocquefelte, S. Jobic, P. Deniard, M.-H. Whangbo, A. Garcia and T. Le Mercier, *Chem. Mater.*, 2005, **17**, 3904–3912.

17 K. Van den Eeckhout, P. F. Smet and D. Poelman, *Materials*, 2011, **4**, 980–990.

18 D. L. Dexter and J. H. Schulman, *J. Chem. Phys.*, 1954, **22**, 1063–1070.

19 T. Förster, *Ann. Phys.*, 1948, **437**, 55–75.

20 D. L. Dexter, *J. Chem. Phys.*, 1953, **21**, 836–850.

21 J. Knoester and J. E. V. Himbergen, *J. Chem. Phys.*, 1987, **86**, 3571–3576.

22 M. L. Pang, J. Lin, J. Fu, R. B. Xing, C. X. Luo and Y. C. Han, *Opt. Mater.*, 2003, **23**, 547–558.

23 Y. Kawahara, V. Petrykin, T. Ichihara, N. Kijima and M. Kakihana, *Chem. Mater.*, 2006, **18**, 6303–6307.

24 W. Horwitz, *Pure Appl. Chem.*, 2009, **62**, 1193–1208.

25 A. Ben-Yakar, R. L. Byer, A. Harkin, J. Ashmore, H. A. Stone, M. Shen and E. Mazur, *Appl. Phys. Lett.*, 2003, **83**, 3030.

26 L. Vegard, *Z. Phys.*, 1921, **5**, 17–26.

27 L. Vegard and H. Dale, *Z. Kristallogr., Kristallgeom., Kristallphys., Kristallchem*, 1928, **67**, 148–162.

28 E. S. Božin, G. H. Kwei, H. Takagi and S. J. L. Billinge, *Phys. Rev. Lett.*, 2000, **84**, 5856–5859.

29 S. J. L. Billinge, T. Proffen, V. Petkov, J. L. Sarrao and S. Kycia, *Phys. Rev. B: Condens. Matter Mater. Phys.*, 2000, **62**, 1203–1211.

30 J. Huang, J. Xu, H. Luo, X. Yu and Y. Li, *Inorg. Chem.*, 2011, **50**, 11487–11492.

31 C. Michaelsen, *Philos. Mag. A*, 1995, **72**, 813–828.

32 C. Dong, J. Pichaandi, T. Regier and F. C. J. M. van Veggel, *J. Phys. Chem. C*, 2011, **115**, 15950–15958.

33 J. Liu, *J. Electron Microsc.*, 2005, **54**, 251–278.

34 R. Pantel and G. Servanton, in *Transmission Electron Microscopy in Micro-Nanoelectronics*, ed. A. Claverie and M. Mouis, John Wiley & Sons, Inc., 2012, pp. 37–64.

35 G. Scappucci, W. M. Klesse, L. A. Yeoh, D. J. Carter, O. Warschkow, N. A. Marks, D. L. Jaeger, G. Capellini, M. Y. Simmons and A. R. Hamilton, *Sci. Rep.*, 2015, **5**, 12948.

36 C. P. Poole and H. A. Farach, *Bull. Magn. Reson.*, 1979, **1**, 162–194.

37 S. Sen and J. F. Stebbins, *J. Non-Cryst. Solids*, 1995, **188**, 54–62.

38 R.-A. Eichel, *J. Am. Ceram. Soc.*, 2008, **91**, 691–701.

39 N. Bloembergen, *Physica*, 1949, **15**, 386–426.

40 P.-G. de Gennes, *J. Phys. Chem. Solids*, 1958, **7**, 345–350.

41 W. W. Simmons, W. J. O'Sullivan and W. A. Robinson, *Phys. Rev.*, 1962, **127**, 1168–1178.

42 H. E. Rorschach Jr., *Physica*, 1964, **30**, 38–48.

43 C. D. Jeffries, *Proc. Phys. Soc.*, 1966, **88**, 257–258.

44 G. R. Khutsishvili, *Phys.-Usp.*, 1966, **8**, 743–769.

45 I. J. Lowe and S. Gade, *Phys. Rev.*, 1967, **156**, 817–825.

46 I. J. Lowe and D. Tse, *Phys. Rev.*, 1968, **166**, 279–291.

9756 | *Phys. Chem. Chem. Phys.*, 2016, **18**, 9752–9757

This journal is © the Owner Societies 2016

47 G. R. Khutsishvili, *Phys.-Usp.*, 1969, **11**, 802–815.

48 M. Punkkinen, *Phys. Kondens. Mater.*, 1971, **13**, 79–88.

49 E. F. W. Seymour and C. A. Sholl, *J. Phys. C: Solid State Phys.*, 1985, **18**, 4521–4537.

50 G. B. Furman, E. M. Kunoff, S. D. Goren, V. Pasquier and D. Tinet, *Solid State Nucl. Magn. Reson.*, 1995, **4**, 255–258.

51 G. B. Furman, E. M. Kunoff, S. D. Goren, V. Pasquier and D. Tinet, *Phys. Rev. B: Condens. Matter Mater. Phys.*, 1995, **52**, 10182–10187.

52 G. B. Furman, A. M. Panich, A. Yochelis, E. M. Kunoff and S. D. Goren, *Phys. Rev. B: Condens. Matter Mater. Phys.*, 1997, **55**, 439–444.

53 S. Maron, G. Dantelle, T. Gacoin and F. Devreux, *Phys. Chem. Chem. Phys.*, 2014, **16**, 18788–18798.

54 M. Punkkinen, *Phys. Kondens. Mater.*, 1971, **13**, 79–88.

55 P. Bernier, H. Launois and H. Alloul, *J. Phys., Colloq.*, 1971, **32**, C1-513–C1-515.

56 B. Giovannini, P. Pincus, G. Gladstone and A. J. Heeger, *J. Phys., Colloq.*, 1971, **32**, C1-163–C1-171.

57 H. Eckert, J. P. Yesinowski, L. A. Silver and E. M. Stolper, *J. Phys. Chem.*, 1988, **92**, 2055–2064.

58 G. Aromí, M. J. Knapp, J.-P. Claude, J. C. Huffman, D. N. Hendrickson and G. Christou, *J. Am. Chem. Soc.*, 1999, **121**, 5489–5499.

59 S. E. Butcher, F. H.-T. Allain and J. Feigon, *Biochemistry*, 2000, **39**, 2174–2182.

60 Y. J. Lee and C. P. Grey, *J. Phys. Chem. B*, 2002, **106**, 3576–3582.

61 Y. J. Lee, S.-H. Park, C. Eng, J. B. Parise and C. P. Grey, *Chem. Mater.*, 2002, **14**, 194–205.

62 R. Hahn, N. Kunkel, C. Hein, R. Kautenburger and H. Kohlmann, *RSC Adv.*, 2015, **5**, 9722–9726.

63 R. K. Harris and E. D. Becker, *J. Magn. Reson.*, 2002, **156**, 323–326.

64 Y. S. Avadhut, D. Schneider and J. Schmedt auf der Günne, *J. Magn. Reson.*, 2009, **201**, 1–6.

65 N. Kunkel, H. Kohlmann, A. Sayede and M. Springborg, *Inorg. Chem.*, 2011, **50**, 5873–5875.

66 K. Yvon, H. Kohlmann and B. Bertheville, *Chim. Int. J. Chem.*, 2001, **55**, 505–509.

67 T. J. Schmugge and C. D. Jeffries, *Phys. Rev.*, 1965, **138**, A1785–A1801.

Homogeneity of doping with paramagnetic ions by NMR

Wenyu Li[a] , Vinicius Ribeiro Celinski[a], Johannes Weber[a], Nathalie Kunkel[b], Holger Kohlmann[c],

Jörn Schmedt auf der Günne[*,a]

[a] Inorganic Materials Chemistry, University of Siegen, Adolf-Reichwein-Str. 2, 57076 Siegen, Germany

[b] ParisTech-CNRS, Institut de Recherche de Chimie Paris, 11, Rue Pierre et Marie Curie, 75005 Paris, France

[c] Inorganic Chemistry, University of Leipzig, Johannisallee 29, 04103 Leipzig, Germany

[*]schmedt_auf_der_guenne@chemie.uni-siegen.de

Supporting information

1. Quantitative 1D ^{1}H NMR spectra of $Sr_{1-x}Eu_xH_2$ samples

We obtained quantitative ^{1}H NMR spectra on a doping series of $Sr_{1-x}Eu_xH_2$. The NMR spectra (Fig. 1) qualitatively show a decay of signal intensity for the ^{1}H peak found in the sample with the lowest doping mole fraction $x = 10^{-8}$, and a broadening of the resonance with higher doping concentration x.
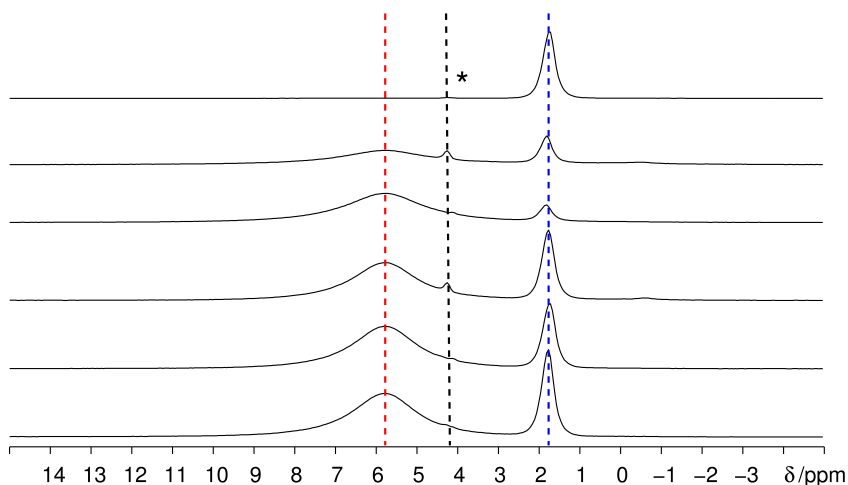

Figure 1: The stack plot of solid state ^{1}H MAS NMR full echo spectra of a mixture of $Sr_{1-x}Eu_xH_2$ (peak at 6 ppm) with adamantane (peak at 1.8 ppm) with different Eu doping mole fraction. x_{Eu} equals to 0.005, 0.0032, 0.0013, 0.0005, 0.00017, 0.000005, 10^{-8} from the top to the bottom. The peaks with the asterisk mark belong to a trace impurity phase related to the hygroscopic reaction of SrH_2. The intensity scale is adapted to the amount of sample inside each rotor, however the amount of adamantane may slighly vary.

2. "Box-in-a-box" Algorithm

How we set up the "box-in-a-box" algorithm of our Fortran 90 program, as shown in the Fig. 2, can be described as follows. The small box in the center is one unit cell of the $PbCl_2$-type crystal structure of SrH_2[1]. The outer big box is built up based on the 3D translational symmetry around the center unit cell. The statistical doping of Eu ions is achieved by applying a system randomizer to replace Sr atoms with Eu atoms, and the probability of replacement is statistically speaking equal within the big box, including the center box. The wipe-out region of Eu ions is set up as a sphere with Eu in the center and the wipe-out radius. The visible fraction $f_{visible}$ is thus defined as the number of H atoms within the wipe-out region divided by the total number of H atoms. When the size of the big box is significantly bigger than the wipe-out radius, the influence of boundary to the center small box can be minimized, therefore the visible fraction $f_{visible}$ in the center box can represent the $f_{visible}$ in a big boundless box, which is often an idealized model of crystals. To average out the fluctuation in the randomized Sr/Eu setup, the calculation is looped until $f_{visible}$ reaches convergence (deviation less than 2%). Different wipe-out radii are assumed and different $f_{visible}$ values are calculated accordingly.
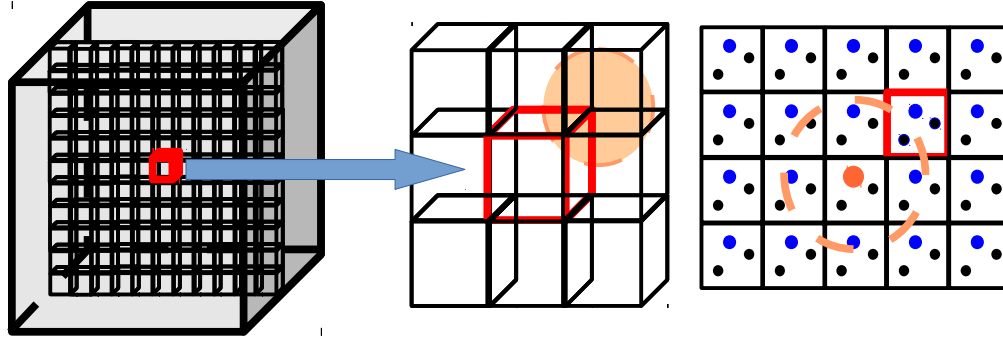
Figure 2: The "box-in-a-box" algorithm for the Fortran90 program. The center small box is one unit cell of the crystal structure [1] of SrH_2. The outer big box is built up based on the 3D translational symmetry around the center unit cell. The visible fraction $f_{visible}$ is calculated as the number of H atoms within the influence region, which are spheres with Eu center and the wipe-out radius r_0, divided by the total number of H atoms.

3. Error propagation for quantitative NMR

The error bars (Fig. 3) are calculated according to three error sources: (1) the mass error from the weighing process on the microbalance, which is an absolute error at around 1µg; (2) the intensity error, which is a relative error originated from the external reference method, around 10%; (3) the fitting error, which is originating from the fitting of the peak area values from the full echo experiments. The fitting error slightly differs for different samples, but all values are around 2%.

The experimental measurements are the mass m and the peak area A. A_0 is the extrapolated peak area at zero delay. External referencing method was applied and here we define a parameter $P = \dfrac{A_0}{A_{ref}}$ which relates to the stability of the spectrometer. The error of P can be calculated from the formula (1).

$$\Delta P = \sqrt{\left(\frac{\Delta A_0}{A_{ref}}\right)^2 + \left(\frac{A_0 \Delta A_{ref}}{A_{ref}^2}\right)^2} = \sqrt{\left(\frac{A_0}{A_{ref}} \frac{\Delta A_0}{A_0}\right)^2 + \left(\frac{A_0}{A_{ref}} \frac{\Delta A_{ref}}{A_{ref}}\right)^2} = P\sqrt{\left(\frac{\Delta A_0}{A_0}\right)^2 + \left(\frac{\Delta A_{ref}}{A_{ref}}\right)^2} \tag{1}$$

herein $\dfrac{\Delta A_{ref}}{A_{ref}} = 10\%$ and $\dfrac{\Delta A_0}{A_0} \approx 2\%$, therefore $\dfrac{\Delta P}{P} \approx 0.102$. $f_{visible}$ can be related to the parameter P

$$f_{visible} = \frac{A_{doped}/n_{doped}}{A_{non-doped}/n_{non-doped}} = \frac{P_{doped}}{P_{non-doped}} \frac{m_{non-doped}}{m_{doped}} \tag{2}$$

A_{doped} and $A_{non-doped}$ refer to the A_0 values of the doped and non-doped samples, respectively. As for the mass m, there is the mass error $\Delta m \approx 0.001\,mg$. The final error propagation can be expressed as an equation for Δf, which is the standard deviation of $f_{visible}$

$$\Delta f = \sqrt{\left(\frac{\Delta P_{doped}}{P_{doped}} \frac{A_{doped}}{A_{non-doped}} \frac{m_{non-doped}}{m_{doped}}\right)^2 + \left(\frac{A_{doped}}{A_{non-doped}} \frac{\Delta P_{non-doped}}{P_{non-doped}} \frac{m_{non-doped}}{m_{doped}}\right)^2 + \left(\frac{A_{doped}}{A_{non-doped}} \frac{\Delta m_{non-doped}}{m_{doped}}\right)^2 + \left(\frac{A_{doped}}{A_{non-doped}} \frac{m_{non-doped} \Delta m_{doped}}{m_{doped}^2}\right)^2} \tag{3}$$
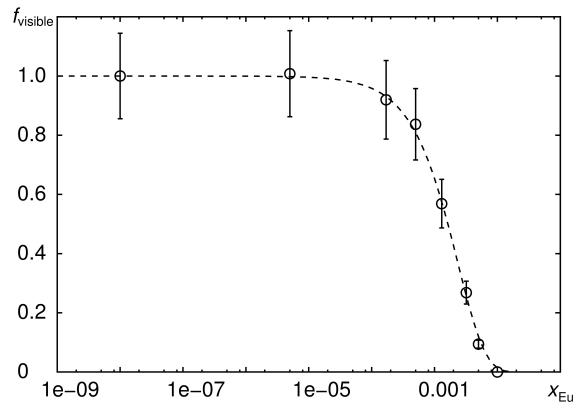
Figure 3: comparison of the visible H fraction $f_{visible}$ calculated from experimental ^{1}H MAS NMR spectra (hollow circles) and the empirical fitted function (dashed line) $f_{visible} = \exp\left[-k_1\left(x_{Eu}\right)^{k_2}\right]$ with $k_1 = 425 \pm 113$ and $k_2 = 1.00 \pm 0.04$, plotted against the Eu doping mole fraction x_{Eu} in log scale.

4. Estimation of the wipe-out radius from calculated data and experimental data

As the value of wipe-out radius r_0 was unknown, different values were assumed and visible H fractions $f_{visible}$ were calculated by Fortran program, based on the statistical distribution of Eu(II) ions with different doping mole fraction x_{Eu}. By comparing the obtained data set of $f_{visible}$ with the result from quantitative NMR measurements, the estimation of the $r_0 = 17$ Å for Eu(II) in SrH_2 can be achieved (see Fig. 4).
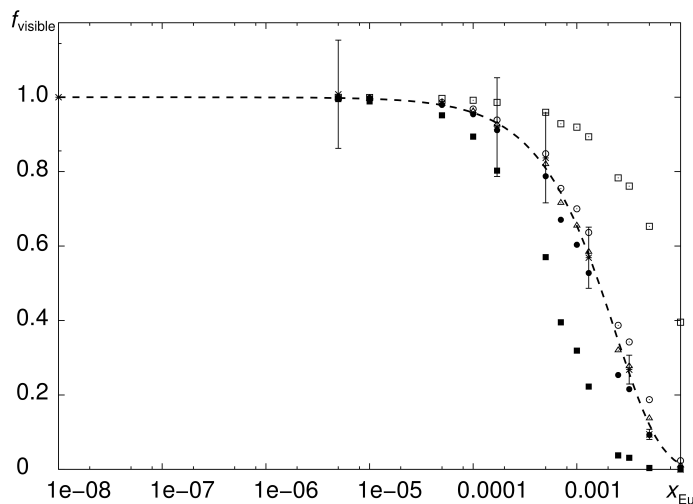
Figure 4: The comparison of the visible H fraction $f_{visible}$ calculated from the ^{1}H MAS NMR back extrapolated full echo series experiments[2] with error bars, calculated according to the statistical distribution model and the fitted function $f_{visible} = \exp\left(-a r_0^3 x_{Eu}\right)$ with $a = 0.0863 \pm 0.0016$ and $r_0 = 17$ Å, plotted against the Eu doping mole fraction x_{Eu} in log scale. The asterisk marks, the hollow squares, the hollow circle, the hollow triangle, the solid circles, the solid squares and the dash line represent the experimental data, the calculated data at $r_0 = 10$ Å, 16 Å, 17 Å, 18 Å, 24 Å and the function plot, respectively.

Reference

1 D. Colognesi, G. Barrera, A. J. Ramirez-Cuesta and M. Zoppi, *J. Alloys Compd.*, 2007, **427**, 18–24.

2 Y. S. Avadhut, D. Schneider and J. Schmedt auf der Günne, *J. Magn. Reson.*, 2009, **201**, 1–6.

3.2 Blind Spheres of Paramagnetic Dopants in Solid State NMR

Wenyu Li, Qianyun Zhang, Jonas J. Joos, Philippe F. Smet and Jörn Schmedt auf der Günne

Contribution to the manuscript:

Based on discussions and conceptual guidance from Jörn Schmedt auf der Günne, the Rietveld refinement, the NMR study and all NMR related data analysis were done by me. The initial testing of $La_{1-x}Ln_xPO_4$ and $(Zn_{1-x}Mn_x)_3(PO_4)_2 \cdot 4H_2O$ synthesis methods was done by me. The optimization and the routine synthesis of $La_{1-x}Ln_xPO_4$ and $(Zn_{1-x}Mn_x)_3(PO_4)_2 \cdot 4H_2O$ were assisted by Qianyun Zhang. The $Sr_{1-x}Eu_xGa_2S_4$ samples were synthesized by Jonas J. Joos in the group of Philippe F. Smet. This paper was drafted by me and perfected by Jörn Schmedt auf der Günne.

Check for updates

Blind spheres of paramagnetic dopants in solid state NMR†

Wenyu Li, [a] Qianyun Zhang, [a] Jonas J. Joos, [b] Philippe F. Smet [b] and Jörn Schmedt auf der Günne *[a]

Solid-state NMR on paramagnetically doped crystal structures gives information about the spatial distribution of dopants in the host. Paramagnetic dopants may render NMR active nuclei virtually invisible by relaxation, paramagnetic broadening or shielding. In this contribution blind sphere radii r_0 have been reported, which could be extracted through fitting the NMR signal visibility function $f(x) = \exp(-ar_0^3x)$ to experimental data obtained on several model compound series: $La_{1-x}Ln_xPO_4$ (Ln = Nd, Sm, Gd, Dy, Ho, Er, Tm, Yb), $Sr_{1-x}Eu_xGa_2S_4$ and $(Zn_{1-x}Mn_x)_3(PO_4)_2 \cdot 4H_2O$. Radii were extracted for ^1H, ^{31}P and ^{71}Ga, and dopants like Nd^{3+}, Gd^{3+}, Dy^{3+}, Ho^{3+}, Er^{3+}, Tm^{3+}, Yb^{3+} and Mn^{2+}. The observed radii determined differed in all cases and covered a range from 5.5 to 13.5 Å. While these radii were obtained from the amount of invisible NMR signal, we also show how to link the visibility function to lineshape parameters. We show under which conditions empirical correlations of linewidth and doping concentration can be used to extract blind sphere radii from second moment or linewidth parameter data. From the second moment analysis of $La_{1-x}Sm_xPO_4$ ^{31}P MAS NMR spectra for example, a blind sphere size of Sm^{3+} can be determined, even though the visibility function remains close to 100% over the entire doping range. Dependence of the blind sphere radius r_0 on the NMR isotope and on the paramagnetic dopant could be suggested and verified: for different nuclei, r_0 shows a $\sqrt[3]{\gamma}$-dependence, γ being the gyromagnetic ratio. The blind sphere radii r_0 for different paramagnetic dopants in a lanthanide series could be predicted from the pseudo-contact term.

Introduction

Nuclear magnetic resonance (NMR) has contributed to the study of paramagnetic systems, such as in structural biology,[1-5] battery materials,[6-8] characterization of pharmaceutical formulation,[9,10] polymers,[11,12] chemical shift thermometers[13,14] and luminescent materials.[15-23] The range of applications of paramagnetic NMR is surprising given that the strong electronic magnetic moment of the paramagnetic species interferes with the NMR measurement in different ways. Nevertheless, paramagnetic NMR may give information about structure,[2,12] dynamics[8,24] and the distribution of paramagnetic dopants in a host.[17-22,25,26] In the latter case different approaches had been used namely relaxation times,[19,20,22] linewidths[17,18] and observed peaks areas[21,25] to relate doping homogeneity to the performance of these luminescent materials.
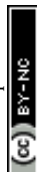
In solid-state NMR a distinction needs to be made between lanthanide atoms and transition metal atoms. The influence transition metal atoms exert on neighbouring NMR nuclei enables studies for example on battery materials[6-8] or metal organic framework compounds.[27] The computation of the influence on valence electrons is important and progress in the computation of paramagnetic shifts[28] has improved significantly in recent years. In contrast, lanthanides with few exceptions show hardly any influence from the valence shell and thus have been used for systematic experimental studies to identify contributions to the paramagnetic spin Hamiltonian.[28,29] Paramagnetic NMR of lanthanide containing compounds found various applications to luminescent materials.[15-21]

A non-trivial problem to paramagnetic NMR is that NMR resonances of paramagnetic compounds may virtually vanish in the dead-time of the NMR spectrometer by relaxation, inhomogeneous broadening mechanisms or anisotropic susceptibility broadening.[29] Lineshape analysis as proposed by Van Vleck[30] in terms of moment-analysis or NMR line width comes with a visibility caveat. Nevertheless, this approach was proved successful in the characterization of several phosphors,[17,18] where it could be shown that, as expected by van Vleck, the linewidth depended linearly on the paramagnetic doping level x at low doping concentration. It should be noted that in the high

[a] *Inorganic Materials Chemistry, University of Siegen, Adolf-Reichwein-Str. 2, 57076 Siegen, Germany. E-mail: gunnej@chemie.uni-siegen.de*

[b] *LumiLab, Department of Solid State Sciences, Ghent University, Krijgslaan 281-S1, 9000 Gent, Belgium*

† Electronic supplementary information (ESI) available: Numerical for the spectral analysis of LaPO₄:Sm, EXSY spectra for LaPO₄:Ln, ³¹P NMR relaxation data for LaPO₄:Ln. See DOI: 10.1039/c9cp00953a

This journal is © the Owner Societies 2019

Phys. Chem. Chem. Phys., 2019, **21**, 10185–10194 | 10185

doping regime a non-trivial dependence due to "exchange narrowing"[30–32] may lead to deviations from this simple behaviour. In case of luminescent materials, the doping homogeneity is of major importance to establish an optimal performance.[33,34] When luminescent ions are too close, energy can easily be transferred between them, leading to uncontrollable migration of energy in the dopant sublattice that can eventually be non-radiatively dissipated at so-called luminescence killer centres. This effect is usually referred to as concentration quenching[35,36] and has been related to the dopant distribution obtained from NMR lineshape analysis in a few cases.[17,18] Furthermore, it was evidenced by a microscopic investigation that the thermal quenching behaviour, *i.e.* the decrease of luminescence quantum yield for increasing temperatures,[37] is severely worsened for inhomogeneously doped materials due to areas with a locally more elevated doping concentration.[34]

Instead of asking for the NMR properties of the visible paramagnetic signals, it may be interesting to ask for the fraction of NMR invisible signal. If a spherical regime around a paramagnetic centre is assumed, from which no NMR signals can be detected, it is possible to relate the signal loss to the size of this sphere of influence which is known under the name blind-sphere[38,39] or wipe-out radius.[40–42] Such radii are important in solution NMR[38,39] where paramagnetic constraints are used for structure solution, and in dynamic nuclear polarization (DNP) to estimate the zone which cannot be accessed by NMR[43–45] and for luminescent materials to study doping homogeneity.[21]

Spectroscopically the blind sphere can be explained by line broadening which leads to undetectable signal by standard experiments,[39] or signal shift[46] that puts the signal outside of spectral window. The origins of blind sphere may relate to (but are not limited to) the following contributions:[39] relaxation which may involve dipolar, Curie, contact and cross relaxation mechanisms, and hyperfine shift which contains contact and pseudo-contact parts.

Reported sizes of blind spheres have been mostly related to the solution NMR, for which Bertini[39] and co-workers have laid a foundation. Besides some attempts have been made to quantify the blind sphere radius of DNP polarizing agents.[43,47] In solid state, due to anisotropic interactions and more ambiguous estimation of correlation time τ_c and spectral density function $J(\omega)$, blind sphere sizes may differ and questions about the influence that a paramagnetic centre has on its environment remain open. To the best of our knowledge, for solid crystalline samples a systematic study on the sizes of blind spheres of different inorganic dopants has not been published before.

The target of this contribution is to relate the size of blind spheres of solid samples to other physical quantities, for example the gyromagnetic ratio of NMR nuclei and the effective magnetic moment of the paramagnetic ion by studying the blind sphere radii in lanthanide-doped solid solutions. Moreover, given that doping homogeneity of inorganic phosphors can be traced both *via* the visible signal by lineshape analysis and *via* the fraction of the invisible signal,[21] it is natural to ask whether the blind sphere radius and linewidth or moment analysis can be linked, and if so under which conditions.

Experimental

The $La_{1-x}Ln_xPO_4$ (Ln = Nd, Sm, Gd, Dy, Er, Ho, Tm, Yb) samples have been synthesized *via* a co-precipitation method: Ln_2O_3 (Nd_2O_3 was bought from chemPUR, the rest from smart elements, the purity is 99.999% for Dy_2O_3 and 99.99% for the rest) and La_2O_3 (chemPUR, 99.99%) were dissolved in nitric acid and later on mixed with $NH_4H_2PO_4$ (VWR chemicals) solution. The resulting precipitates were dried at 80 °C overnight, sintered in corundum crucibles at 1000 °C for 4 h.

$Sr_{1-x}Eu_xGa_2S_4$ powders were obtained *via* a solid state synthesis method. Stoichiometric quantities of SrS (Alfa Aesar, 99.9%), Ga_2S_3 (Alfa Aesar, 99.99%) and EuF_3 (Alfa Aesar, 99.5%) were weighed and mixed in an agate mortar. A small amount (1 weight %) of NH_4F (Alfa Aesar, 98+%) was added as a fluxing agent. The mixtures were fired for two hours at 900 °C under a flow of forming gas (90% N_2, 10% H_2). The obtained powder was again lightly ground.

The $(Zn_{1-x}Mn_x)_3(PO_4)_2\cdot4H_2O$ samples have been synthesized by a co-precipitation method: stoichiometric amounts of $MnCl_2\cdot4H_2O$ (ACROS organics, 99+%) and $Zn(NO_3)_2\cdot6H_2O$ (chemPUR, 98+%) were dissolved into water and mixed with an excess of $NH_4H_2PO_4$ (VWR chemicals) in aqueous solution. The precipitates were washed with water and ethanol and dried overnight.

Powder X-ray diffraction (XRD) measurements were performed on a Huber G621 diffractometer with Cu $K_{\alpha1}$ radiation (λ = 0.15405931 nm) in transmission geometry. Diffractograms were extracted from the image files, which were obtained by scanning the photostimulable $BaBrF:Eu^{2+}$ films with an image plate detector (Typhoon FLA 7000, λ = 650 nm), by home-written program ipreader-0.9. The Rietveld analysis was performed *via* the program TOPAS-Academic (TOtal PAttern Solution, by Coelho Software, V4.1).

The solid state NMR measurements were performed on a Bruker Avance II spectrometer at a magnetic field of 7.05 T. Magic angle spinning (MAS) was done with 4 mm pencil rotors at spinning frequencies of 10 kHz or 12.5 kHz with a home-built McKay probe head. The dead time delay was set to 15 μs. Quantification was assisted by a micro-balance (Sartorius MC5). The deconvolution of peaks and moment analysis were assisted with the program deconv2Dxy[48] (version 0.4). The NMR visibility fitting function[21] for a homogeneously doped sample is defined as follows.

$$f(x) = \exp(-ar_0^3x) \tag{1}$$

The wipe-out radius r_0 relates to the size of the blind sphere of a paramagnetic centre and the variable a is host-specific number ($a = 4\pi N_{hostUC}/3V_{UC}$ where N_{hostUC} is the number of "dopable" sites in the unit cell and V_{UC} is the volume of the unit cell). For monazite[49] $LaPO_4$ the variable a amounts to 0.055 Å^{-3}. The doping concentration x in this work is defined as the degree of substitution, which is dimensionless. The experimental NMR visibility f was calculated in the following way: first the molar peak areas $P = A/n$ were calculated for all samples in one dopant series (A peak area, n amount of material).

10186 | *Phys. Chem. Chem. Phys.*, 2019, **21**, 10185–10194

This journal is © the Owner Societies 2019

The visibility function $f(x)$ and $P(x)$ are related by normalization through the undoped sample, *i.e.* $P(x) = f(x) \cdot P(0)$. Therefore the experimental P values were fitted with the function $P(x)$ to determine the free parameters r_0 and $P(0)$. This approach gives equal weight to all measured points. The diagrams (Fig. 2, 4, 7 and 8) show $P(x)/P(0)$ on the y-axis.

Results and discussion

The target of this contribution is to provide a better understanding of the blind sphere in solids. In order to achieve that, measurements have been performed on three model compounds series, Ln^{3+} (Ln = Nd, Sm, Gd, Dy, Er, Ho, Tm, Yb) doped monazite $LaPO_4$, Mn^{2+} doped hopeite $Zn_3(PO_4)_2 \cdot 4H_2O$ and Eu^{2+} doped $SrGa_2S_4$. Lanthanide doped xenotime YPO_4 and monazite $LaPO_4$ have been subject to several studies[50,51] in terms of a determination of NMR parameters. Lanthanide dopants have the advantage that for a model study chemical interference is reduced to a minimum because of the low lying, unpaired f-shell electrons. To extract the sizes of blind spheres from measured data, approaches which relate the peak area and lineshape to the doping level are investigated. Finally, the obtained sizes are compared to establish relations between blind sphere and physical quantities, for example magnetic moment and gyromagnetic ratio.

Peak area and blind sphere

To judge the quality of obtained samples X-ray diffraction was applied. The synthesized samples were phase pure according to X-ray diffraction. Rietveld refinements of the diffraction pattern yielded lattice parameters which followed Vegard's law.[52] Fig. 1 shows the lattice parameters of $La_{1-x}Sm_xPO_4$ follow a linear dependence on the doping concentration x as an example. Such a fulfilment of Vegard's law is often considered as evidence for a homogeneously doped phase pure sample in the sense of a solid solution.

The single pulse ^{31}P MAS NMR spectra offer information on the change of peak area upon increasing the doping level x. Based on the visibility function[21] $f(x) = \exp(-ar_0^3 x)$ blind sphere radii for trivalent dopants Ln^{3+} (Ln = Nd, Gd, Dy, Er, Ho, Tm, Yb) could be obtained (Fig. 2 and Table 1).

While in principle blind sphere radii can be determined from two points only, we fitted the visibility function to all points (experimental part). Because of the discrete nature of the pair distribution function in crystalline materials, radii determined this way become less reliable the smaller the blind-sphere radius (see discussion in ref. 21).

Line shape and blind sphere

While the visibility function $f(x) = \exp(-ar_0^3 x)$ proved to be a useful tool for the extraction of blind-sphere radii in the cases above and in case of $Sr_{1-x}Eu_xH_2$,[21] it could not be applied in case of $La_{1-x}Sm_xPO_4$, because single pulse ^{31}P MAS NMR (Fig. 3) recovers (Fig. 4) signals from all ^{31}P atoms including those of the first coordination sphere around Sm^{3+}, as can be
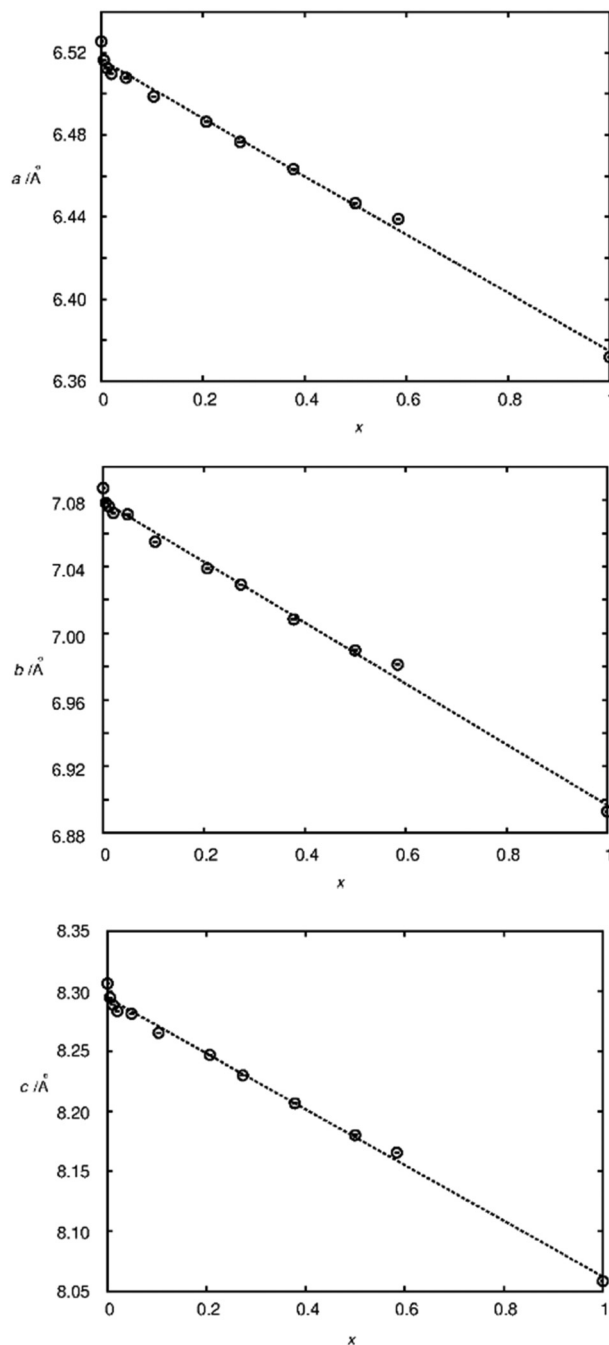
Fig. 1 Lattice parameters as a function of the substitution degree x in $La_{1-x}Sm_xPO_4$, as determined by Rietveld refinement based on X-ray powder diffraction data. The dotted lines represent linear fits resulting in $a/Å = 6.516 − 0.142 \cdot x$, $b/Å = 7.0794 − 0.183 \cdot x$, $c/Å = 8.294 − 0.232 \cdot x$.

seen from the visibility function (Fig. 4 in circles) which stays close to 100% for all doping concentrations x.

Because of line broadening, precise deconvolution of different environments is difficult for $x > 0.1$. Despite the large errors from peak deconvolution, an analysis was attempted to relate line width and doping concentration (ESI,† Fig. S1) as previously done on similar systems in literature,[17,18] however, a linear dependence could not be found. On the other hand a signal specific
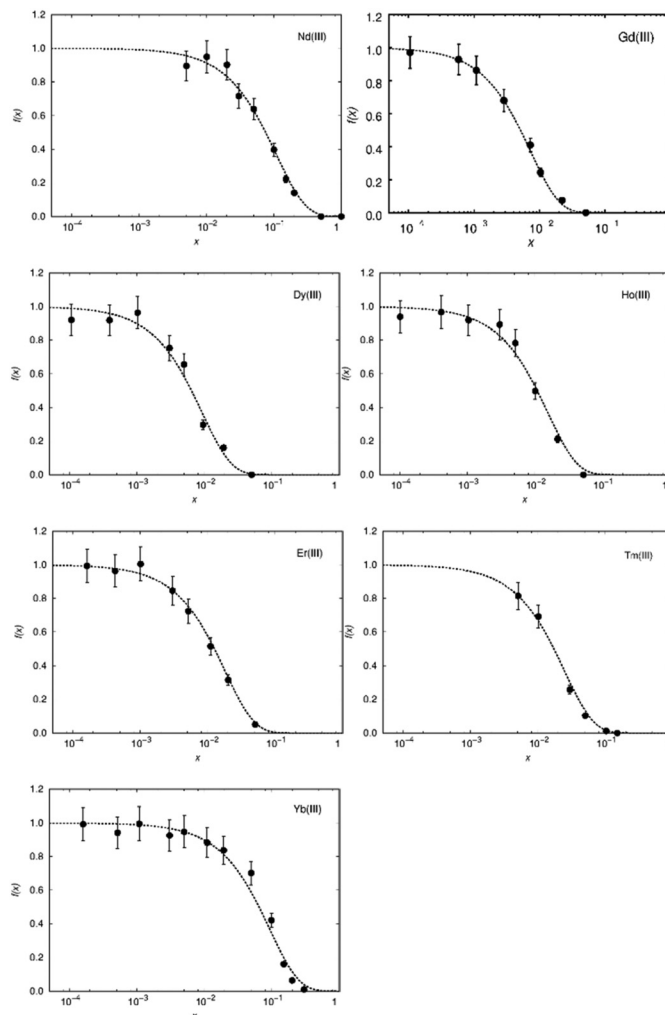
Fig. 2 Normalized visibility function f (circles with error bars) calculated from ^{31}P MAS NMR data plotted against the substitution degree x in $La_{1-x}Ln_xPO_4$, on a logarithmic scale. The dashed line corresponds to the fitting function $f(x) = \exp(-ar_0^3 x)$ with $a = 0.055$ Å^{-3} and $r_0 = 5.5, 13.5, 12.5, 10.5, 10, 9$ and 5.8 Å for Ln = Nd, Gd, Dy, Ho, Er, Tm and Yb, respectively.

Table 1 Radii of blind spheres r_0 obtained from ^{31}P MAS NMR of $La_{1-x}Ln_xPO_4$ sample series, the effective magnetic moments[53] $\mu_{eff}$ in equivalents of the Bohr magneton μ_B and the number of unpaired 4f electrons $N_{unpaired}$ for comparison; r_0 determined by peak area method except for "*" where an estimate from second moment analysis is reported (see main text)

Dopant ion	r_0/Å	μ_{eff}/μ_B	$N_{unpaired}$
Nd^{3+}	5.5	3.62	3
Sm^{3+}	0.45*	1.54	5
Gd^{3+}	13.5	7.95	7
Dy^{3+}	12.5	10.5	5
Ho^{3+}	10.5	10.5	4
Er^{3+}	10.0	9.55	3
Tm^{3+}	9.0	7.5	2
Yb^{3+}	5.8	4.4	1

Fig. 3 Stack plot of ^{31}P MAS NMR spectra of $La_{1-x}Sm_xPO_4$ (x values are marked on the corresponding spectra, dashed line indicates the position of the peak of pure $LaPO_4$).

^{31}P visibility function f can be defined, which corresponds only to the area of the peak which has a similar shift and linewidth as the peak of pure host material $LaPO_4$ (Fig. 4, triangles). A radius of 4.5 Å could in principle be obtained this way which as expected covers the P-atoms in the first coordination sphere around the La atom.

A practical approach which works for any kind of lineshape is to calculate the second moment from the lineshape as suggested by Van Vleck[30] in the context of dipolar peak broadening on whole spectra, which does not rely on the separation of different environments. This dipolar broadening includes

10188 | Phys. Chem. Chem. Phys., 2019, 21, 10185–10194

This journal is © the Owner Societies 2019
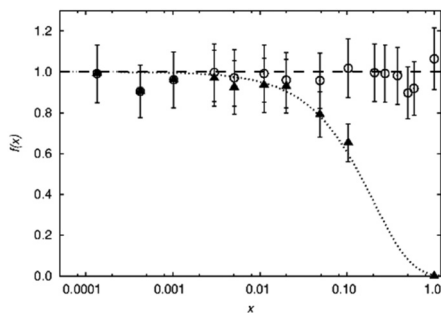
Fig. 4 Normalized visibility $f(x)$ of the ^{31}P MAS NMR signal of $La_{1-x}Sm_xPO_4$. The circles represent the $f(x)$ values calculated from whole peak area, which scatter around 100% (dashed line). The triangles represent the $f(x)$ values from the sharp component which has a similar isotropic chemical shift value as the pure $LaPO_4$. The dotted line refers to the fitting function $f(x) = \exp(-ar_0^3x)$ with $a = 0.055$ Å^{-3} and $r_0 = 4.5$ Å. Note that this r_0 does not follow the definition used in the rest of this contribution.

broadening by magnetic dipolar couplings because of the hyperfine coupling. In case of $La_{1-x}Sm_xPO_4$ the second moment M_2/Hz^2 follows the doping concentration x in a linear way over a wide range (Fig. 5).

To explain the observed linear relation, a brief discussion of line shape functions and line broadening mechanisms may be helpful. For an idealized free induction decay (FID) of a single nucleus the decay function can be expressed for example as a Gaussian or monoexponentially decaying function. The Fourier transformation of such a FID returns a Gaussian or Lorentzian line shape, respectively. When a resonance is broadened homogeneously, for example by relaxation *i.e.* by random oscillatory local field components at the Larmor frequency[54] or by lifetime broadening,[29] then the Lorentzian function is a good basis for the description of the line-shape in the frequency domain. On the other hand, inhomogeneous broadening,[55,56] which can be caused for example by magnetic field inhomogeneity, chemical shift anisotropy (CSA) or pseudo-contact term, produces a more complicated, often asymmetric lineshape, for which the description by van Vleck's moment approach is a suitable analysis tool. In van Vleck's moment approach, the dipolarly broadened spectral lineshape is decomposed into a sum of Gaussian functions. Hole-burning[57–59] experiments allow to distinguish inhomogeneous from homogeneous broadening.
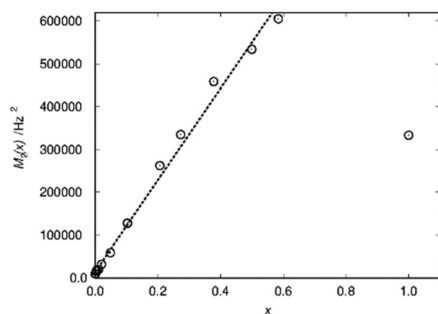

Fig. 5 Second moment $M_2(x)$ as a function of the substitution degree x in $La_{1-x}Sm_xPO_4$. The dotted line represents linear fit resulting in $M_2/Hz^2 = 1.4 \times 10^4 + 1.07 \times 10^6 \cdot x$.
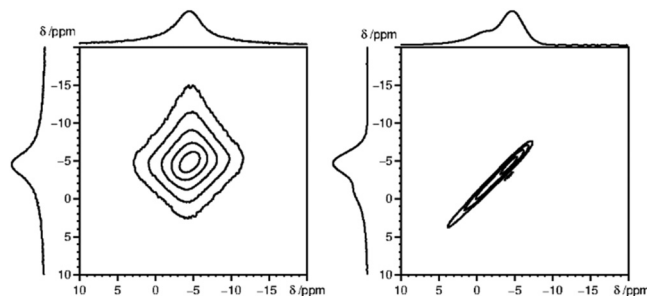

Fig. 6 2D ^{31}P MAS EXSY spectra (with zero mixing time) for $La_{0.997}Gd_{0.003}PO_4$ (left) and $La_{0.99}Sm_{0.01}PO_4$ (right), which depicted homogeneous and inhomogeneous type of line broadening, respectively.

A simple alternative to the hole-burning experiment is the 2D exchange spectroscopy (EXSY) experiment. EXSY experiments with zero mixing time show a sharp ridge on the diagonal in case of inhomogeneous broadening and a double Lorentzian type lineshape in case of homogeneous broadening. Note that the EXSY looks the same and behaves like the stimulated echo experiment. From the ^{31}P MAS NMR 2D spectra (Fig. 6), it is clear that the ^{31}P 2D NMR signal observed for Sm^{3+} doped $LaPO_4$ is typical for inhomogeneous broadening, while for Gd^{3+} homogeneous broadening is observed. The ^{31}P NMR signals for the other measured Ln^{3+} doped samples, namely Nd^{3+}, Dy^{3+}, Ho^{3+}, Er^{3+}, Tm^{3+} and Yb^{3+}, all show an inhomogeneous broadening behaviour (ESI,† Fig. S2).

In the following, a relation between the blind-sphere radius and the observed line-broadening is developed for simple cases.

The peak area which is the basis of the visibility function $f(x)$ (see above) is related to the intensity of first point of the FID according to the integral theorem of the Fourier transformation.[56] Any loss in peak area should then be reflected by the decay of the FID during the dead-time delay t_{de}, either by relaxation or by coherent mechanisms. If spectral line-broadening is assumed to be following a simple Lorentzian or Gaussian function then the decay in the FID needs to be monoexponential or Gaussian, respectively. Thus for simple cases the blind-sphere radius and line-broadening follow simple analytical expressions for a given dead-time delay (see below).

A Gaussian type FID $s_G(t)$ of an on-resonance signal is described with a linewidth parameter λ_G and the amplitude factor $s_{G,0}$.

$$s_G(t) = s_{G,0} \exp(-\lambda_G^2 t^2) \tag{2}$$

The corresponding spectral function $I_G(\omega)$ is obtained by a single-sided complex Fourier transformation.[56]

$$I_G(\omega) = \frac{1}{\pi}\int_0^\infty s_G(t)e^{-i\omega t}dt$$
$$= \frac{s_{G,0}}{\sqrt{\pi}2\lambda_G}\exp\left(-\frac{\omega^2}{4\lambda_G^2}\right)\left[1 - i\,\mathrm{erfi}\left(\frac{\omega}{2\lambda_G}\right)\right] \tag{3}$$

The line width parameter λ_G is related to the full width half-maximum of the line-shape in Hz as $\lambda_G = \frac{\pi}{2\sqrt{\ln2}}\Delta\nu_G^{FWHM}$.

Given the lineshape of a paramagnetically doped sample can be described with a simple Gaussian function then the peak area A_G for a given dead time t_{de} can be predicted on the basis of the integral theorem[56] of the Fourier transformation from the decay of the FID.

$$A_G = s_{G,0} \exp[-\lambda_G^2 t_{de}^2] \qquad (4)$$

In order to derive the visibility function $f(x)$ in terms of line-broadening $\lambda_G(x)$, eqn (4) is plugged into the definition of the visibility function.

$$f_G(x) \underset{=}{\mathrm{def}} \frac{A_G(x)}{A_G(0)} = \frac{s_{G,0} \exp\left[-\lambda_G^2(x)t_{de}^2\right]}{s_{G,0} \exp\left[-\lambda_G^2(0)t_{de}^2\right]}$$
$$= \exp\left\{-t_{de}^2\left[\lambda_G^2(x) - \lambda_G^2(0)\right]\right\} \qquad (5)$$

The amplitude factor $s_{G,0}$ of the doped and the pure host material should the equal, while the line width parameter $\lambda_G(x)$ depends on doping concentration. The visibility function can also be expressed in terms of the blind sphere radii r_0, the number density parameter a and doping level x (eqn (1)). Therefore, the link between parameter λ_G and doping level x can be established as follows.

$$\lambda_G^2(x) - \lambda_G^2(0) = \frac{ar_0^3}{t_{de}^2}x \qquad (6)$$

Assuming a negligible frequency difference between signals, the second moment[48,56] $M_2 = \int \omega^2 I(\omega)d\omega$ of the Gaussian type function is $2\lambda_G^2$ and the second moment becomes $M_2(x) = 2\lambda_G^2(x)$. Eqn (6) can be rewritten in terms of the second moment.

$$M_2(x) = M_2(0) + \frac{2ar_0^3}{t_{de}^2}x \qquad (7)$$

A linear regression of the second moment $M_2(x)$ yields the slope $k_G = \frac{2ar_0^3}{t_{de}^2}$. From the latter the radius of the blind sphere r_0 can be estimated *via* a simple analytical equation.

$$r_0 = \sqrt[3]{\frac{k_G t_{de}^2}{2a}} \qquad (8)$$

This way the blind-sphere r_0 of Sm^{3+} doped $La_{1-x}Sm_xPO_4$ was estimated to be 0.45 Å. The La to P and Sm to P distances in the monazite[49] structure of $LaPO_4$ and $SmPO_4$ are 3.2 Å and 3.1 Å, respectively, which means that all ^{31}P nuclei are outside of the blind spheres of Sm^{3+} and thus visible. This is consistent with the observation the signal visibility function $f(x)$ remains close to 100% (Fig. 4). In addition, ^{19}F and ^1H NMR signals for SmF_3[60] and SmH_3[61,62] both have been reported to be visible, which supports the found small blind sphere size of Sm^{3+}. Given the estimated blind sphere radius is even smaller than the Shannon radius[63] for Sm^{3+} (around 1 Å) it appears that Sm-compounds in general are good candidates for NMR studies, because no signal loss is expected. The second moment analysis as presented above can provide information on the size of the blind sphere, especially for paramagnetic dopants which have small blind spheres.

For Gd^{3+}, the line broadening is mainly based on the homogeneous broadening mechanism which is relaxation dominated and follows a Lorentzian lineshape. Thus the FID can be described with a monoexponentially decaying function. The line width parameter $\lambda_L(x)$ then has a slightly different relation to the blind sphere r_0, doping concentration x and deadtime delay t_{de} (see ESI†).

$$\lambda_L(x) - \lambda_L(0) = \frac{2ar_0^3}{t_{de}}x \qquad (9)$$

The $\lambda_L(x)$ is related to the full width half-maximum in Hz as $\lambda_L = 2\pi\Delta\nu_L^{FWHM}$.

The relation between the size of blind sphere r_0 and the experimental results $\lambda_L(0)$ (the line width of non-doped diamagnetic analog) and slope k_L value (from the linear fit of $\lambda_L(x)$ against x) can be derived in a similar fashion as in the Gaussian case.

$$r_0 = \sqrt[3]{\frac{k_L t_{de}}{2a}} \qquad (10)$$

This way the blind sphere r_0 for the Gd^{3+} doped sample becomes 6.7 Å, which is much smaller than the estimated 13.5 Å from signal visibility method. This discrepancy can be explained by the inadequacy of simple functions to describe the FID. In case the spectral lineshape function becomes more complicated it is non-trivial to extract line-width parameters from the spectra and in those cases the visibility function $f(x)$ provides an easier way to determine blind-sphere radii. As shown above line-shape analysis requires knowledge about the decay character of the FID in order to determine the blind sphere radius. The reported[17,18] linear relation of doping concentration x and linewidth is only expected in case of Lorentzian type spectral lineshapes. While the derivation of blind-spheres *via* a line-shape analysis suffers from a number of approximations including the assumption of a sharp transition of the visible to invisible nuclei, we believe that the scaling behaviour of the doping concentration x with respect to second moment and line-width, is the most important insight that is being conveyed by the above analysis.

Blind sphere radius dependence on the gyromagnetic ratio

In order to investigate the size dependence of the blind sphere on the gyromagnetic ratio γ, data obtained from the same paramagnetic ion but different NMR nuclei are compared (Table 2). In the following we assume that Eu^{2+} and Gd^{3+} are isoelectronic paramagnetic ions, and thus have equal blind sphere radii. The concept of the blind-sphere is based on the idea that the signals of all atoms inside the sphere vanish in the dead-time delay, *i.e.* nuclei which are situated on the blind sphere have a critical relaxation rate, a critical amount of line-broadening or paramagnetic shift. Critical relaxation rates R_{1M} and R_{2M} driven by a dipolar coupling mechanism with unpaired electrons or Curie nuclear spin relaxation are then proportional to γ^2/r_0^6,[39] while critical broadening through the pseudo-contact shift (PCS) relates to γ/r_0^3.[39] Given that other influences, like the spectral density, are negligible, it can be concluded that the prefactors which relate to the critical broadening or

10190 | *Phys. Chem. Chem. Phys.*, 2019, **21**, 10185–10194

This journal is © the Owner Societies 2019

Table 2 The blind sphere radii r_0 values for different NMR nuclei obtained with the visibility method; γ is the nuclei gyromagnetic ratio; $r_0(^{31}P)$ is the blind-sphere radius of a virtual ^{31}P nucleus converted from experimental r_0 via the eqn (11)

Host	NMR nucleus	$\gamma/10^7$ rad T^{-1} s^{-1}	$a/\text{Å}^{-3}$	Dopant	$r_0/\text{Å}$	$r_0(^{31}P)/\text{Å}$
SrH_2	^1H	26.75	0.092	Eu^{2+}	17^{21}	12.6
$SrGa_2S_4$	^{71}Ga	8.18	0.025	Eu^{2+}	13	14.3
$LaPO_4$	^{31}P	10.84	0.055	Gd^{3+}	13.5	—
$Zn_3(PO_4)_2\cdot 4H_2O$	^1H	26.75	0.051	Mn^{2+}	10	7.4
$Zn_3(PO_4)_2\cdot 4H_2O$	^{31}P	10.84	0.051	Mn^{2+}	7	—

relaxation rate would feature the same relation of gyromagnetic ratio γ to blind sphere radius r_0. In this case the blind sphere radii for different nuclei X and Y in the same compound should feature a cubic root dependence to the gyromagnetic ratio.

$$r_{0,X}/r_{0,Y} = \sqrt[3]{\gamma_X/\gamma_Y} \qquad (11)$$

To test this hypothesis we compare blind-sphere radii from different nuclei in the same and in different compounds. The visibility method yielded a blind sphere radius from ^{71}Ga NMR for Eu^{2+} in $Sr_{1-x}Eu_xGa_2S_4$ (Fig. 7). This may be compared with a blind sphere for Eu^{2+} in $Sr_{1-x}Eu_xH_2$ from ^1H NMR[21] and with one for Gd^{3+} in $La_{1-x}Gd_xPO_4$ from ^{31}P NMR (Fig. 2). The values converted to the blind sphere via eqn (11) of a virtual ^{31}P nucleus are the same (Table 2) within approximated error limits. Given the low number of values in the comparison this is a weak indication that the blind sphere radii of lanthanide dopants may be abstracted from the host structure.

In a second example the sphere radius of Mn^{2+} is detected by ^1H and ^{31}P NMR in hopeite $(Zn_{1-x}Mn_x)_3(PO_4)_2\cdot 4H_2O$ (Fig. 8). Again the virtual radius of ^{31}P converted from the radius applying to the ^1H nucleus agrees to the observed value within error limits (Table 2). Deviations from this fairly good agreement are expected especially in case of a Fermi-contact contribution[64,65] which however does not seem to be relevant here. Another explanation in case of a relaxation dominated blind sphere may be the change of the electronic relaxation mechanism at high doping concentrations which in principle could even lead to an increase visibility in the high concentration regime. In some cases of transition metal doping even at very high dopant concentration[64,65] the signal does not vanish.
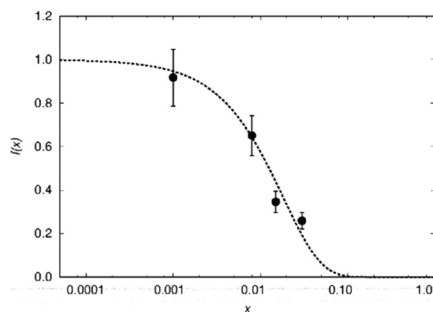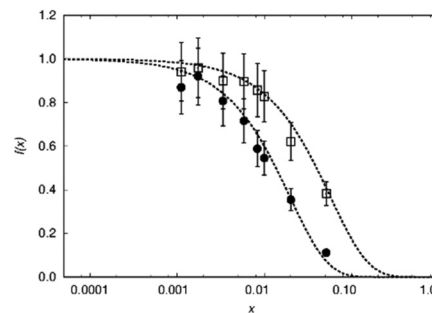

Fig. 8 Normalized NMR visibility function $f(x)$ on a logarithmic scale for x for $(Zn_{1-x}Mn_x)_3(PO_4)_2\cdot 4H_2O$. $f(x)$ data obtained from ^1H NMR are plotted as circles while those from ^{31}P NMR as squares. The dashed lines feature the fitted functions $f(x) = \exp(-ar_0^3 x)$ with $a = 0.051/\text{Å}^3$, $r_0 = 10$ Å and 7 Å for ^1H and ^{31}P, respectively.

In the presented cases of lanthanide(III) doped monazite the only system where we have an indication of a relaxation dominated blind sphere radius is Gd(III). At 100% doping, i.e. pure $GdPO_4$ no intensity increase can be observed, in line with the presented interpretation.

Blind sphere radius dependence on the effective magnetic moment

In order to test the hypothesis that blind sphere radius depends on the effective magnetic moment, data obtained from the same host $LaPO_4$ and the same NMR nucleus (^{31}P) but different paramagnetic dopants are compared. Relaxation and hyperfine shift are two possible origins of blind spheres, and are discussed resonances in $La_{1-x}Ln_xPO_4$ are inhomogeneously broadened for all Ln^{3+} dopants except Gd^{3+}, which indicates that relaxation is dominant in the case of doping by Gd^{3+} but not as important in case of other paramagnetic Ln^{3+} as is explained in detail in the following paragraph.

Relaxation

Dipolar, Curie-spin and Fermi-contact relaxation are in principle three possible relaxation contributions in paramagnetic systems which lead to homogeneous line broadening. For solid crystalline $La_{1-x}Ln_xPO_4$, chemical exchange and stochastic reorientation are negligible, only vibrational motions exert efficient influence on the electronic relaxation. Based on the Solomon–Bloembergen–Morgan relaxation model,[66,67] the nuclear transverse relaxation time T_2 can be described as eqn (12) for lanthanide ions induced paramagnetic relaxation enhancement (PRE). Parameter A^{FC} is the Fermi-contact coupling and $b_{JI} = \dfrac{\mu_0 \mu_B g_J \hbar \gamma_I}{4\pi R^3}$ is the spin-dipolar coupling parameter.[67] T_{1e} and T_{2e} are the longitudinal and transverse electronic relaxation times, respectively, which are used to approximate the corresponding electronic correlation times.[67] ω_I and ω_S are the nuclear and electronic Larmor frequencies, respectively. J is the main total angular momentum quantum number. R is the distance between NMR nuclei and the unpaired electrons which belong to the paramagnetic ion and are assumed to be localized on the lanthanide ion (point-dipole approximation).

Fig. 7 Normalized NMR visibility function $f(x)$ on a logarithmic scale for x for $Sr_{1-x}Eu_xGa_2S_4$ (circles). The dashed line corresponds to the fitted function $f(x) = \exp(-ar_0^3 x)$ with $a = 0.025/\text{Å}^3$ and $r_0 = 13$ Å.

The γ_I is the nuclear gyromagnetic ratio and g_J is the isotropic Born–Landé g-factor.

$$\frac{1}{T_2} = \frac{1}{3}J(J+1)\left(\frac{A^{FC}}{\hbar}\right)^2\left[T_{1e} + \frac{T_{2e}}{1 + (\omega_S - \omega_I)^2 T_{2e}^2}\right]$$
$$+ \frac{1}{15}J(J+1)\left(\frac{b_{JI}}{\hbar}\right)^2\left[4T_{1e} + \frac{6T_{2e}}{1 + \omega_S^2 T_{2e}^2}\right.$$
$$\left. + \frac{3T_{1e}}{1 + \omega_I^2 T_{1e}^2} + \frac{6T_{2e}}{1 + (\omega_S + \omega_I)^2 T_{2e}^2} + \frac{T_{2e}}{1 + (\omega_S - \omega_I)^2 T_{2e}^2}\right] \quad (12)$$

The first term in this equation is caused by Fermi-contact coupling and lacks a simple relation to the blind-sphere radius. The second term, called pseudo-contact term, is caused by a direct dipole–dipole interaction and has a distance dependence of R^{-6}. At the critical relaxation rate (neglecting the Fermi contact contribution) the second term is proportional to $b_{JI}^2 J(J + 1)$ or expressed with the effective magnetic moment $\mu_{eff} = g_J\mu_B\sqrt{J(J+1)}$ (Landé formula) proportional to $\mu_{eff}^2 R^{-6}$. The electronic relaxation times in solids are driven by vibrational motions and differ by the lanthanide ion. Published ranges[39,67] of the electronic relaxation times show only minor differences for lanthanides Ln^{3+} (Ln = Sm, Nd, Yb, Tm, Er and Ho) with the exception of Gd^{3+} (see Table 8.6 in ref. 67) for which electronic relaxation rates are several orders of magnitude lower than for the other paramagnetic lanthanide ions, which causes efficient nuclear transversal relaxation and is consistent with the magnitude of the linewidth (few hundreds to kHz) observed from the EXSY (Fig. 6) and single pulse measurements. Note that the EXSY experiment with a very short mixing time behaves like a stimulated echo and provides information about transversal relaxation over the complete linewidth. For the other Ln^{3+} ions, the observed line broadening (Fig. 6 and ESI,† Fig. S2) is of the order of ten to a hundred Hz. This is much larger than the expected relaxation-induced line broadening which indicates relaxation not to be the predominant source of broadening. This interpretation is in agreement with the observation that the line broadening for Gd^{3+} is homogeneous while the other Ln^{3+} dopants generate inhomogeneous line broadening and explains the exceptional role of Gd^{3+} in the Fig. 9 and 10.

Paramagnetic shift

Besides relaxation, another possible origin for blind sphere is the paramagnetic shift δ_{param}. The inhomogeneous line-broadening observed on the ^{31}P resonances indicates that the paramagnetic shift is the relevant origin for the blind spheres of $LaPO_4$ doped with Ln^{3+} (Ln = Nd, Sm, Dy, Er, Ho, Tm, Yb), but not for $LaPO_4$ doped with Gd^{3+}. Different mechanisms may cause a paramagnetic isotropic or anisotropic shift, which have been subject to a recent review.[67] In order to compare the relative size of paramagnetic shift in a lanthanide series Bleaney,[68] Golding and Halton[69] have developed an approach in which they separate the electronic term C from a coupling term.
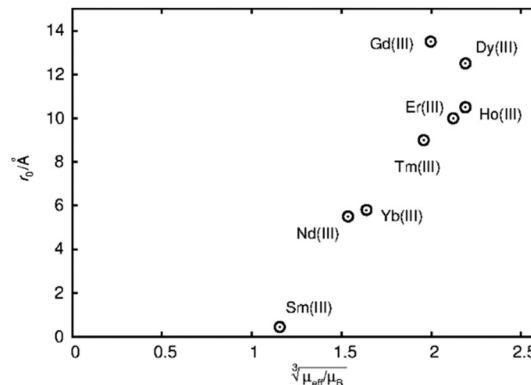

Fig. 9 Blind sphere radii for Ln(III) dopants of $La_{1-x}Ln_xPO_4$ series, plotted against $\sqrt[3]{\mu_{eff}/\mu_B}$. The μ_{eff} and μ_B refer to effective magnetic moment[53] and Bohr magneton, respectively.
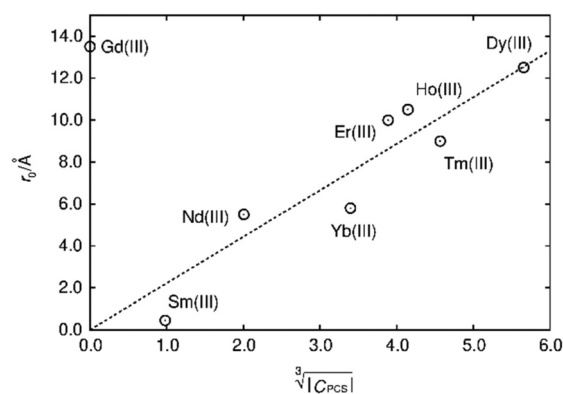

Fig. 10 Blind sphere radii for Ln(III) dopants of $La_{1-x}Ln_xPO_4$ series, plotted against $\sqrt[3]{|C_{CPS}|}$. $|C_{PCS}|$ refers to the magnitude of electronic contribution from pseudo-contact shielding.[67,68] The dashed line features the fitting function $r_0/\text{Å} = 2.22 \cdot \sqrt[3]{|C_{PCS}|}$ with the coefficient of determination $R^2 = 0.89$.

The size of the electronic term can be described by a real number and was tabulated by Pell et al.[67] for the contact shift C_{con}, the pseudo-contact shift $C_{PCS} = g^2 J(J + 1)(2J - 1)(2J + 3)\langle J||\alpha||J\rangle$[67] and the shielding anisotropy C_{SA} (Table 3). Given that a critical broadening or shift exists (see above) which defines the blind-sphere radius r_0, it should be possible to obtain a linear relation between $\sqrt[3]{|C_{PCS}|}$ and the blind sphere radius r_0. In fact a good correlation is observed (Fig. 10), with the expected exception of Gd^{3+} (see above). For completeness we have also plotted the blind-sphere radius vs. $\sqrt[3]{|C_{SA}|}$ (ESI,† Fig. S3) and $\sqrt[3]{|C_{con}|}$ (Fig. S4, ESI†). The observed excellent empirical correlation in case of the contact interaction lacks a good explanation, though. It should not be overinterpreted as it is caused by the drastic change of a single measurement, i.e. on $La_{1-x}Gd_xPO_4$ for which relaxation is expected to have a big influence.

To sum up, for Ln^{3+} both relaxation (in case of Gd^{3+}) and the paramagnetic shift (in case of the other presented Ln^{3+}) give an explanation for the origin of the blind sphere. The pseudo-contact term provides a simple explanation for the change of

10192 | *Phys. Chem. Chem. Phys.*, 2019, **21**, 10185–10194

This journal is © the Owner Societies 2019

Table 3 Radii of blind spheres r_0 obtained from ^{31}P MAS NMR of $La_{1-x}Ln_xPO_4$ sample series, and corresponding Ln^{3+} hyperfine contributions.[67] $|C_{SA}|$, $|C_{con}|$ and $|C_{PCS}|$ refer to the electronic contribution to the paramagnetic shift from shielding anisotropy, contact and pseudo-contact term, respectively

Dopant ion	$r_0^A/\text{Å}$	$|C_{SA}|$	$|C_{con}|$	$|C_{PCS}|$
Nd^{3+}	5.5	13.1	4.5	8.08
Sm^{3+}	0.45	0.7	0.063	0.94
Gd^{3+}	13.5	63	31.5	0
Dy^{3+}	12.5	113.3	28.5	181
Ho^{3+}	10.5	112.5	22.6	71.3
Er^{3+}	10.0	91.8	15.4	58.8
Tm^{3+}	9.0	57.2	8.2	95.3
Yb^{3+}	5.8	20.6	2.6	39.2

the blind-sphere radius in a lanthanide series and predicts a $r_0 \propto \sqrt[3]{|\mu_{eff}|}$ dependence for relaxation and a $r_0 \propto \sqrt[3]{|C_{PCS}|}$ dependence for the paramagnetic shift, of which the latter is confirmed by the experiment.

Conclusions

In this work, sizes of blind spheres r_0 have been determined from NMR spectra by two methods: signal visibility decay function and lineshape analysis. A formula for the blind sphere radius could be derived, that relates the radii of blind sphere to the lineshape for a given dead time of the spectrometer, which allows to estimate blind-sphere radii even when the visibility remains close to 100% over the complete doping range.

The dependence of blind sphere radii on the effective magnetic moment of the dopant ions and on the nucleus give insight into processes leading to a blind-sphere and provide estimates for blind sphere radii upon switching the dopant in a lanthanide series or the nucleus. Blind-sphere radii up to 13 Å suggest that a significant amount of material may remain virtually invisible in NMR, while certain paramagnetic ions, like Sm^{3+}, allow the detection of NMR signal even from atoms two bonds away from paramagnetic centre. These results are relevant for evaluating the paramagnetic doping homogeneity of inorganic phosphors and their optical performance and to estimate which nuclei around a paramagnetic centre can directly be observed, for example in dynamic nuclear polarization (DNP) NMR or by direct detection.

Conflicts of interest

There are no conflicts to declare.

References

1 I. Bertini, P. Turano and A. J. Vila, *Chem. Rev.*, 1993, **93**, 2833–2932.
2 I. Bertini, C. O. Fernández, B. G. Karlsson, J. Leckner, C. Luchinat, B. G. Malmström, A. M. Nersissian, R. Pierattelli, E. Shipp, J. S. Valentine and A. J. Vila, *J. Am. Chem. Soc.*, 2000, **122**, 3701–3707.
3 C. Öster, S. Kosol, C. Hartlmüller, J. M. Lamley, D. Iuga, A. Oss, M.-L. Org, K. Vanatalu, A. Samoson, T. Madl and J. R. Lewandowski, *J. Am. Chem. Soc.*, 2017, **139**, 12165–12174.
4 E. Ravera, G. Parigi and C. Luchinat, *J. Magn. Reson.*, 2017, **282**, 154–169.
5 L. Cerofolini, T. Staderini, S. Giuntini, E. Ravera, M. Fragai, G. Parigi, R. Pierattelli and C. Luchinat, *JBIC, J. Biol. Inorg. Chem.*, 2018, **23**, 71–80.
6 J. Kim, D. S. Middlemiss, N. A. Chernova, B. Y. X. Zhu, C. Masquelier and C. P. Grey, *J. Am. Chem. Soc.*, 2010, **132**, 16825–16840.
7 L. Zhou, M. Leskes, A. J. Ilott, N. M. Trease and C. P. Grey, *J. Magn. Reson.*, 2013, **234**, 44–57.
8 X. Li, M. Tang, X. Feng, I. Hung, A. Rose, P.-H. Chien, Z. Gan and Y.-Y. Hu, *Chem. Mater.*, 2017, **29**, 8282–8291.
9 C. A. Lepre, J. M. Moore and J. W. Peng, *Chem. Rev.*, 2004, **104**, 3641–3676.
10 Q. Z. Ni, F. Yang, T. V. Can, I. V. Sergeyev, S. M. D'Addio, S. K. Jawla, Y. Li, M. P. Lipert, W. Xu, R. T. Williamson, A. Leone, R. G. Griffin and Y. Su, *J. Phys. Chem. B*, 2017, **121**, 8132–8141.
11 R. R. Amirov, E. A. Burilova, Y. I. Zhuravleva, A. V. Zakharov and A. B. Ziyatdinova, *Polym. Sci., Ser. C*, 2017, **59**, 133–140.
12 N. J. Brownbill, R. S. Sprick, B. Bonillo, S. Pawsey, F. Aussenac, A. J. Fielding, A. I. Cooper and F. Blanc, *Macromolecules*, 2018, **51**, 3088–3096.
13 C. S. Zuo, K. R. Metz, Y. Sun and A. D. Sherry, *J. Magn. Reson.*, 1998, **133**, 53–60.
14 A. E. Thorarinsdottir, A. I. Gaudette and T. David Harris, *Chem. Sci.*, 2017, **8**, 2448–2456.
15 M. Ilibi, T. B. de Queiroz, J. Ren, L. D. Cola, A. S. S. de Camargo and H. Eckert, *Dalton Trans.*, 2014, **43**, 8318–8330.
16 M. de Oliveira, T. Uesbeck, T. S. Gonçalves, C. J. Magon, P. S. Pizani, A. S. S. de Camargo and H. Eckert, *J. Phys. Chem. C*, 2015, **119**, 24574–24587.
17 T. Harazono, E. Yokota, H. Uchida and T. Watanabe, *Bull. Chem. Soc. Jpn.*, 1998, **71**, 2797–2805.
18 T. Harazono, E. Yokota, H. Uchida and T. Watanabe, *Bull. Chem. Soc. Jpn.*, 1998, **71**, 825–829.
19 T. Harazono, R. Adachi, N. Kijima and T. Watanabe, *Bull. Chem. Soc. Jpn.*, 1999, **72**, 2655–2664.
20 S. Maron, G. Dantelle, T. Gacoin and F. Devreux, *Phys. Chem. Chem. Phys.*, 2014, **16**, 18788–18798.
21 W. Li, V. R. Celinski, J. Weber, N. Kunkel, H. Kohlmann and J. Schmedt auf der Günne, *Phys. Chem. Chem. Phys.*, 2016, **18**, 9752–9757.
22 S. Maron, N. Ollier, T. Gacoin and G. Dantelle, *Phys. Chem. Chem. Phys.*, 2017, **19**, 12175–12184.
23 N. C. George, J. Brgoch, A. J. Pell, C. Cozzan, A. Jaffe, G. Dantelle, A. Llobet, G. Pintacuda, R. Seshadri and B. F. Chmelka, *Chem. Mater.*, 2017, **29**, 3538–3546.
24 L. Russo, M. Maestre-Martinez, S. Wolff, S. Becker and C. Griesinger, *J. Am. Chem. Soc.*, 2013, **135**, 17111–17120.
25 R. J. McCarty and J. F. Stebbins, *Solid State Nucl. Magn. Reson.*, 2016, **79**, 11–22.
26 C. P. Grey, C. M. Dobson, A. K. Cheetham and R. J. B. Jakeman, *J. Am. Chem. Soc.*, 1989, **111**, 505–511.

This journal is © the Owner Societies 2019

Phys. Chem. Chem. Phys., 2019, **21**, 10185–10194 | 10193

27 T. Wittmann, A. Mondal, C. B. L. Tschense, J. J. Wittmann, O. Klimm, R. Siegel, B. Corzilius, B. Weber, M. Kaupp and J. Senker, *J. Am. Chem. Soc.*, 2018, **140**, 2135–2144.

28 A. Mondal, M. W. Gaultois, A. J. Pell, M. Iannuzzi, C. P. Grey, J. Hutter and M. Kaupp, *J. Chem. Theory Comput.*, 2018, **14**, 377–394.

29 A. R. Brough, C. P. Grey and C. M. Dobson, *J. Am. Chem. Soc.*, 1993, **115**, 7318–7327.

30 J. H. Van Vleck, *Phys. Rev.*, 1948, **74**, 1168–1183.

31 P. W. Anderson and P. R. Weiss, *Rev. Mod. Phys.*, 1953, **25**, 269–276.

32 G. W. Parker and F. Lado, *Phys. Rev. B: Solid State*, 1973, **8**, 3081–3092.

33 C. Zhang, T. Uchikoshi, L. Liu, B. Dierre, Y. Sakka and N. Hirosaki, *Appl. Phys. Lett.*, 2014, **104**, 021914.

34 L. I. D. J. Martin, D. Poelman, P. F. Smet and J. J. Joos, *ECS J. Solid State Sci. Technol.*, 2018, **7**, R3052–R3056.

35 V. Bachmann, C. Ronda, O. Oeckler, W. Schnick and A. Meijerink, *Chem. Mater.*, 2009, **21**, 316–325.

36 J. J. Joos, K. W. Meert, A. B. Parmentier, D. Poelman and P. F. Smet, *Opt. Mater.*, 2012, **34**, 1902–1907.

37 V. Bachmann, C. Ronda and A. Meijerink, *Chem. Mater.*, 2009, **21**, 2077–2084.

38 I. Bertini, C. Luchinat, G. Parigi and R. Pierattelli, *ChemBioChem*, 2005, **6**, 1536–1549.

39 I. Bertini, C. Luchinat, G. Parigi and E. Ravera, *NMR of Paramagnetic Molecules: Applications to Metallobiomolecules and Models*, Elsevier, 2016.

40 I. J. Lowe and D. Tse, *Phys. Rev.*, 1968, **166**, 279–291.

41 B. Giovannini, P. Pincus, G. Gladstone and A. J. Heeger, *J. Phys., Colloq.*, 1971, **32**, C1-163.

42 M. Punkkinen, *Phys. Kondens. Mater.*, 1971, **13**, 79–88.

43 B. Corzilius, L. B. Andreas, A. A. Smith, Q. Z. Ni and R. G. Griffin, *J. Magn. Reson.*, 2014, **240**, 113–123.

44 R. Rogawski, I. V. Sergeyev, Y. Zhang, T. H. Tran, Y. Li, L. Tong and A. E. McDermott, *J. Phys. Chem. B*, 2017, **121**, 10770–10781.

45 T. Wolf, S. Kumar, H. Singh, T. Chakrabarty, F. Aussenac, A. I. Frenkel, D. T. Major and M. Leskes, *J. Am. Chem. Soc.*, 2019, **141**, 451–462.

46 A. Bertarello and G. Pintacuda, *Paramagnetism in Experimental Biomolecular NMR*, 2018, pp. 163–188.

47 S. Lange, A. H. Linden, Ü. Akbey, W. Trent Franks, N. M. Loening, B. J. van Rossum and H. Oschkinat, *J. Magn. Reson.*, 2012, **216**, 209–212.

48 D. Jardón-Álvarez and J. Schmedt auf der Günne, *Solid State Nucl. Magn. Reson.*, 2018, **94**, 26–30.

49 Y. Ni, J. M. Hughes and A. N. Mariano, *Am. Mineral.*, 1995, **80**, 21–26.

50 A. C. Palke, J. F. Stebbins and L. A. Boatner, *Inorg. Chem.*, 2013, **52**, 12605–12615.

51 J. F. Stebbins, R. J. McCarty and A. C. Palke, *Acta Crystallogr., Sect. C: Struct. Chem.*, 2017, **73**, 128–136.

52 L. Vegard, *Z. Phys.*, 1921, **5**, 17–26.

53 C. H. Evans, *Biochemistry of the Lanthanides*, Springer Science & Business Media, 2013.

54 G. E. Pake and E. M. Purcell, *Phys. Rev.*, 1948, **74**, 1184–1188.

55 M. M. Maricq and J. S. Waugh, *J. Chem. Phys.*, 1979, **70**, 3300–3316.

56 K. Schmidt-Rohr and H. W. Spiess, *Multidimensional Solid-State NMR and Polymers*, Elsevier, 2012.

57 N. Bloembergen, E. M. Purcell and R. V. Pound, *Phys. Rev.*, 1948, **73**, 679–712.

58 G. A. Morris and R. Freeman, *J. Magn. Reson.*, 1969, **1978**(29), 433–462.

59 P. L. Kuhns and M. S. Conradi, *J. Chem. Phys.*, 1982, **77**, 1771–1778.

60 A. Y. H. Lo, V. Sudarsan, S. Sivakumar, F. van Veggel and R. W. Schurko, *J. Am. Chem. Soc.*, 2007, **129**, 4687–4700.

61 O. J. Żogał, M. Drulis and S. Idziak, *Z. Phys. Chem.*, 1989, **163**, 303–308.

62 O. J. Żogał, S. Idziak, M. Drulis and K. Niedźwiedź, *Phys. Status Solidi B*, 1991, **167**, K55–K58.

63 R. D. Shannon, *Acta Crystallogr., Sect. A: Cryst. Phys., Diffr., Theor. Gen. Crystallogr.*, 1976, **32**, 751–767.

64 F. C. Strobridge, D. S. Middlemiss, A. J. Pell, M. Leskes, R. J. Clément, F. Pourpoint, Z. Lu, J. V. Hanna, G. Pintacuda, L. Emsley, A. Samoson and C. P. Grey, *J. Mater. Chem. A*, 2014, **2**, 11948–11957.

65 I. D. Seymour, D. S. Middlemiss, D. M. Halat, N. M. Trease, A. J. Pell and C. P. Grey, *J. Am. Chem. Soc.*, 2016, **138**, 9405–9408.

66 N. Bloembergen and L. O. Morgan, *J. Chem. Phys.*, 1961, **34**, 842–850.

67 A. J. Pell, G. Pintacuda and C. P. Grey, *Prog. Nucl. Magn. Reson. Spectrosc.*, 2019, **111**, 1–271.

68 B. Bleaney, *J. Magn. Reson.*, 1972, **8**, 91–100.

69 R. M. Golding and M. P. Halton, *Aust. J. Chem.*, 1972, **25**, 2577–2581.

Blind spheres of paramagnetic dopants in solid state NMR

Wenyu Li[a], Qianyun Zhang[a], Jonas J. Joos[b], Philippe F. Smet[b], Jörn Schmedt auf der Günne[*,[a]]

[a] Inorganic Materials Chemistry, University of Siegen, Adolf-Reichwein-Str. 2, 57076 Siegen, Germany

[b] LumiLab, Department of Solid State Sciences, Ghent University, Krijgslaan 281-S1, 9000 Gent, Belgium.

[*]gunnej@chemie.uni-siegen.de

Supporting information

1. Line width and isotropic chemical shift changes of $La_{1-x}Sm_xPO_4$ series

In order to test whether the Sm^{3+} NMR data would show correlations to the doping level x, both the isotropic chemical shift values (δ_{iso}) and the line width (Δv) for three different environments have been plotted against x (Fig. S1). The three components are: (1) the comparably sharp signal at the $LaPO_4$ signal position of around -4.6 ppm, (2) the comparably broad signal whose $\delta_{iso} > 0$ ppm and shifts towards the $SmPO_4$ signal position as x increases, (3) the signal in between the previous two signals. When $x > 0.1$, peaks can't be well separated due to the overlap of different components. Nevertheless, positive correlations could be rationalized between δ_{iso}, Δv and x, although the overlap would introduce large data scattering for deconvolution. In order to present the correlation as well as indicate the large data scattering, data points with same x were plotted, which were obtained by deconvolution from different starting values on the same spectrum.
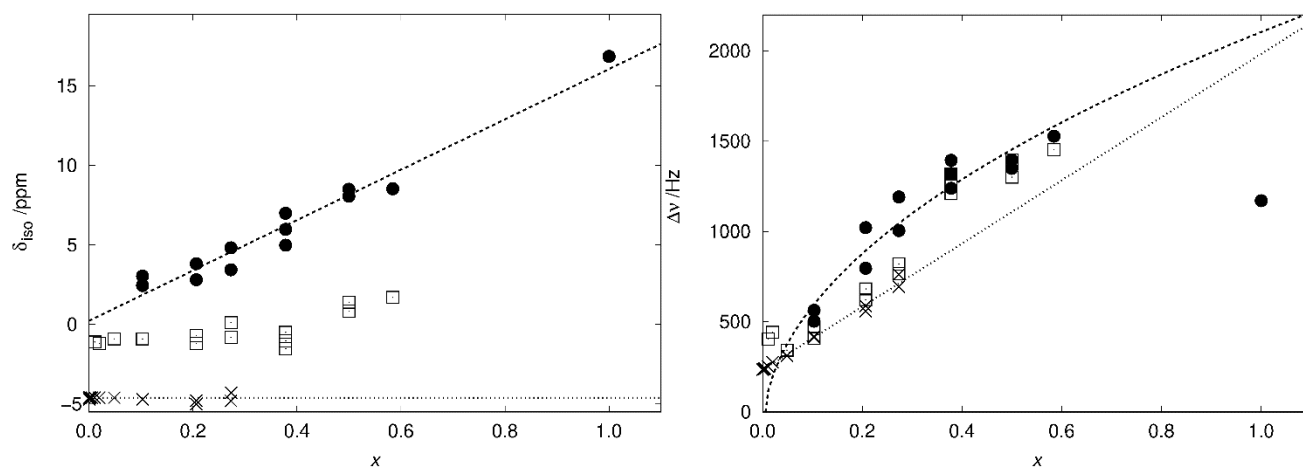
Figure S1: (left) isotropic chemical shift values as a function of the substitution degree x in 1000 °C co-precipitated $La_{1-x}Sm_xPO_4$, the dashed line represents linear fits resulting in δ_{iso}/ppm = 0.2 + 15.8·x, and the dotted lines represent δ_{iso}/ppm = −4.6. (right) line width as a function of the substitution degree x in co-precipitated $La_{1-x}Sm_xPO_4$, the dashed line represent Δv/Hz = −115 + 2220·$x^{1/2}$, and the dotted line represents Δv/Hz = 234 + 1749·x. The data points of the same x show significant scattering of the fitted parameters for overlapping signals.

A linear relation only holds for the peak component (Fig. S1 crosses) at around −4.6 ppm, which is close to the ^{31}P shift for non-doped diamagnetic $LaPO_4$. For the broad component (Fig. S1 circles) which stretches further towards $SmPO_4$ signal as x increases, a linear relation, which was suggested earlier in literature[1,2], is not describing the experimental data well. A square root function provides a more reasonable fit. As for the middle component (Fig. S1 squares), which lies in between two previously peaks, the functional dependence is more difficult to identify and needs more components.

2. Exchange 2D spectra for $La_{1-x}Ln_xPO_4$ (Ln = Nd, Dy, Ho, Er, Tm, Yb)

2D exchange spectroscopy (EXSY) ^{31}P MAS experiments with zero mixing time show a sharp ridge on the diagonal (Fig. S2) for $La_{1-x}Ln_xPO_4$ (Ln = Nd, Dy, Ho, Er, Tm, Yb) samples, which is typical for inhomogeneous broadening.

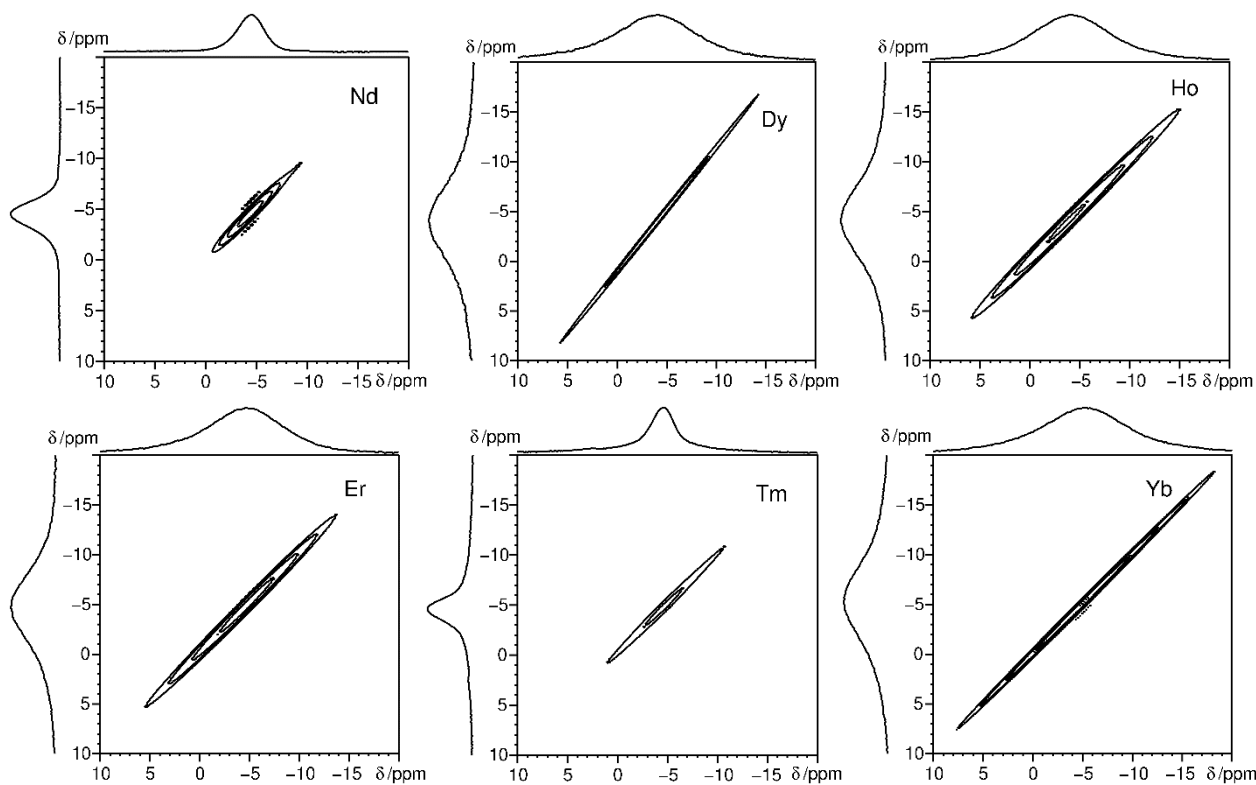Figure S2: 2D ^{31}P MAS EXSY spectra (with zero mixing time) for La$_{0.98}$Nd$_{0.02}$PO$_4$, La$_{0.995}$Dy$_{0.005}$PO$_4$, La$_{0.99}$Ho$_{0.01}$PO$_4$, La$_{0.99}$Er$_{0.01}$PO$_4$, La$_{0.995}$Tm$_{0.005}$PO$_4$ and La$_{0.98}$Yb$_{0.02}$PO$_4$, which all show a lineshape consistent with inhomogeneous line broadening. MAS spinning frequency is 10 kHz for La$_{1-x}$Ln$_x$PO$_4$ Ln = Nd, Dy, Tm and 12.5 kHz for Ln = Ho, Er, Yb.

3. Different correlations blind sphere radius with Ln-parameters

The factor $C_{SA} = g_J^2 J(J+1)^4$ refers to the lanthanide free-ion and gives indication on the size of the anisotropy shielding contribution to hyperfine shift. The parameter C_{con} refers to the size of electronic contribution from contact shielding[4]. The blind sphere sizes r_0 of measured lanthanide ions were plotted against both $\sqrt[3]{|C_{SA}|}$ (Fig. S3) and $\sqrt[3]{|C_{con}|}$ (Fig. S4). A linear dependence $r_0 \propto \sqrt[3]{|C_{SA}|}$ was observed (Fig. S3) except for Gd^{3+}. Such correlation indicates that, for the same host, treating the dopant ions as free lanthanide ions provides a reasonable estimate of the trend of the size of the blind sphere. Also contact and pseudo-contact contributions were considered. An empirical linear dependence $r_0 \propto \sqrt[3]{|C_{con}|}$ was observed (Fig. S4) for all Ln^{3+} including Gd^{3+}.

Figure S3: Blind sphere radii for Ln(III) dopants of $La_{1-x}Ln_xPO_4$ series, plotted against $\sqrt[3]{|C_{SA}|}$. $|C_{SA}|$ refers to the magnitude of hyperfine contribution from anisotropy shielding[4]. The dashed line features the fitting function $r_0/Å = -1.50 + 2.83 \cdot \sqrt[3]{|C_{SA}|}$ with $R^2 = 0.85$.
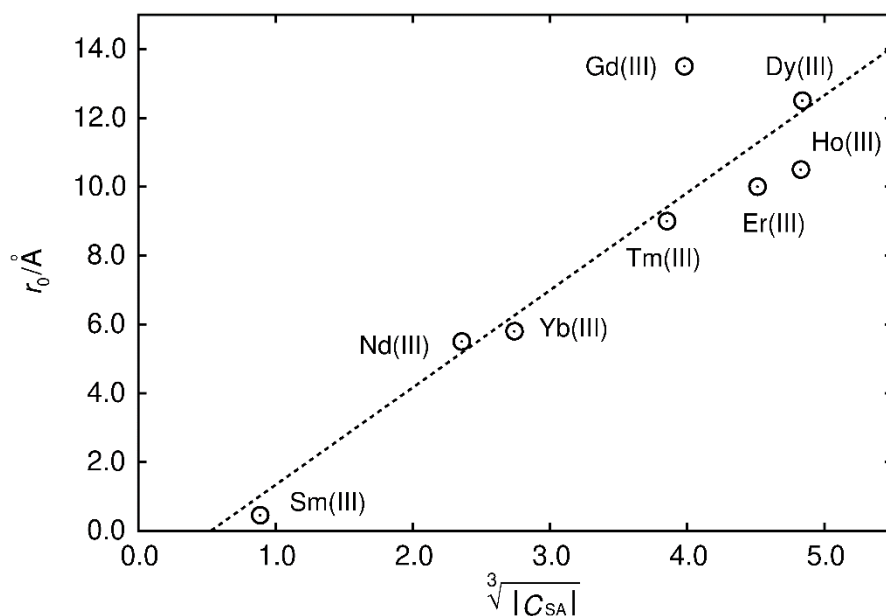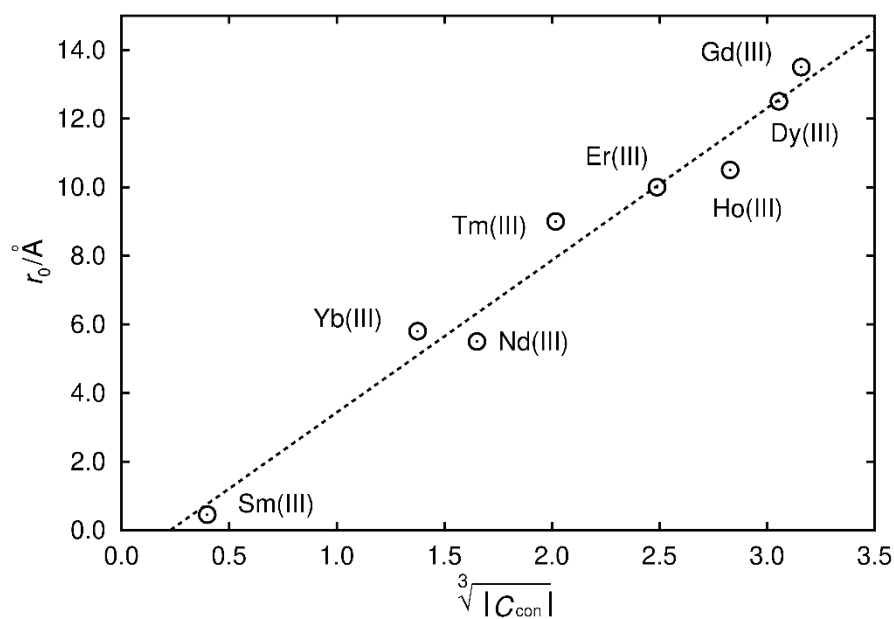

Figure S4: Blind sphere radii for Ln(III) dopants of $La_{1-x}Ln_xPO_4$ series, plotted against $\sqrt[3]{|C_{con}|}$. $|C_{con}|$ refers to the magnitude of electronic contribution from contact shielding[4]. The dashed line features the fitting function $r_0/Å = -1.01 + 4.44 \cdot \sqrt[3]{|C_{con}|}$ with the coefficient of determination $R^2 = 0.97$.

-4-

4. ^{31}P NMR relaxation
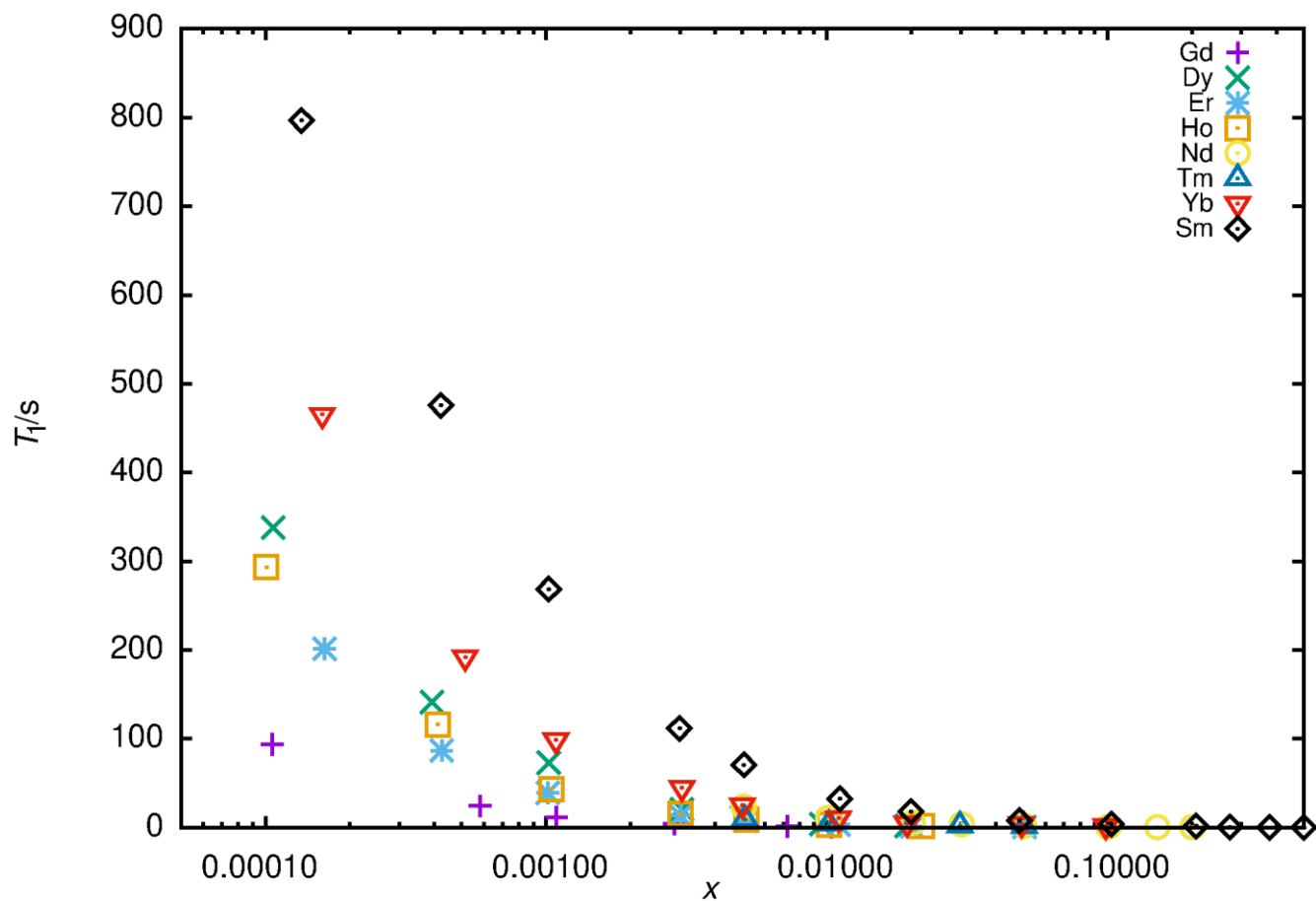
Figure S5: T_1 relaxation data of LaPO$_4$:Ln obtained with the saturation recovery sequence at room temperature in a magnetic field of 9.4 T.

References

1 T. Harazono, E. Yokota, H. Uchida and T. Watanabe, *Bull. Chem. Soc. Jpn.*, 1998, **71**, 2797–2805.

2 T. Harazono, E. Yokota, H. Uchida and T. Watanabe, *Bull. Chem. Soc. Jpn.*, 1998, **71**, 825–829.

3 K. Schmidt-Rohr and H. W. Spiess, *Multidimensional Solid-State NMR and Polymers*, Elsevier, 2012.

4 A. J. Pell, G. Pintacuda and C. P. Grey, *Prog. Nucl. Magn. Reson. Spectrosc.* 2019, **111**, 1-271.

5 I. Bertini, C. Luchinat, G. Parigi and E. Ravera, *NMR of Paramagnetic Molecules: Applications to Metallobiomolecules and Models*, Elsevier, 2016.

6 Y. Ni, J. M. Hughes and A. N. Mariano, *Am. Mineral.*, 1995, **80**, 21–26.

7 C. H. Evans, *Biochemistry of the Lanthanides*, Springer Science & Business Media, 2013.

3.3 A Guide to Brighter Phosphors — Linking Luminescence Properties to Doping Homogeneity Probed by NMR

Wenyu Li, Matthias Adlung, Qianyun Zhang, Claudia Wickleder, and Jörn Schmedt auf der Günne

Contribution to the manuscript:

Based on discussions and conceptual guidance from Jörn Schmedt auf der Günne, the NMR study and all NMR related data analysis were done by me. The initial testing of $La_{1-x}Ln_xPO_4$ synthesis methods was done by me. The optimization and the routine synthesis of $La_{1-x}Ln_xPO_4$ were assisted by Qianyun Zhang. The Rietveld refinement was done by me. The quantitative excitation plus emission spectra and the decay times were measured by Matthias Adlung in the group of Claudia Wickleder. The data interpretation of lifetime was done by me with the help of Jörn Schmedt auf der Günne. The computer program which did synchronous least-square fitting of decay time curves was written by Jörn Schmedt auf der Günne. This paper was drafted by me and perfected by Jörn Schmedt auf der Günne.

A Guide to Brighter Phosphors-Linking Luminescence Properties to Doping Homogeneity Probed by NMR

Wenyu Li,[a] Matthias Adlung,[b] Qianyun Zhang,[a] Claudia Wickleder,[b] and
Jörn Schmedt auf der Günne*[a]

Crystalline powders of Ln^{3+} doped $LaPO_4$ (Ln=Nd, Gd, Dy, Ho, Er, Tm, Yb) have been synthesized to serve in a case study for linking doping homogeneity as determined by NMR to luminescent properties. Samples obtained via different synthesis methods act as examples of homo- and inhomogeneous doping. The sample quality was verified by X-ray diffraction. The homogeneously doped samples show improved luminescent properties in terms of brightness and lifetime which is consistent with the interpretation that, NMR visibility curves probe the distribution of paramagnetic dopants on a similar length scale as necessary for an efficient energy transfer in crystalline phosphors i.e. between sensitizers and activators, and to killer sites. Thus "NMR homogeneity" as observed by visibility curves may serve as a tool to optimize luminescent materials.

1. Introduction

Paramagnetic dopants, especially the paramagnetic lanthanide ions, play an important role in various applications, for example $Y_3Al_5O_{12}:Ce^{3+}$ is used as scintillator material,[1] $Y_2O_3:Eu^{3+}$ in cathode ray tubes,[2] $Gd_2O_2S:Tb^{3+}$ as X-ray phosphor,[3] $SrAl_2O_4:Eu^{2+},Dy^{3+}$ as long persistent phosphor[4] and $Y_3Al_5O_{12}:Nd^{3+}$ in solid-state lasers.[5] In case of the application scenario of light-converting phosphors, brightness, efficiency and lifetime are related to the local pair distance[6] and the effective dopant concentration,[7] which are both microscopically related to the dopant distribution. Especially for brightness, i.e. quantum yields, phosphors may suffer from concentration quenching[6,8] at high doping level which inhibits higher emission intensities. A homogeneous distribution of dopants ensures a high effective doping concentration while it avoids concentration quenching[6] at low doping concentration and therefore improves quantum yields (Figure 1 and 2).

Distribution of dopants can be investigated by different techniques, for example by X-ray diffraction (XRD),[9,10] X-ray photoelectron spectroscopy (XPS)[10] or energy dispersive X-ray spectroscopy (EDX).[11] In general, the concept "homogeneity" as defined by IUPAC[12] is related to a defined quantity of a material, i.e. volume or length scale: optical glasses depict long-
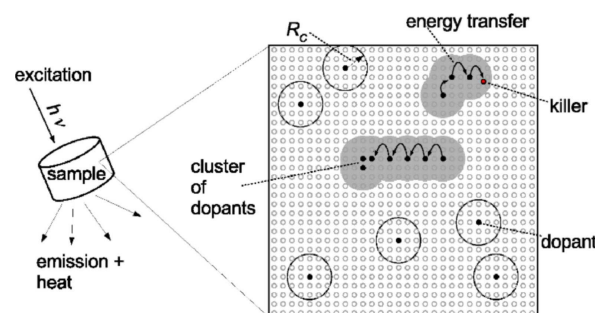

Figure 1. A schematic sketch describing how the dopant distribution affects the luminescence behavior. The crystalline host is shown by its potential doping sites (small empty circles) and the sites filled with dopants (filled black circles). Dopants can be activators (A) and/or sensitizers (S) depending on the system. Energy transfer may happen between either of them, i.e. S to A (SA) or S to S (SS) if they are closer than the critical distance[16] R_C (big circles around a dopant), which differs for different dopants and different transfer processes. For mono-doped systems, concentration quenching[6] of an emission band may be ascribed to energy migration of the excited state to a cluster site leading to cross-relaxation or to a killer site (red circle) leading to non-radiative conversion to the ground state.

range homogeneity when investigated by optical microscopic techniques (visible light), but may show inhomogeneity (heterogeneity) on an atomic scale (electron microscopy).[13] Here the term "homogeneous doping" is used to refer to a random, i.e. statistical, substitutional doping of a crystalline host material (Figure 2). Depending on the analytical technique and required length scale, a sample could thus appear to be homogeneous and inhomogeneous at the same time. Besides, some techniques like XPS and EDX are more surface sensitive or have a smaller analyzed volume,[14] while others sense bulk properties[15] as for example laboratory powder XRD. Different analytical techniques often nicely complement one another with respect to length scale and surface sensitivity. However, analysis of homogeneity on an atomic scale of dopants added in the low-percent range turns out to be a non-trivial problem.

[a] W. Li, Q. Zhang, Prof. Dr. J. Schmedt auf der Günne
Department of Chemistry and Biology Chemistry
University of Siegen
Adolf-Reichwein-Str. 2, 57076 Siegen, Germany
E-mail: gunnej@chemie.uni-siegen.de
[b] Dr. M. Adlung, Prof. Dr. C. Wickleder
Department of Chemistry and Biology Chemistry
University of Siegen
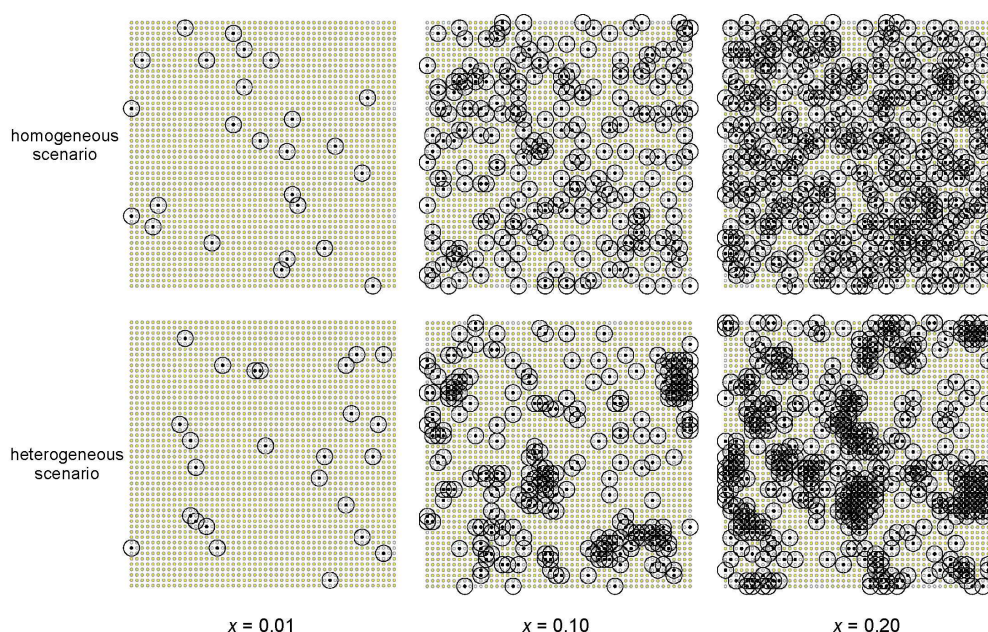Adolf-Reichwein-Str. 2, 57076 Siegen, Germany

Figure 2. A simplified two-dimensional illustration of a homogeneous (top row) and a heterogeneous (bottom row) doping scenario in a crystalline host where a certain fraction x of dopable sites (small circles) is filled with paramagnetic dopants (black filled circles). In terms of NMR visibility only signals from the volume outside the blind spheres[26] (big circles with r_0) can be picked up. In terms of luminescence the radii of these spheres (big circles) could be interpreted as the critical energy transfer distance[16] R_c. The radii r_0 and R_c are not the same but typical values fall into a similar range: Å – few nm.[17–20,26,35,36]

The role of energy transfer processes,[6,16–18] which may happen between sensitizers or between sensitizer and activator, and from sensitizer to killer sites, can't be underestimated (Figure 1) for a better understanding of how the dopant distribution relates to luminescence performance. The processes operate over a distance called critical energy transfer distance R_c which ranges from a few ångströms to a few nanometers.[17–20]

Solid state NMR has been reported to be helpful for studying paramagnetic systems.[21–26] Especially, the distribution of paramagnetic dopants can be investigated by the spin-lattice relaxation time,[27–30] hyperfine shifts[31,32] and the line-broadening effect.[27,33,34] Homogeneous distributions of Tb^{3+} and Eu^{3+} were shown to be correlated to NMR line broadening and positively related to the brightness of phosphors.[33,34]

A disadvantage of a lineshape analysis is that it implicitly only refers to the NMR visible part of the compound but not to the nuclei inside the blind sphere, i.e. in direct vicinity of paramagnetic centers, for which the signal may vanish within the dead-time of spectrometer. An alternative to the lineshape analysis approach is the visibility function, i.e. the observed peak area as a function of doping concentration which was also shown to be related to doping homogeneity (Figure 3).[35] It is interesting to note that for lanthanide ions the blind sphere radii[26,35,36] and the critical energy transfer distances[17–20] share a similar size range. The aim of this contribution is to relate NMR doping homogeneity to the luminescence properties of inorganic phosphors on the basis of the NMR visibility function[35] for the first time. For this case study $LaPO_4$ was chosen as a diamagnetic inorganic host and different Ln^{3+} ions (Ln=Nd, Gd, Dy, Ho, Er, Tm, Yb) served as paramagnetic dopants which allows to determine blind sphere
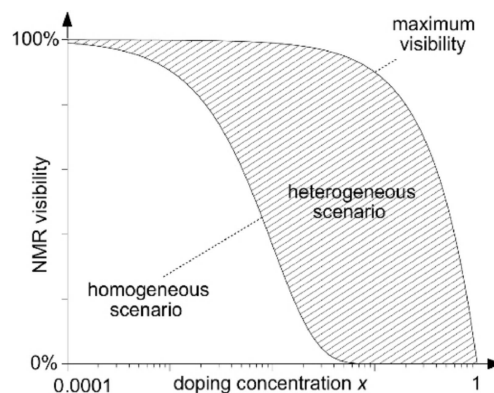
Figure 3. Typical NMR visibility curves $f(x)$ as a function of the paramagnetic dopant concentration x. The NMR visibility is defined as the visible signal of the doped material normalized by the signal of the diamagnetic host.[35] For a homogeneous doping scenario, the NMR signals vanish in the dead-time of the spectrometer[36] more efficiently thus $f(x)$ approaches zero earlier as x increases. The visibility of the heterogeneous case $f(x)$ is located in the dashed regime between the maximum visibility $f_{max}(x)$ (upper solid line) and the visibility of a homogeneous doping scenario. The NMR visibility is always smaller for a homogeneous (lower solid line) than for a heterogeneous doping scenario (compare Figure 2) at the same doping concentration.

radii by ^{31}P NMR and sample quality by XRD at the same time. Besides $LaPO_4$:Ln(III) is a reasonable phosphor[37–39] so that luminescence properties (lifetime and brightness) could be determined. If the working hypothesis is true, that the NMR length scale given by the blind sphere radius is similar to the distance relevant to energy transfer in lanthanide doped phosphors, then it should be possible to observe differences in luminescence proper-

ties between homogeneously and inhomogeneously doped samples.

2. Results and Discussion

2.1. XRD Homogeneity

In a first step two sample series were obtained by different synthesis routes. Their doping homogeneity was evaluated by XRD, i.e. by Rietveld refinement and Vegard's law.[40] The corresponding refinement results (Supporting information Figure S1–S4) of the $La_{1-x}Ln_xPO_4$ series (Ln≡Nd, Dy, Ho, Yb), which were obtained by **co-precipitation**, show a linear correlation of the lattice parameters with the doping concentration x. Such fulfillment of Vegard's law is often obeyed by **homogeneously** doped samples which follow random substitutional replacement of ions.[41]

For the samples obtained via a **solid-state reaction** a phase separation of $LnPO_4$ and $LaPO_4$ becomes evident at high doping concentration ($x \geq 0.2$) from the powder diffractograms (Supporting Information Figure S5). Phase separation is a typical case of **heterogeneity**. Note that XRD requires the samples to be doped to a high degree (herein about $x \geq 0.05$) to obtain lattice parameter changes which are significant, while doping levels relevant to luminescence properties often require low lanthanide doping concentrations, for instance $x < 5\%$.

2.2. NMR Homogeneity

In a second stage these sample were investigated by quantitative ^{31}P NMR to test whether the NMR homogeneity agrees with XRD results at low doping concentration. Only one ^{31}P NMR signal at around -4.6 ppm, which corresponds to monazite $LaPO_4$, was observed for the $La_{1-x}Ln_xPO_4$ (Ln≡Nd, Gd, Dy, Ho, Er, Tm, Yb). As the doping level x increases, the signal broadens without significant shifts and the peak area decreases (^{31}P MAS NMR spectra stack plots in Supporting Information Figure S6–S11). Thus the situation in the investigated cases is simpler than in the cases of $La_{1-x}Sm_xPO_4$[36] and $La_{1-x}Eu_xPO_4$,[32] where different ^{31}P signals could be observed.

The resulting peak areas from one pulse experiments were calculated and tested by the visibility function.[35,36] Deviations from the theoretical visibility function for homogeneous doping indicate a lower degree of NMR homogeneity. By this comparison for seven Ln^{3+} dopants (Figure 4 for Dy^{3+} and for other Ln^{3+} ions (Supporting Information Figure S6–S11)) it is possible to conclude that the samples series obtained via a solid-state-reaction showed a lower degree of NMR homogeneity as compared to the co-precipitated samples of the same dopant series. Therefore, differences in homogeneity can be traced via the NMR visibility function in the low-doping regime. The result is in excellent agreement with the XRD analysis.

The homogeneity length scale of the NMR experiment is related to the radius of the blind sphere of the paramagnetic dopant. For Nd, Gd, Dy, Er, Ho, Tm, Yb in $La_{1-x}Ln_xPO_4$ the blind
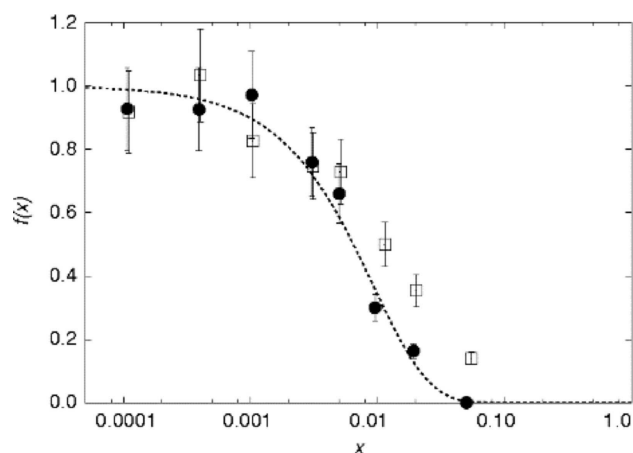

Figure 4. The normalized NMR visibility $f(x)$ as a function of doping concentration x, for $La_{1-x}Dy_xPO_4$ obtained by the co-precipitation method (circles) and by the solid-state reaction method (squares). The dashed lines feature a fitted visibility function[27] $f(x) = \exp(-ar_0^3 x)$ with $a = 0.055/Å^3$ and $r_0 = 12.5$ Å.

sphere radii are 5.5 Å, 13.5 Å, 12.5 Å, 10.5 Å, 10 Å, 9 Å and 5.8 Å respectively.[36] Based on the differences in homogeneity traced via the NMR visibility curves (Figure 4 and Figure S6–S11), it may be concluded that only the co-precipitated samples qualify as homogeneously doped on a length scale of about 1 nm.

2.3. Luminescence Spectra

What remains to be shown is that homogeneity on the nm-scale correlates with luminescence properties. From the different available doping series only Dy^{3+} doped $LaPO_4$ was chosen for luminescence measurements. Quantitative excitation and emission spectra for the Dy^{3+} doped samples with $x = 0.05$ (Figure 4) show their most intense emissions bands at 477 and 572 nm which can be assigned to transitions[42,43] $^4F_{9/2} \rightarrow {}^6H_{15/2}$ and $^4F_{9/2} \rightarrow {}^6H_{13/2}$, respectively.

An increase in brightness can be observed (Figure 5) for the $La_{0.95}Dy_{0.05}PO_4$ samples which feature a more homogeneous dopant distribution according to the NMR and XRD analysis.

2.4. Luminescence Lifetimes

To obtain independent evidence of doping homogeneity lifetime measurements of the two sample series of $La_{1-x}Dy_xPO_4$ were obtained (lifetime curves: Supporting Information Figure S12–S18). Qualitatively the individual measurements show a transition from mono-exponentially decaying lifetime functions to a complex behavior with increasing doping concentration x.

How can this behavior qualitatively be understood and what can be learned about the distribution of dopants from lifetime measurements?

The lifetime functions applying to isolated ions are well established, describe the intensity decay as a mono-exponential
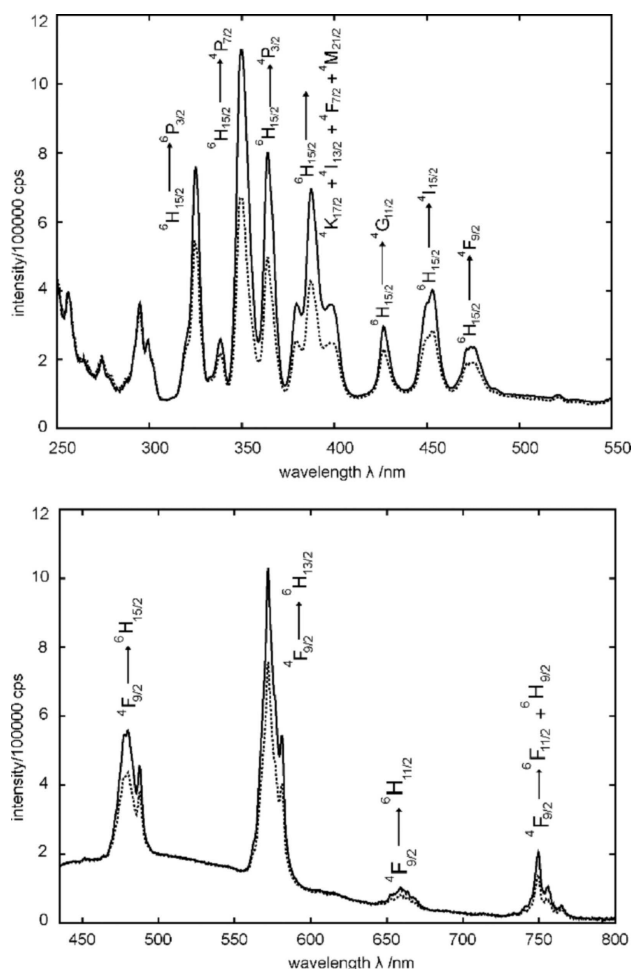
Figure 5. Excitation (top) and emission (bottom) spectra of $La_{0.95}Dy_{0.05}PO_4$ obtained by co-precipitation (solid line) and solid-state reaction (dashed line). The excitation spectra were recorded at an emission wavelength of $\lambda_{em} = 572$ nm. The emission spectra were measured at an excitation wavelength of $\lambda_{ex} = 325$ nm.

function and require excitation and emission to occur on the same ion S.[16,18]

$$I(t) = I_0 \exp\left(-\frac{t}{\tau_0}\right)$$

The same model also applies when the energy is transferred from one S atom to another one (SS transfer) between excitation and emission.

When a photon is excited on an S atom (sensitizer) transferred to an activator (A) or a killer site (SA transfer),[18] deviations from mono-exponential functions are expected.[16,18]

$$I(t) = I_0 \exp\left(-\frac{t}{\tau_0} - C\, t^{\frac{3}{n}}\right)$$

C is a constant that relates to both concentration of A, and the interaction strength between S and A, while n depends on the electric multipole interaction ($n = 6$, 8 or 10 for dipole-

dipole, dipole-quadrupole or quadrupole-quadrupole interaction, respectively).[44] If SA and SS transfers are combined complicated non-monoexponential models apply.[18] Note that in a doping series with variable doping concentration x the lifetime of the activators will reflect their individual environments, i.e. clustered activators which are subject to cross-relaxation and isolated activators will exist side by side and their lifetime curves can best be described as a sum of monoexponential curves with different lifetime values. Lifetime reduction by cross-relaxation processes[16,18,42] between Dy^{3+} ion pairs, for example ($^4F_{9/2}$, $^6H_{15/2}$)→($^6H_{5/2}$, $^6F_{7/2}$) and ($^4F_{9/2}$, $^6H_{9/2}$ ($^6F_{11/2}$))→($^6H_{15/2}$, $^6F_{3/2}$) is well estabilshed.[42,43]

As shown in detail in the supporting information (Figure S12–S18) the lifetime curves of both the homogeneous and the heterogeneous scenario can be described using the same lifetimes τ_1, τ_2 and τ_3 in the a tri-exponential model (see Supporting Information for details).

$$I(x) = I_0 \cdot \left(a_1 \cdot e^{-\frac{x}{\tau_1}} + a_2 \cdot e^{-\frac{x}{\tau_2}} + a_3 \cdot e^{-\frac{x}{\tau_3}}\right) + I_{\text{offset}}$$

$$1 = a_1 + a_2 + a_3$$

$$\tau_1 > \tau_2 > \tau_3$$

The corresponding parameters could be extracted via synchronous least-square fitting of all lifetime curves. This approach minimizes the number of fitting parameters and delivers a stable fitting model. The longest lifetime τ_1 clearly can be assigned to the lifetime of isolated Dy ions, while the other two can be considered as fitting parameters to reflect different processes leading to shorter lifetimes or more complex decay functions in general. The parameters a_1, a_2 and a_3 depend on the doping concentration and are the weights of the individual exponential curves, while I_0 and I_{offset} depend on the individual measurements, i.e. the amount of experimental time spent on each experiment and background noise, respectively.

Lifetime measurements can be described both for the heterogeneous and homogeneous sample series in the low-doping regime with the same lifetimes. Thus it is reasonable to argue that killer sites caused by different lattice defects, e.g. color centers, which should be synthesis dependent, have a negligible influence on the lifetime curves in this case. Impurities by other rare earth elements were neglected because of the used reagent purities. Thus the shortening of the lifetimes will be discussed based on the assumption that cross-relaxation caused by cluster formation of Dy-ions is the main mechanism for lifetime reduction.

How should the dopant distribution influence the weights a_n as a function of doping concentration x? The weight a_1 is a measure for the frequency of isolated dopants and is well defined because it describes the degree of mono-exponentiality of the lifetime curves. The relative amount of isolated dopants ($\sim a_1$) decreases as the doping concentration x increases in both the homogeneous and the heterogeneous doping model (Figure 6).

The visualization (Figure 2) may help grasping the differences between the homogeneous and the heterogeneous doping
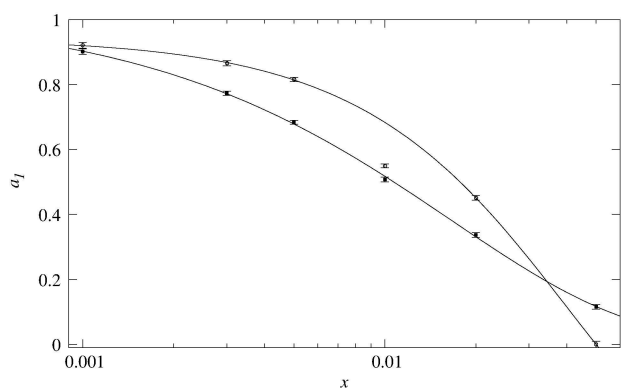
Figure 6. Weight a_1 with error bars of the slowest decay process in a lifetime measurement obtained by a synchronous tri-exponential fit of all lifetime curves at different doping concentrations x, for two $La_{1-x}Dy_xPO_4$ doping series: samples obtained by co-precipitation (open circles), as an example for homogeneous doping and samples obtained via a solid-state reaction (filled squares), as an example for heterogeneous doping according to NMR and XRD. The lines serve as a guide to the eye (homogeneous case (solid line) $a_1(x) = 1.294 \cdot \exp(-(25.5 \cdot x)^{1.095}) - 0.352$, heterogeneous case $a_1(x) = 1.018 \cdot \exp(-(60.4 \cdot x)^{0.729} + 0.008$. The fairly small statistical errors obtained via an error analysis indicate that the fit is stable and sample-preparation dependent errors dominate.

scenario. In the low-doping regime both the homogeneous and the heterogeneous case look similar (Figure 2), which reflects the stabilization of defects for entropic reasons and the formation of a thermodynamically stable solid solution of $La_{1-x}Dy_xPO_4$. Higher doping concentrations may cause demixing as the XRD measurements showed (Supporting Information Figure S5). The precise distribution of the dopants in the host depends on the preparation and the type of segregation process, for example spinodal demixing versus crystallization and growth, and Oswald ripening. The formation of clusters may be considered as a consequence of demixing and phase segregation. Note, that in the homogeneous doping scenario clusters will form simply for statistical reasons, especially in the high doping regime. In the low doping regime the frequency of isolated dopants, corresponding to the non-overlapping spheres (Figure 2) with a radius of the critical energy transfer distance R_c, would be higher in the homogeneous than in the heterogeneous case. However in the high doping regime the frequency of isolated dopants are expected to be higher in the heterogeneous than in the homogeneous scenario, because demixing generates islands of low-doping between clusters of dopants in the heterogeneous case (Figure 2).

Following this argument the frequency of isolated dopants, i.e. weight a_1, is then expected to start off with similar values for the homogeneous and heterogeneous doping scenario at low doping concentration (Figure 6). With increasing doping concentration, clusters would form which indirectly reduce the frequency of isolated dopants. Because clusters form more easily in the heterogeneous doping scenario its frequency of isolated dopants would be reduced faster. However the opposite behavior is expected for the even higher doping concentrations: while in the homogeneous case for statistical reasons almost all dopants would be part of a cluster (Figure 2),

in the heterogeneous case a limited frequency of dopants could still remain in the space between the clusters. Consequently the frequency of isolated dopants as a function of doping concentration should feature a cross-over for the homogeneous and the heterogeneous scenario. As can be seen in Figure 6, the expected behavior is observed which is an independent confirmation of the hypothesis that NMR homogeneity can be related to the luminescence properties, because blind sphere radii and critical distances in luminescence are of the same order of magnitude.

3. Conclusions

The main target of this contribution was to test whether homogeneity evaluated by the peak areas in solid state NMR shows consistency with the actual luminescence performance. To this end seven different sample series of lanthanide doped monazite $LaPO_4$ were prepared. Sample homogeneity could be tested by XRD in this case because the doping concentration could be varied from x equals 0 to 100 %. NMR was able to provide the same information on the basis of the NMR visibility function, with the advantage that the visibility function does not require the samples to be doped up to 100 % but to much lower values. The established homogeneity of the samples was shown to be related to both fluorescence intensity and the lifetime of the excited states. The length scale of the NMR homogeneity criterion can be estimated as the blind-sphere radius which takes values up to 1 nm approximately for Ln(III) dopants. The method is not restricted by the choice of the host structure as long as NMR nuclei are present. An application of this method to for example Ln(II) or Ln(III) doped halogenides, phosphates, borates or nitrides should be straight forward. Synthesis methods that produce samples with higher NMR homogeneity avoid the unnecessary consumption of dopant reagents. The activator ions can be used more efficiently and a higher light yield should be achievable. We conclude solid state NMR may act as a tool for the evaluation of different synthesis methods and for optimizing luminescence properties.

Experimental Section

Two commonly used synthesis routines have been selected in order to create different degrees of doping homogeneity.

The co-precipitation method: Ln_2O_3 (Ln=Nd, Gd, Dy, Er, Ho, Tm, Yb. Nd_2O_3 was bought from ChemPur, the rest from smart elements®. The purity is 99.999 % for Dy_2O_3 and 99.99 % for the rest) and La_2O_3 (Chempur, 99.99 %) were dissolved in concentrated nitric acid and later on mixed with excess $NH_4H_2PO_4$ (VWR chemicals) solution. The resulting precipitates were centrifuged and washed with water and ethanol. The washed precipitates were dried at 80 °C overnight and sintered in corundum crucibles at 1000 °C for 4 h.

The "solid-state reaction" method: stoichiometric amounts of Ln_2O_3, La_2O_3 and $NH_4H_2PO_4$ were ground in an agate mortar and sintered in corundum crucibles at 1000 °C for 4 h.

Powder XRD measurements were performed on a Huber G621 diffractometer with Cu $K_{\alpha 1}$ radiation ($\lambda = 0.15405931$ nm) and

Guinier camera in transmission geometry. Diffractograms were extracted from the image files, which were obtained by scanning photostimulable $BaBrF:Eu^{2+}$ films with an image plate detector (Typhoon FLA 7000, $\lambda = 650$ nm), by a home-written program ("ipreader", version 0.9).

The solid state NMR measurements were performed on a Bruker Avance II spectrometer at 7.05 T. Magic angle spinning (MAS) was done with 4 mm pencil rotors at 10 kHz spinning frequency with completely filled rotors with a home-built McKay probe head. The spectra were acquired by direct excitation, with a dead time of 15 μs, and 90° pulses with a pulse length of typically 4–5 μs and repetition delays being longer than 5 times the T_1 relaxation time to ensure quantitative measurements. In addition, quantification was assisted by a micro-balance (Sartorius MC5). The deconvolution of peaks was performed by the program deconv2Dxy[45] (version 0.4). Because an external referencing method was used for quantification we estimated that this scheme causes a relative error of the individual measurements of about 10% being related to small changes in tuning, matching and in dielectric loss. The NMR visibility was calculated as observed peak area per mole of doped sample normalized by that of the non-doped sample. The NMR visibility fitting function[35] for homogeneously doped sample was shown to be $f(x) = exp(-ar_0^3 x)$, with $a = 4\pi N_{hostUC}/3V_{UC} = 0.055/Å^3$ for monazite[46] $LaPO_4$, where N_{hostUC} is the number of "dopable" sites in the unit cell and V_{UC} is the volume of the unit cell. Herein $N_{hostUC} = 4$ and $V_{UC} = 305.73$ Å^3. The variable r_0 is the blind sphere radius of a paramagnetic ion.

Quantitative excitation and emission spectra were recorded on a FluoroMax HORIBA fluorescence spectrometer within a spectral range of 250–800 nm with an integrating sphere. The emission spectra were corrected for the sensitivity of the photomultiplier and the reflectivity of the integrating sphere. Decay times were measured at room temperature using a 75 W Xe flash attached to a Fluorolog 3 spectrometer (FL3-22, Horiba). At both spectrometers the emission was detected by a photomultiplier R928P from Hamamatsu.

Conflict of Interest

The authors declare no conflict of interest.

[1] M. Moszyński, T. Ludziejewski, D. Wolski, W. Klamra, L. O. Norlin, *Nucl. Instrum. Methods Phys. Res. Sect. A* **1994**, *345*, 461–467.
[2] S. L. Jones, D. Kumar, R. K. Singh, P. H. Holloway, *Appl. Phys. Lett.* **1997**, *71*, 404–406.
[3] L. H. Brixner, *Mater. Chem. Phys.* **1987**, *16*, 253–281.
[4] T. Matsuzawa, Y. Aoki, N. Takeuchi, Y. Murayama, *J. Electrochem. Soc.* **1996**, *143*, 2670–2673.
[5] A. Ikesue, Y. L. Aung, T. Taira, T. Kamimura, K. Yoshida, G. L. Messing, *Annu. Rev. Mater. Res.* **2006**, *36*, 397–429.
[6] W. M. Yen, S. Shionoya, H. Yamamoto, *Phosphor Handbook*, CRC Press/Taylor and Francis, Boca Raton, **2007**.
[7] S. Wu, Z. Pan, R. Chen, X. Liu, *Long Afterglow Phosphorescent Materials*, Springer, **2017**.
[8] D. L. Dexter, J. H. Schulman, *J. Chem. Phys.* **1954**, *22*, 1063–1070.
[9] A. Punnoose, M. H. Engelhard, J. Hays, *Solid State Commun.* **2006**, *139*, 434–438.
[10] C. Dong, J. Pichaandi, T. Regier, F. C. J. M. van Veggel, *J. Phys. Chem. C* **2011**, *115*, 15950–15958.
[11] D. Flak, E. Coy, G. Nowaczyk, L. Yate, S. Jurga, *RSC Adv.* **2015**, *5*, 85139–85152.
[12] *IUPAC. Compendium of Chemical Terminology*, 2nd ed. (the "Gold Book"). Compiled by A. D. McNaught, A. Wilkinson. Blackwell Scientific Publications, Oxford, **1997**.
[13] L. R. Pinckney, G. H. Beall, *J. Am. Ceram. Soc.* **2008**, *91*, 773–779.
[14] H. Hantsche, *Scanning* **1989**, *11*, 257–280.
[15] K. Hirota, J. P. Hill, S. M. Shapiro, G. Shirane, Y. Fujii, *Phys. Rev. B* **1995**, *52*, 13195–13205.
[16] G. Blasse, B. C. Grabmaier, *Luminescent Materials*, Springer Berlin Heidelberg, **1994**.
[17] G. Blasse, *Phys. Lett. A* **1968**, *28*, 444–445.
[18] G. Blasse, *Mater. Chem. Phys.* **1987**, *16*, 201–236.
[19] K. Li, R. V. Deun, *Dalton Trans.* **2018**, *47*, 6995–7004.
[20] J. Yang, J. Dong, R. Wu, H. Wu, H. Song, S. Gan, L. Zou, *Dalton Trans.* **2018**, *47*, 9795–9803.
[21] A. J. Pell, G. Pintacuda, C. P. Grey, *Prog. Nucl. Magn. Reson. Spectrosc.* **2019**, *111*, 1–271.
[22] T. Polenova, R. Gupta, A. Goldbourt, *Anal. Chem.* **2015**, *87*, 5458–5469.
[23] M. Bertmer, *Solid State Nucl. Magn. Reson.* **2017**, *81*, 1–7.
[24] E. Ravera, A. Carlon, M. Fragai, G. Parigi, C. Luchinat, *Emerg. Top. Life Sci.* **2018**, *2*, 19–28.
[25] J. Malanho Silva, L. Cerofolini, S. Giuntini, V. Calderone, C. F. G. C. Geraldes, A. L. Macedo, G. Parigi, M. Fragai, E. Ravera, C. Luchinat, *J. Struct. Biol.* **2019**, *206*, 99–109.
[26] I. Bertini, C. Luchinat, G. Parigi, E. Ravera, *NMR of Paramagnetic Molecules: Applications to Metallobiomolecules and Models*, Elsevier, **2016**.
[27] T. Harazono, R. Adachi, N. Kijima, T. Watanabe, *Bull. Chem. Soc. Jpn.* **1999**, *72*, 2655–2664.
[28] S. Maron, G. Dantelle, T. Gacoin, F. Devreux, *Phys. Chem. Chem. Phys.* **2014**, *16*, 18788–18798.
[29] S. Maron, N. Ollier, T. Gacoin, G. Dantelle, *Phys. Chem. Chem. Phys.* **2017**, *19*, 12175–12184.
[30] D. J. Kubicki, D. Prochowicz, A. Pinon, G. Stevanato, A. Hofstetter, S. M. Zakeeruddin, M. Grätzel, L. Emsley, *J. Mater. Chem. A* **2019**, *7*, 2326–2333.
[31] A. Karmakar, M. S. Dodd, S. Agnihotri, E. Ravera, V. K. Michaelis, *Chem. Mater.* **2018**, *30*, 8280–8290.
[32] L. Martel, A. Rakhmatullin, J. J. Baldoví, M. Perfetti, K. Popa, M. Deschamps, T. Gouder, E. Colineau, A. Kovács, J.-C. Griveau, *Phys. Rev. B* **2019**, *100*, 054412.
[33] T. Harazono, E. Yokota, H. Uchida, T. Watanabe, *Bull. Chem. Soc. Jpn.* **1998**, *71*, 2797–2805.
[34] T. Harazono, E. Yokota, H. Uchida, T. Watanabe, *Bull. Chem. Soc. Jpn.* **1998**, *71*, 825–829.
[35] W. Li, V. R. Celinski, J. Weber, N. Kunkel, H. Kohlmann, J. Schmedt auf der Günne, *Phys. Chem. Chem. Phys.* **2016**, *18*, 9752–9757.
[36] W. Li, Q. Zhang, J. J. Joos, P. F. Smet, J. Schmedt auf der Günne, *Phys. Chem. Chem. Phys.* **2019**, *21*, 10185–10194.
[37] K. Riwotzki, H. Meyssamy, A. Kornowski, M. Haase, *J. Phys. Chem. B* **2000**, *104*, 2824–2828.
[38] K. Riwotzki, H. Meyssamy, H. Schnablegger, A. Kornowski, M. Haase, *Angew. Chem. Int. Ed.* **2001**, *40*, 573–576.
[39] G. A. Hebbink, J. W. Stouwdam, D. N. Reinhoudt, F. C. J. M. van Veggel, *Adv. Mater.* **2002**, *14*, 1147–1150.
[40] L. Vegard, *Z. Phys.* **1921**, *5*, 17–26.
[41] A. R. West, *Solid State Chemistry and Its Applications*, Wiley, **1987**.
[42] S. Chemingui, M. Ferhi, K. Horchani-Naifer, M. Férid, *J. Lumin.* **2015**, *166*, 82–87.
[43] R. Faoro, F. Moglia, M. Tonelli, E. Cavallis, *Phys. Procedia* **2009**, *2*, 345–347.
[44] M. Inokuti, F. Hirayama, *J. Chem. Phys.* **1965**, *43*, 1978–1989.
[45] D. Jardón-Álvarez, J. Schmedt auf der Günne, *Solid State Nucl. Magn. Reson.* **2018**, *94*, 26–30.
[46] Y. Ni, J. M. Hughes, A. N. Mariano, *Am. Mineral.* **1995**, *80*, 21–26.

ARTICLES

homogeneous doping
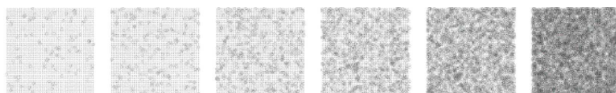
heterogeneous doping
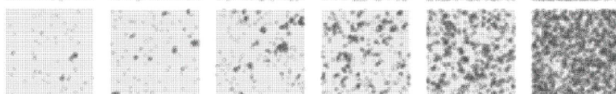
NMR allows distinguishing homogeneous from heterogeneous doping situations, which makes phosphors convert light more efficiently.

W. Li, Dr. M. Adlung, Q. Zhang, Prof. Dr. C. Wickleder, Prof. Dr. J. Schmedt auf der Günne*

1 – 7

A Guide to Brighter Phosphors-Linking Luminescence Properties to Doping Homogeneity Probed by NMR

CHEMPHYSCHEM

Supporting Information

A Guide to Brighter Phosphors-Linking Luminescence Properties to Doping Homogeneity Probed by NMR

Wenyu Li, Matthias Adlung, Qianyun Zhang, Claudia Wickleder, and
Jörn Schmedt auf der Günne*© 2019 The Authors. Published by Wiley-VCH Verlag GmbH &
Co. KGaA.

A guide to brighter phosphors - linking luminescence properties to doping homogeneity probed by NMR

Wenyu Li[a], Matthias Adlung[b], Qianyun Zhang[a], Claudia Wickleder[b], Jörn Schmedt auf der Günne*,[a]

[a,b] Inorganic Materials Chemistry, University of Siegen, Adolf-Reichwein-Str. 2, 57076 Siegen, Germany

*gunnej@chemie.uni-siegen.de

Supporting Information

1. Lattice parameters

Based on the Rietveld refinement results of the $La_{1-x}Nd_xPO_4$ series which were obtained by co-precipitation (Fig. **S1**), all the lattice parameters show linear correlation with doping level *x.*

Figure S1. Lattice parameters as a function of the substitution degree x in the co-precipitated and 1000 °C sintered $La_{1-x}Nd_xPO_4$, as determined by Rietveld refinement based on X-ray powder diffraction data. The dotted lines represent linear fits resulting in a/Å = *6.5114 – 0.0992*·x, b/Å = 7.0788 – 0.1189·x and c/Å = 8.2916 – 0.1570·x, respectively.

The Rietveld refinements have been performed also on the $La_{1-x}Dy_xPO_4$ (Fig. S2), $La_{1-x}Ho_xPO_4$ (Fig. S3), and $La_{1-x}Yb_xPO_4$ (Fig. S4) sample series, which were obtained by the co-precipitation method. The refinement results all show linear correlation with x. Note that the synthesized doping x ranges were different for different series, and at small doping level x, refinement data scattering is larger than at higher x.

Figure S2. Lattice parameters as a function of the substitution degree x in the co-precipitated and 1000 °C sintered $La_{1-x}Dy_xPO_4$, as determined by Rietveld refinement based on X-ray powder diffraction data. The dotted lines represent linear fits resulting in $a/Å = 6.5154 - 0.2094 \cdot x$, $b/Å = 7.0780 - 0.2890 \cdot x$ and $c/Å = 8.2938 - 0.3525 \cdot x$, respectively.
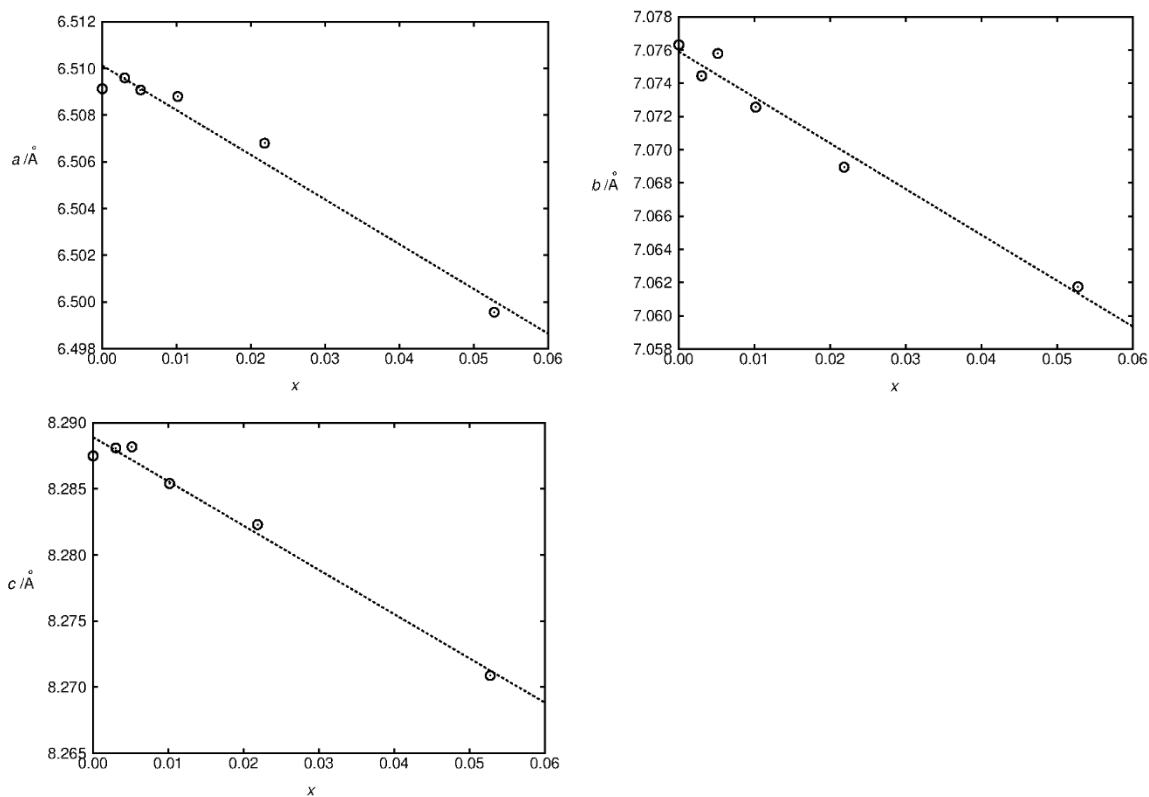
Figure S3. Lattice parameters as a function of the substitution degree x in the co-precipitated and 1000 °C sintered $La_{1-x}Ho_xPO_4$, as determined by Rietveld refinement based on X-ray powder diffraction data. The dotted lines represent linear fits resulting in $a/\text{Å} = 6.5101 - 0.1914 \cdot x$, $b/\text{Å} = 7.0759 - 0.2761 \cdot x$ and $c/\text{Å} = 8.2889 - 0.3349 \cdot x$, respectively.
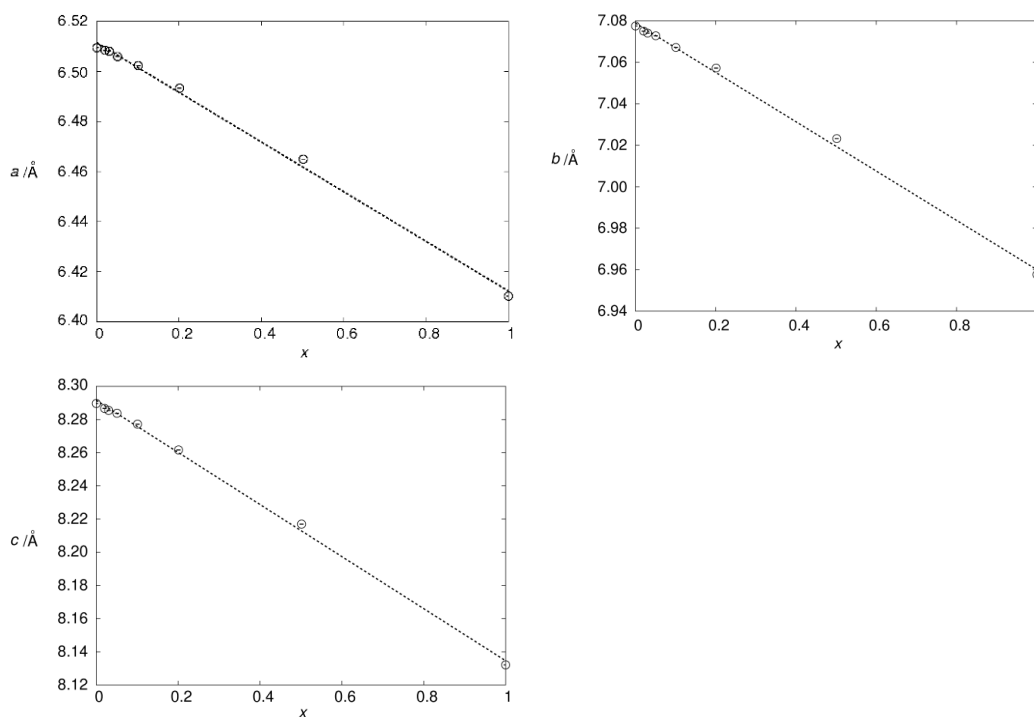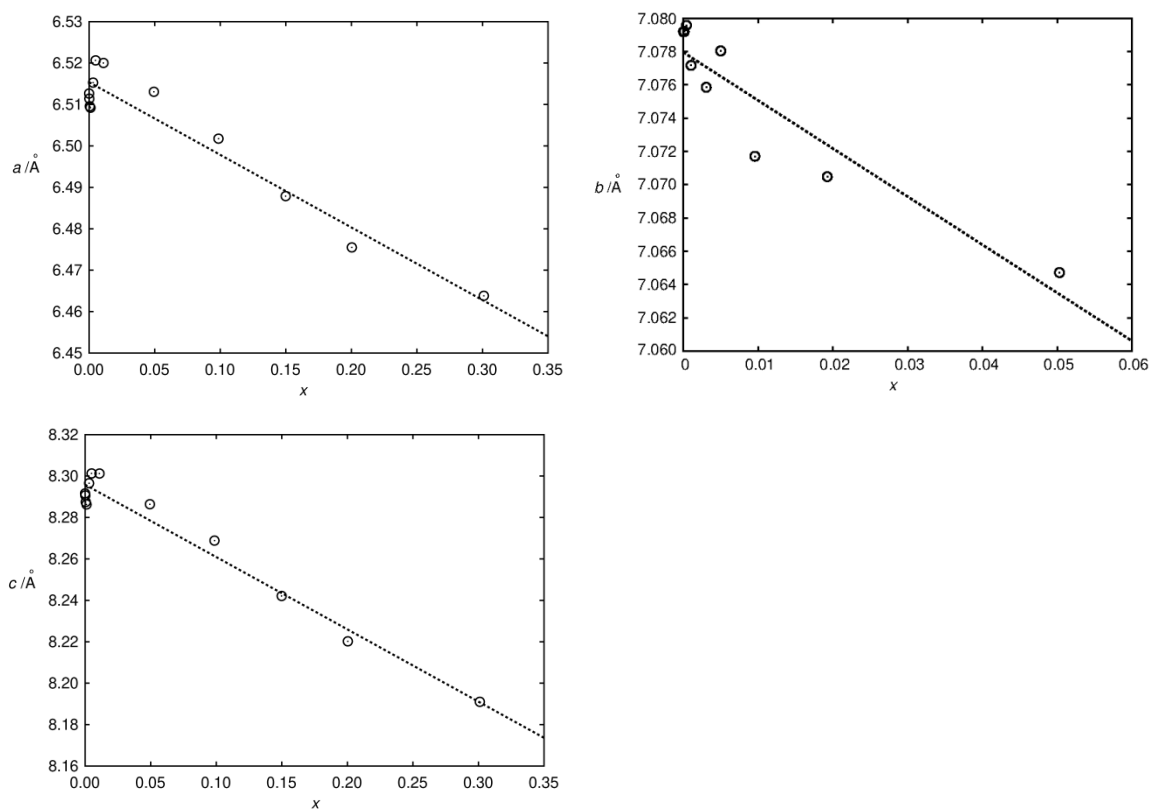
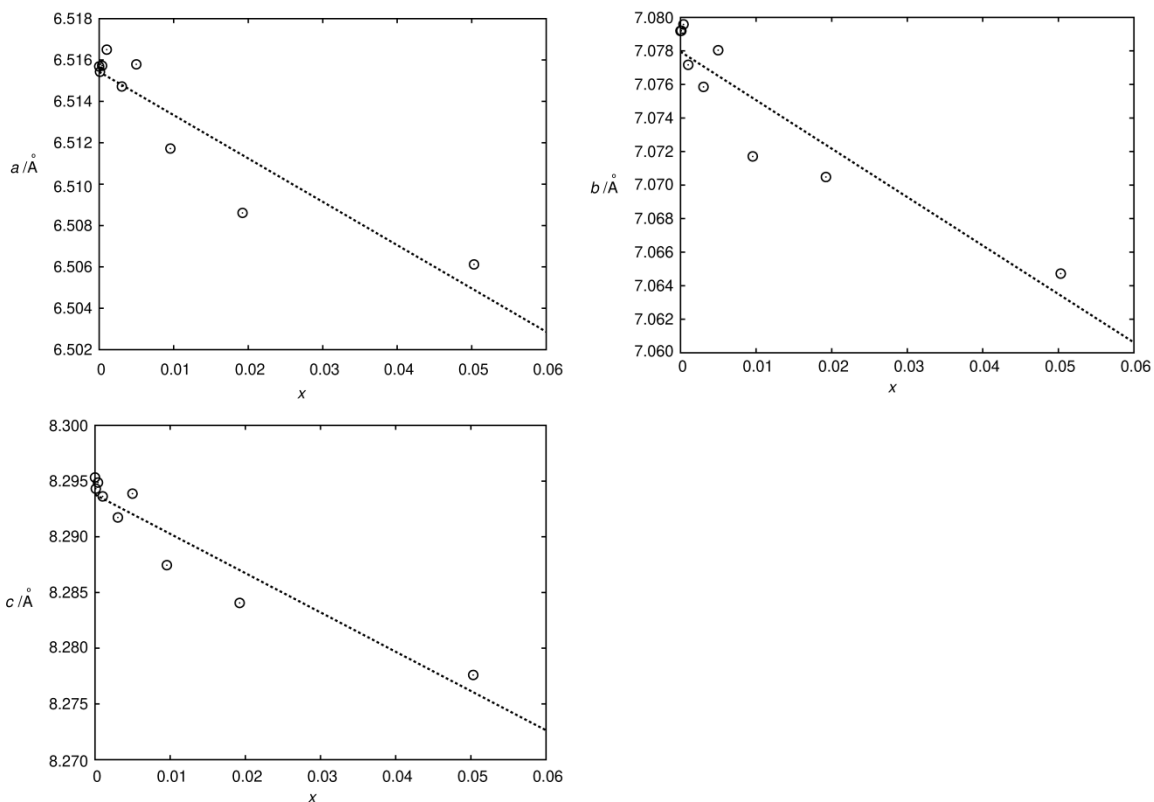**Figure S4.** Lattice parameters as a function of the substitution degree x in the co-precipitated and 1000 °C sintered $La_{1-x}Yb_xPO_4$, as determined by Rietveld refinement based on X-ray powder diffraction data. The dotted lines represent linear fits resulting in $a/\text{Å} = 6.5154 - 0.1753 \cdot x$, $b/\text{Å} = 7.0807 - 0.2994 \cdot x$ and $c/\text{Å} = 8.2958 - 0.3492 \cdot x$, respectively.

2. XRD diffractograms

For the 1000°C sintered solid state samples, at high doping concentration ($x \geq 0.2$), phase separation of $LnPO_4$ and $LaPO_4$ becomes evident from diffractograms. Nd doped $LaPO_4$ samples aimed at $x = 0.5$ were shown as examples. The XRD pattern of the solid state sample (Fig. S5 left) shown phase separation of $LaPO_4$ and $NdPO_4$. No phase separation was observed for corresponding co-precipitated sample (Fig. S5 right).
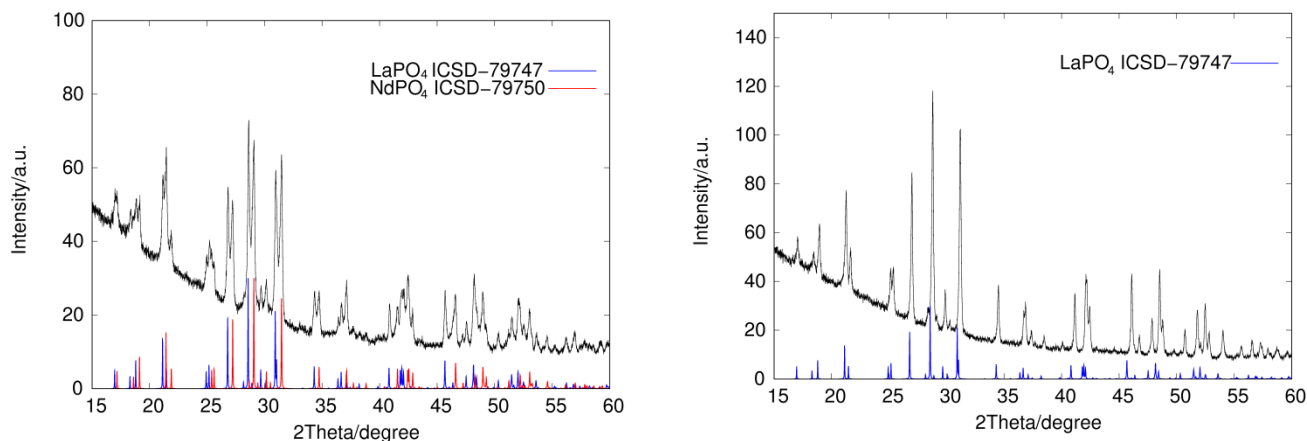
Figure S5. The powder XRD pattern of Nd doped $LaPO_4$ samples aimed at $x=0.5$, compared with literature data (ICSD-79747[1] for $LaPO_4$ and 79750[1] for $NdPO_4$). Left: solid state method synthesized, right: co-precipitation method synthesized sample.

3. NMR visibility curves

To establish the scale on which homogeneity is studied by NMR, the ^{31}P MAS NMR spectra were first obtained for the doped sample series $La_{1-x}Ln_xPO_4$ (Ln = Nd, Gd, Ho, Er, Tm, Yb). Only one signal was observed (Fig. S6) and as the doping level x increases, the peak area gradually decreases as shown in the ^{31}P MAS NMR spectra stack plots (Fig. S7-S12). Such data sets of the peak area of the homogeneous compounds $La_{1-x}Ln_xPO_4$ (Ln = Nd, Gd, Ho, Er, Tm, Yb) were fitted with the visibility function[2] $f(x) = \exp(-ar_0^3x)$ for the wipe-out radii r_0 of blind spheres. The $f(x)$ plots were shown next to the corresponding NMR stack plots in the Fig. S7-S12. NMR data from samples which were obtained from the solid state method were also compared along (Fig. S7-S12), and the deviation from the NMR visibility function indicates heterogeneity. For all mentioned Ln^{3+} dopants, homogeneously and heterogeneously doped samples can be distinguished. Therefore such method based on the

NMR visibility function serves as a nice tool for the evaluation of "NMR homogeneity". Based on the radii r_0 of the blind spheres,[3] it may be concluded that "NMR homogeneity" relies on a length scale of about 1 nm, and the co-precipitated samples (annealed at 1000 °C) are more homogeneously doped on nm scale.
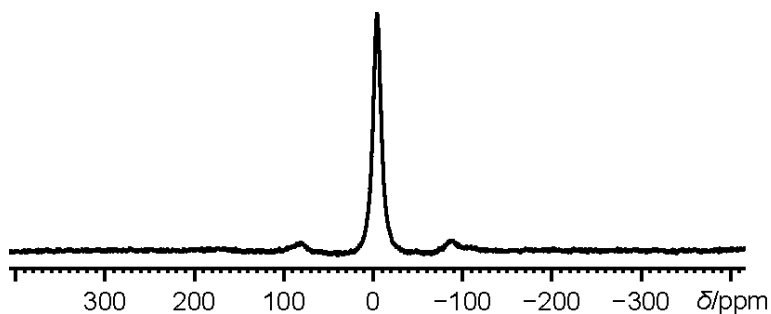
Figure S6. The ^{31}P MAS NMR full spectrum (spectrum width 100 kHz) of $La_{0.995}Dy_{0.005}PO_4$ obtained by co-precipitation method, which is shown as one example to demonstrate typical spectra of Ln doped $LaPO_4$ series. Only one P signal with its spinning side band were observed.

Figure S7. The stack plot of ^{31}P NMR spectra for $La_{1-x}Nd_xPO_4$ obtained by co-precipitation method (left), and the normalized NMR visibility $f(x)$ as a function of doping concentration x (right), for $La_{1-x}Nd_xPO_4$ obtained by co-precipitation method (circles) and solid state method (squares), both sintered at 1000 °C. The dashed line features the best fit of $f(x) = \exp(-ar^3x)$ with $a = 0.055/Å^3$ and $r_0 = 5.5$ Å to the points of samples from the co-precipitation method.
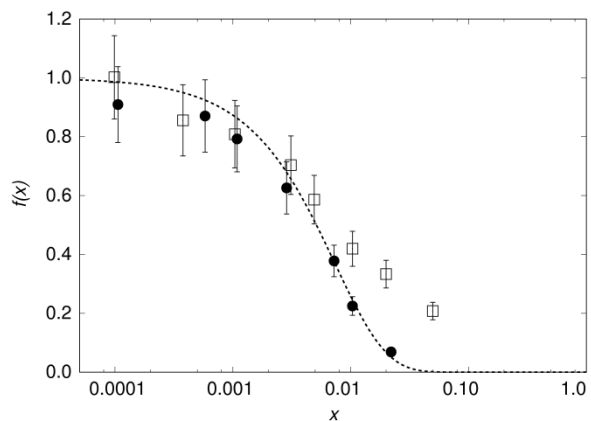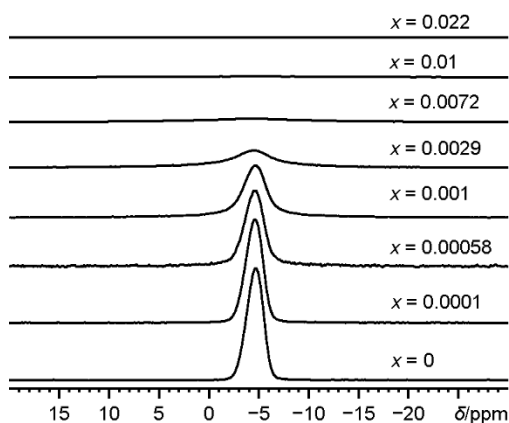
Figure S8. The stack plot of ^{31}P NMR spectra for La$_{1-x}$Gd$_x$PO$_4$ obtained by co-precipitation method (left), and the normalized NMR visibility $f(x)$ as a function of doping concentration x (right), for La$_{1-x}$Gd$_x$PO$_4$ obtained by co-precipitation method (circles) and solid state method (squares), both sintered at 1000 °C. The dashed line features the best fit of $f(x) = \exp(-ar^3x)$ with $a = 0.055/\text{Å}^3$ and $r_0 = 13.5$ Å to the points of samples from the co-precipitation method.
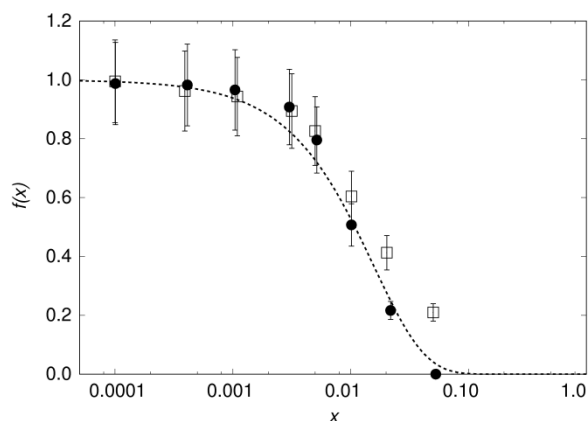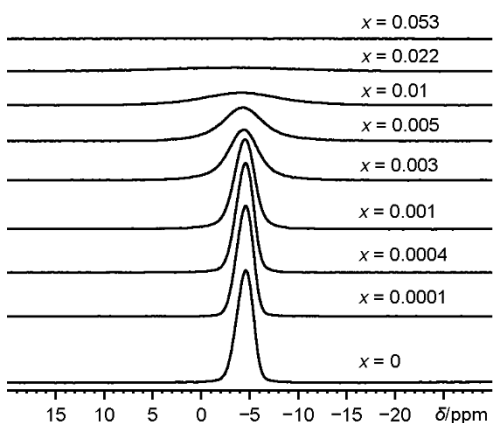
Figure S9. The stack plot of ^{31}P NMR spectra for La$_{1-x}$Ho$_x$PO$_4$ obtained by co-precipitation method (left) and the normalized NMR visibility $f(x)$ as a function of doping concentration x (right), for La$_{1-x}$Ho$_x$PO$_4$ obtained by co-precipitation method (circles) and solid state method (squares), both sintered at 1000 °C. The dashed line features the best fit of $f(x) = \exp(-ar^3x)$ with $a = 0.055/\text{Å}^3$ and $r_0 = 10.5$ Å to the points of samples from the co-precipitation method.
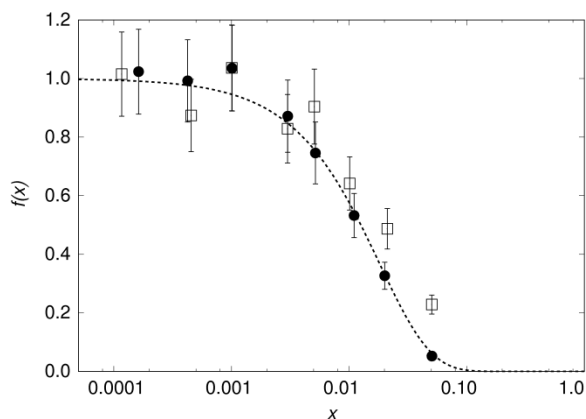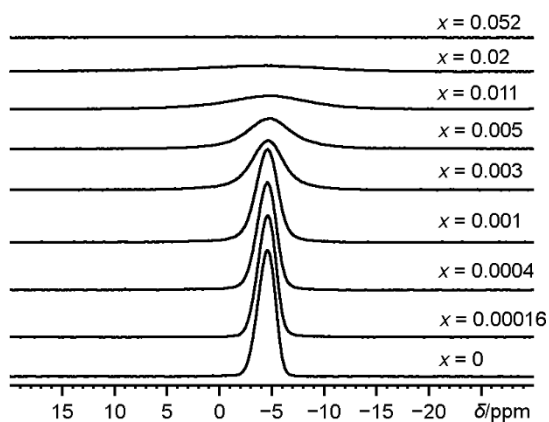
Figure S10. The stack plot of ^{31}P NMR spectra for $La_{1-x}Er_xPO_4$ obtained by co-precipitation method (left) and the normalized NMR visibility $f(x)$ as a function of doping concentration x (right), for $La_{1-x}Er_xPO_4$ obtained by co-precipitation method (circles) and solid state method (squares), both sintered at 1000 °C. The dashed line features the best fit of $f(x) = exp(-ar^3x)$ with $a = 0.055/Å^3$ and $r_0 = 10$ Å to the points of samples from the co-precipitation method.
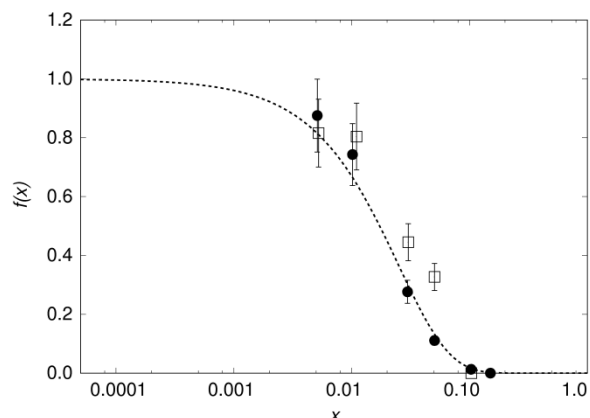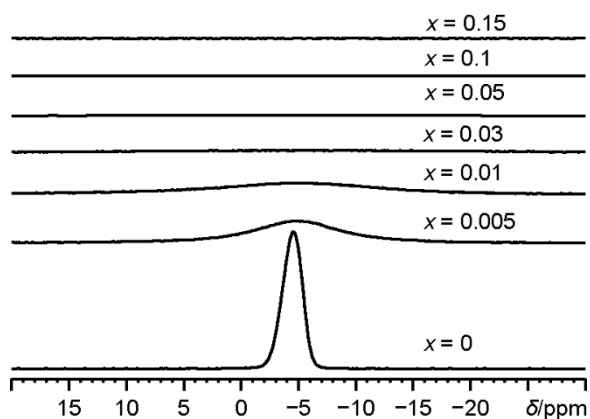
Figure S11. The stack plot of ^{31}P NMR spectra for $La_{1-x}Tm_xPO_4$ obtained by co-precipitation method (left) and the normalized NMR visibility $f(x)$ as a function of doping concentration x (right), for $La_{1-x}Tm_xPO_4$ obtained by co-precipitation method (circles) and solid state method (squares), both sintered at 1000 °C. The dashed line features the best fit of $f(x) = exp(-ar^3x)$ with $a = 0.055/Å^3$ and $r_0 = 9$ Å to the points of samples from the co-precipitation method.
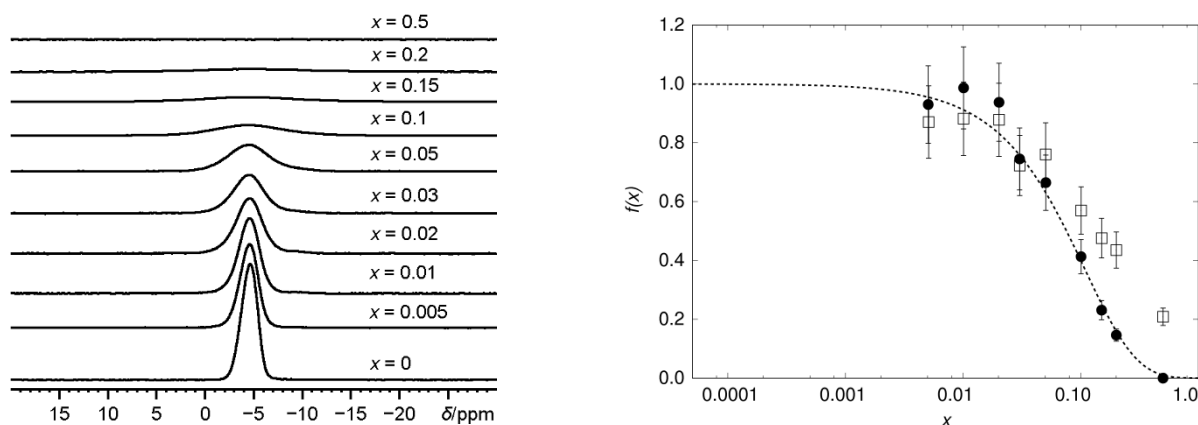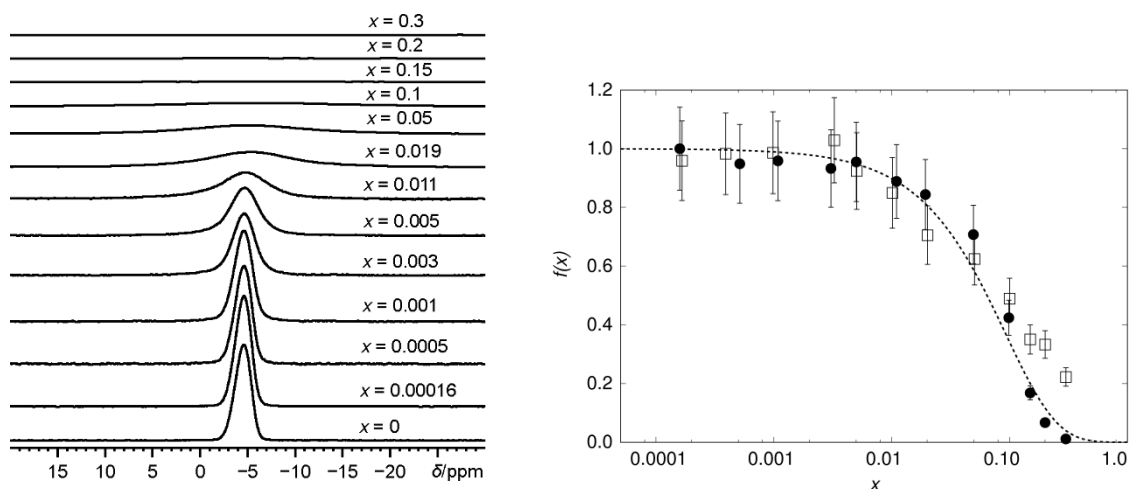
Figure S12. The stack plot of ^{31}P NMR spectra for La$_{1-x}$Yb$_x$PO$_4$ obtained by co-precipitation method (left) and the normalized NMR visibility $f(x)$ as a function of doping concentration x (right), for La$_{1-x}$Yb$_x$PO$_4$ obtained by co-precipitation method (circles) and solid state method (squares), both sintered at 1000 °C. The dashed line features the best fit of $f(x) = \exp(-ar^3x)$ with $a = 0.055/\text{Å}^3$ and $r_0 = 5.8$ Å to the points of samples from the co-precipitation method.

## 4. Lifetime of La$_{1-x}$Dy$_x$PO$_4$ doping series

The fluorescence lifetime of the La$_{1-x}$Dy$_x$PO$_4$ doping series has been obtained from the multi-exponential (equation **Fehler! Verweisquelle konnte nicht gefunden werden.** and 2) fitting of the intensity decay curve (Fig. S13-S19). I_{offset} was due to the dark counts and the corresponding parameter $c_{offset} = I_{offset}/I_0$ is also fitted (Table S1 and S2). I_0 is the initial intensity, which was set to be the intensity of the first data point in the decay curve. τ_1, τ_2 and τ_3 are the lifetime and a_1, a_2 and a_3 are the fitted weight fractions, respectively. In particular, a_1 is the mono-exponentiality factor.

The results shown in Tables S1 and S2 are the results of a single unconstrained non-linear least square fit of all slifetime curves with a self-written tcl-script including an error analysis based on a variance analysis. The fit model used different a_1, a_2, a_3 and I_{offset} / I_0 parameters for the different lifetime curves but assumed the lifetime values τ_1, τ_2 and τ_3 to be the same for both sample series. The fit converged consistently to the same minimal value independent of small changes in the starting values.

The values in Table S1 and S2 were used to produce Figure 6 in the manuscript.

Table S1. The fitting parameters including weight fractions a_1, a_2, a_3 and intensity offset c_{offset} for the lifetime measurements of samples obtained from co-precipitation method. The lifetime values are $\tau_1 = 1.099 \pm 0.003$ ms, $\tau_2 = 0.583 \pm 0.007$ ms, $\tau_3 = 0.099 \pm 0.002$ ms.

x	a_1	a_2	a_3	c_{offset}
0.0004	0.921±0.009	0.034±0.008	0.045±0.005	0.0049±0.0002
0.001	0.920±0.009	0.080±0.008	0.000±0.005	0.0008±0.0002
0.003	0.866±0.008	0.128±0.007	0.006±0.005	0.0000±0.0002
0.005	0.816±0.007	0.071±0.006	0.114±0.004	0.0006±0.0002
0.01	0.549±0.006	0.428±0.006	0.023±0.005	0.0019±0.0002
0.02	0.451±0.007	0.511±0.008	0.038±0.007	0.0018±0.0003
0.05	0.000±0.010	0.660±0.008	0.340±0.005	0.0059±0.0006

Table S2. The fitting parameters including weight fractions a_1, a_2, a_3 and intensity offset I_{offset} for the lifetime measurements of samples obtained from solid state method.

x	a_1	a_2	a_3	c_{offset}
0.0004	0.898±0.009	0.000±0.008	0.102±0.005	0.0055±0.0002
0.001	0.901±0.008	0.019±0.008	0.080±0.005	0.0022±0.0002
0.003	0.773±0.006	0.101±0.006	0.126±0.004	0.0011±0.0002
0.005	0.684±0.006	0.169±0.005	0.147±0.004	0.0004±0.0002
0.01	0.508±0.007	0.421±0.007	0.072±0.007	0.0007±0.0003
0.02	0.337±0.007	0.573±0.008	0.091±0.007	0.0006±0.0003
0.05	0.116±0.007	0.529±0.006	0.355±0.005	0.0041±0.0005
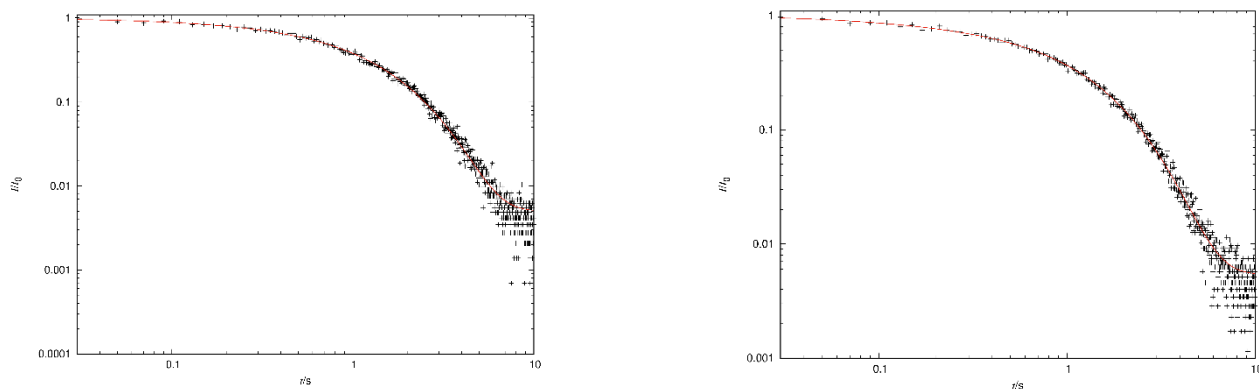
Figure S13. The decay curves from lifetime measurements of $La_{0.9996}Dy_{0.0004}PO_4$ samples, obtained by co-precipitation method with sintering temperature 1000°C (left) and solid state method 1000°C (right). The dashed lines represent the fitting function as equation 2 with fitting parameters in table S1 (left) and S2 (right), respectively. The measurements were recorded at emission wavelength λ_{em} = 477 nm and excitation wavelength λ_{ex} = 350 nm.
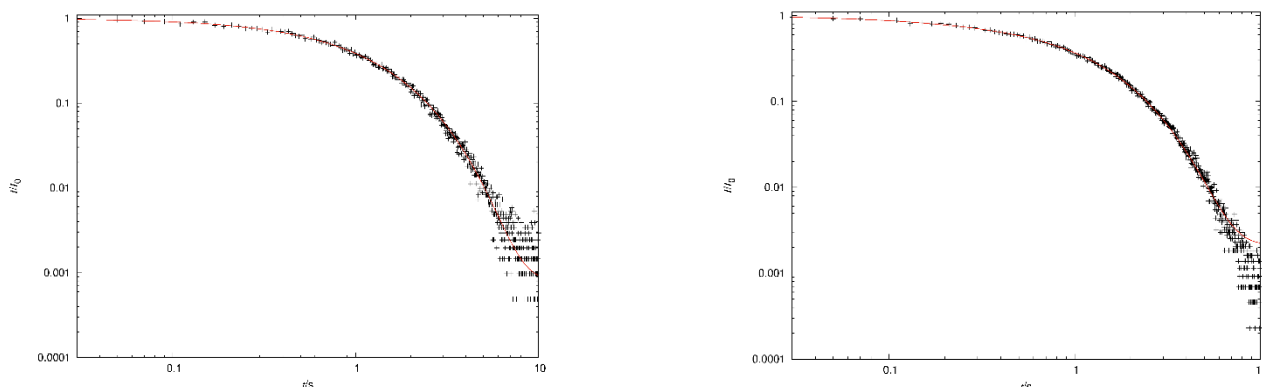
Figure S14. The decay curves from lifetime measurements of $La_{0.999}Dy_{0.001}PO_4$ samples, obtained by co-precipitation method with sintering temperature 1000°C (left) and solid state method 1000°C (right). The dashed lines represent the fitting function as equation 2 with fitting parameters in table S1 (left) and S2 (right), respectively. The measurements were recorded at emission wavelength λ_{em} = 477 nm and excitation wavelength λ_{ex} = 350 nm.
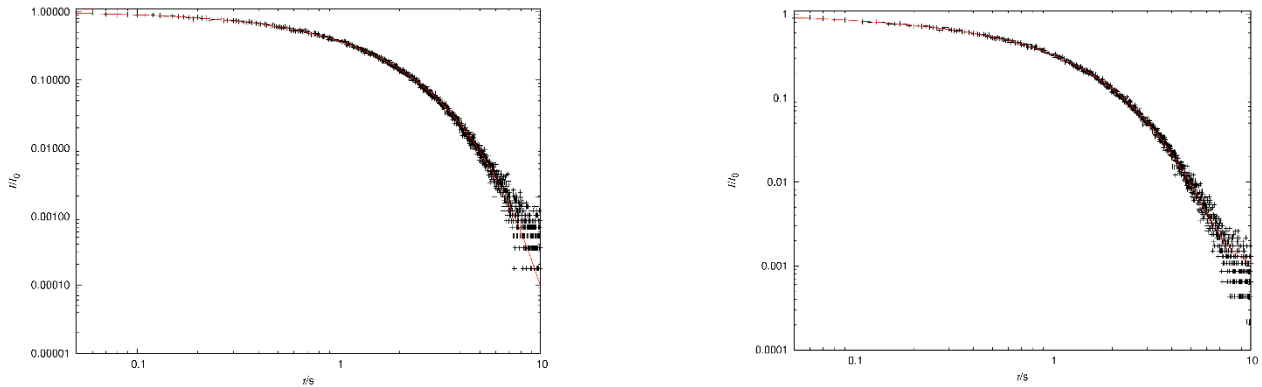
Figure S15. The decay curves from lifetime measurements of $La_{0.997}Dy_{0.003}PO_4$ samples, obtained by co-precipitation method with sintering temperature 1000°C (left) and solid state method 1000°C (right). The dashed lines represent the fitting function as equation 2 with fitting parameters in table S1 (left) and S2 (right), respectively. The measurements were recorded at emission wavelength λ_{em} = 477 nm and excitation wavelength λ_{ex} = 350 nm.
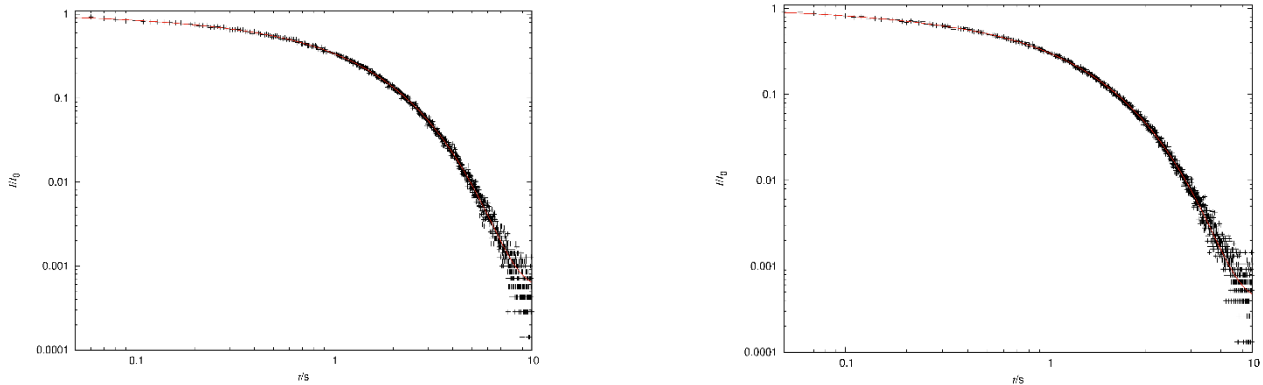
Figure S16. The decay curves from lifetime measurements of $La_{0.995}Dy_{0.005}PO_4$ samples, obtained by co-precipitation method with sintering temperature 1000°C (left) and solid state method 1000°C (right). The dashed lines represent the fitting function as equation 2 with fitting parameters in table S1 (left) and S2 (right), respectively. The measurements were recorded at emission wavelength λ_{em} = 477 nm and excitation wavelength λ_{ex} = 350 nm.
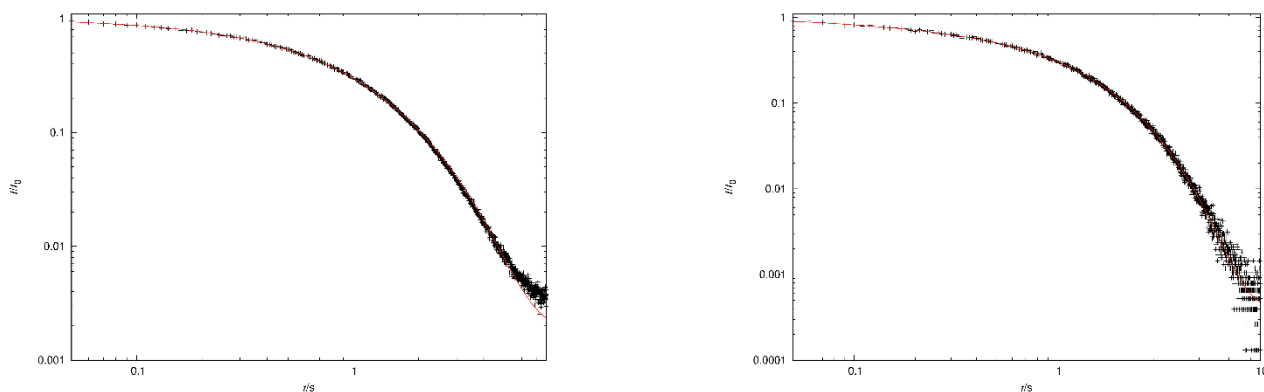
Figure S17. The decay curves from lifetime measurements of $La_{0.99}Dy_{0.01}PO_4$ samples, obtained by co-precipitation method with sintering temperature 1000°C (left) and solid state method 1000°C (right). The dashed lines represent the fitting function as equation 2 with fitting parameters in table S1 (left) and S2 (right), respectively. The measurements were recorded at emission wavelength λ_{em} = 477 nm and excitation wavelength λ_{ex} = 350 nm.
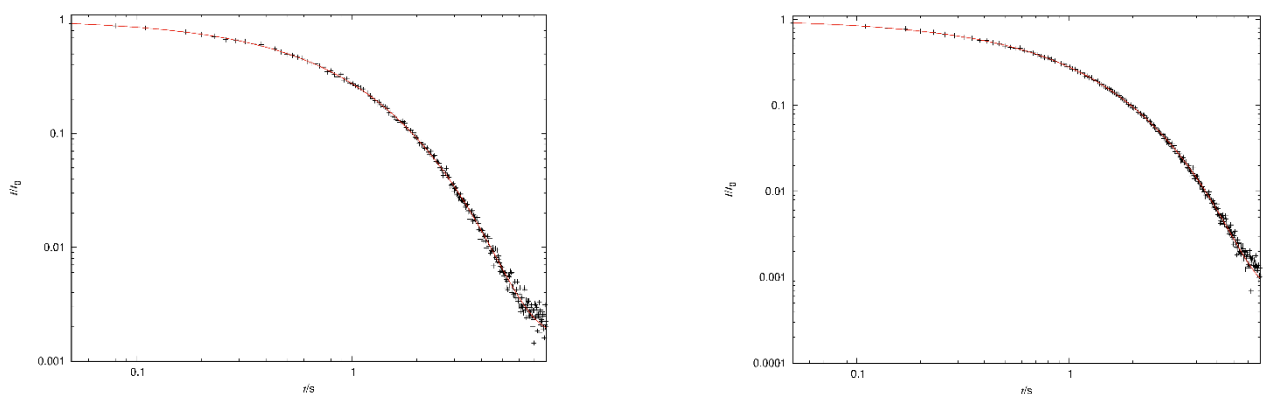
Figure S18. The decay curves from lifetime measurements of $La_{0.98}Dy_{0.02}PO_4$ samples, obtained by co-precipitation method with sintering temperature 1000°C (left) and solid state method 1000°C (right). The dashed lines represent the fitting function as equation 2 with fitting parameters in table S1 (left) and S2 (right), respectively. The measurements were recorded at emission wavelength λ_{em} = 477 nm and excitation wavelength λ_{ex} = 350 nm.
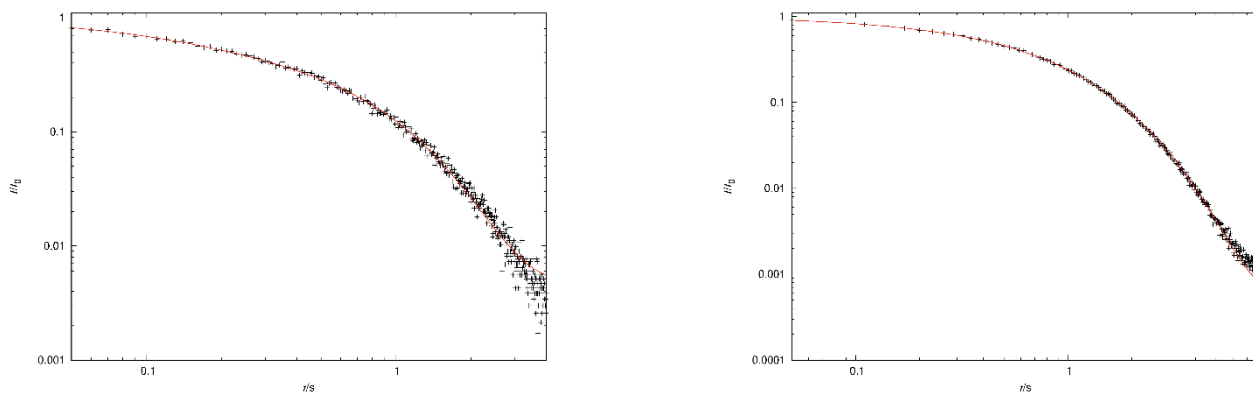
Figure S19. The decay curves from lifetime measurements of $La_{0.95}Dy_{0.05}PO_4$ samples, obtained by co-precipitation method with sintering temperature 1000°C (left) and solid state method 1000°C (right). The dashed lines represent the fitting function as equation 2 with fitting parameters in table S1 (left) and S2 (right), respectively. The measurements were recorded at emission wavelength λ_{em} = 477 nm and excitation wavelength λ_{ex} = 350 nm.

References

[1]   Y. Ni, J. M. Hughes , A. N. Mariano, *Am. Mineral.*, **1995**, *80*, 21–26.
[2]   W. Li, V. R. Celinski, J. Weber, N. Kunkel, H. Kohlmann, J. Schmedt auf der Günne, *Phys. Chem. Chem. Phys.* **2016**, *18*, 9752–9757.
[3]   W. Li, Q. Zhang, J. J. Joos, P. F. Smet, J. Schmedt auf der Günne, *Phys. Chem. Chem. Phys.* **2019**, *21*, 10185–10194.

3.4 Doping Homogeneity in Co-doped Materials Investigated at Different Length Scales

Wenyu Li, Philippe F. Smet, Lisa I. D. J. Martin, Christian Pritzel and Jörn Schmedt auf der Günne

Phys. Chem. Chem. Phys. **2020**, *22*, 818–825

Contribution to the manuscript:

Based on discussions and conceptual guidance from Jörn Schmedt auf der Günne, the NMR study and all NMR related data analysis were done by me. The synthesis was done by me and optimized during a practicum course. The Monte Carlo simulations of the EDX signal, the CL spectra and the SEM-CL-EDX analysis have been performed by Lisa I. D. J. Martin and Philippe F. Smet. The EDX mapping was recorded by Christian Pritzel. This paper was drafted by me and perfected by Jörn Schmedt auf der Günne and Philippe F. Smet.

Check for updates

Doping homogeneity in co-doped materials investigated at different length scales†

Wenyu Li, [a] Philippe F. Smet, *[b] Lisa I. D. J. Martin, [b] Christian Pritzel[c] and Jörn Schmedt auf der Günne *[a]

Doping homogeneity is important for the properties of co-doped phosphors, as it can affect the energy transfer between sensitizer and activator ions. In a case study we apply different methods, that is scanning electron microscopy (SEM) combined with energy dispersive X-ray spectroscopy (EDX) mapping, SEM combined with cathodoluminescence (CL) and solid-state nuclear magnetic resonance (NMR), to study the doping homogeneity of the host system monazite $LaPO_4$ doped with two different lanthanide ions on different length scales. A new criterion for doping heterogeneity in co-doped systems is developed, which is based on the NMR visibility function, which for this purpose is extended to doping with two or more paramagnetic dopants. A deviation from this function is indicative of doping heterogeneity on the length-scale of the blind-spheres of the paramagnetic dopants. A discussion of the advantages and disadvantages of the different methods is presented. The combined approach allows to study doping homogeneity from the nm to the μm scale.

Introduction

Co-doping is often utilized to achieve extra performance for functional materials. For example, defect populations can be manipulated by co-doping in semi-conductors[1] to achieve changes in conductivity or in luminescence materials to achieve higher efficiency,[2] brightness or longer afterglow.[3] For glass lasers[4] co-doping makes a higher dopant-solubility and thermal tolerance possible. Not only the choice of suitable pairs of co-dopants needs to be considered depending on the application scenario, but also the distribution of the co-dopants in the host material is important. Co-doped afterglow materials for example critically depend on energy transfer[5,6] processes between different dopant ions which are limited by their distance. As an example, the addition of Dy^{3+} to the $SrAl_2O_4$:Eu^{2+} persistent phosphor increases the brightness and the duration of the afterglow.[7] However, partial segregation of dysprosium has been observed at grain boundaries, affecting the actual dopant concentration inside the phosphor particles.[8]

In general the concept homogeneity depends on a length scale or a volume.[9] For example a glass sample may appear

homogeneous when investigated by visible light but heterogeneous on an atomic scale. In case of co-doped phosphors the interesting length scale is of the order of the energy transfer distance (up to a few nm, depending on the transfer mechanism).[5,6] In the present case we refer to "homogeneous doping" if the La atoms in the host material are statistically replaced by the lanthanides (Ln) used for doping. While different techniques are able to elucidate the distribution of dopants in the host matrix on different length scale, it turns out that it is not easy to "prove" doping homogeneity. Instead the usual approach is to disprove heterogeneity on different length scales. Analytical methods can establish heterogeneity in different ways: X-ray diffraction (XRD) as a bulk technique can be used to establish heterogeneity by deviation of the lattice parameters from Vegard's rule[10] or by the appearance of a non-statistical pair distribution function[11] given that the scattering contrast is sufficient. X-ray photoelectron spectroscopy (XPS) offers information about the dopant distribution at the surface on the nm scale.[12] Methods based on electron microscopy can prove heterogeneity at a specific location in the sample but not in the bulk. For example, transmission electron microscopy can provide line-scans showing a dopant distribution profile on the nm scale for thin sample layers.[13] Energy dispersive X-ray (EDX) mapping in a scanning electron microscope (SEM) can show heterogeneous dopant distributions on the sub-μm scale[14,15] at a sample surface to a depth of several μm, depending on the accelerator voltage[13] (see below). EDX is considered to be a semi-quantitative analysis technique, as the number of detected X-rays depends on the accelerating voltage, the sample composition, the detection angle

[a] *Inorganic Materials Chemistry, University of Siegen, Adolf-Reichwein-Str. 2, 57076 Siegen, Germany. E-mail: gunnej@chemie.uni-siegen.de*

[b] *Department of Solid State Sciences, Ghent University, Krijgslaan 281-S1, 9000 Gent, Belgium. E-mail: Philippe.Smet@UGent.be*

[c] *Construction and Materials Chemistry, University of Siegen, Paul-Bonatz-Str. 9-11, 57076 Siegen, Germany*

and the sample morphology, with especially the latter effect not being easy to correct for. Cathodoluminescence (CL) imaging evaluates the spatial and spectral distribution of the emitted light after excitation by the electron beam. For a certain fixed position of the electron beam, light is generated in a similar volume compared to the characteristic X-rays. The advantage over EDX is an increased sensitivity, allowing to study lower impurity concentrations. Finally, the luminescence characteristics of many impurities depend on the local environment. Hence, the shape of the CL emission spectrum can be used to probe the local chemical composition.[16,17] Electron paramagnetic resonance (EPR) studies the signals from paramagnetic dopants in low concentration and extracts information on distribution as well as local environment[18] from spectroscopic parameters such as the lineshape.[19] A broad linewidth is typical for strong couplings and indicative of heterogeneity.[20]

In this contribution solid-state NMR is used to investigate co-doping heterogeneity. In case of a diamagnetic solid host with NMR-active nuclei solid-state NMR has been used to investigate the dopant distribution of a single kind of paramagnetic dopant ("mono-doped") in different ways: spin–lattice T_1 relaxation,[21–23] line width[24–26] and visibility function (see below).[27,28] A T_1–T_2 correlation map was also shown to be useful in studying a paramagnetic site distribution at the surface of porous materials.[29] These NMR observables of the host-material are influenced by the hyperfine interaction[30,31] between the unpaired electrons of a paramagnetic dopant and the NMR-active nucleus in a non-trivial way in general. For Ln(III) dopants the valence electrons are situated in f-orbitals for which the spin–orbit (SO) interactions dominate over ligand field effects as compared to transition metal atoms for which the order is reversed.[32] Thus the magnetism of Ln(III) ions can be predicted neglecting ligand field effects in the high-temperature regime with the exception of Sm(III) and Eu(III). In fact the NMR visibility function, the relaxation behavior and the line-width of host signals have been shown to correlate in a simple way with an increasing Ln(III) doping concentration for the host chosen here.[26] Here we make use of the NMR visibility, which is the molar peak area of NMR signal of a paramagnetically doped compound normalized by that of the undoped host. The visibility function is the NMR visibility as a function of doping concentration that can be approximated analytically by a decaying exponential function, if it is assumed that around every paramagnetic dopant a certain volume exists within which NMR nuclei become "invisible" to the NMR experiment. Invisible here means that signals decay very fast so that they do not contribute to the FID which is sampled after the spectrometer deadtime. This concept was independently introduced by different groups in the context of dynamic nuclear polarization[33] and for the purpose of studying doping homogeneity.[27] It could be shown that in a homogeneous system the visible percentage of the host NMR signal decays in an exponential fashion with increasing doping concentration which can be used to estimate the radius of the blind sphere around a paramagnetic center (formula see experimental part).[26,27] In mono-doped materials deviations from this exponential function may serve as a criterion of doping heterogeneity in the above sense on the

length scale of the blind-sphere radius[26–28] which typically takes values up to ~ 2 nm. While in general it may not always be trivial to explain what contributes to the blind sphere radius it appears that for Ln(III) dopants the pseudo-contact shielding is strongly correlated with the size of the blind sphere.[26] Correspondingly the blind-spheres for different NMR active nuclei in the same material are related to the size of the gyromagnetic ratio.[26] The only known exception for Ln(III) dopants is Gd(III) which is known for its very special relaxation behavior which also makes it an effective contrast agent in magnetic resonance imaging.[31]

Given the interest in co-doped luminescent materials the target of this study is to investigate whether the NMR visibility function can be extended to co-doped systems and to compare this approach to other commonly used techniques to investigate doping homogeneity.

Experimental

Reference materials for co-doped monazite $LaPO_4$ were obtained with a co-precipitation method and subsequent annealing which previously had been shown to produce homogeneously mono-doped samples.[26,28] The starting reagents, which include La_2O_3 (ChemPur, 99.99%) and dopant materials Gd_2O_3 (smart elements, 99.99%), Dy_2O_3 (smart elements, 99.999%), Ho_2O_3 (smart elements, 99.99%), Yb_2O_3 (smart elements, 99.99%) and Nd_2O_3 (ChemPur, 99.99%), were mixed and dissolved in the required ratios in concentrated nitric acid. Upon adding $NH_4H_2PO_4$ (VWR chemicals) solution in excess a precipitate is formed, washed with water and ethanol, then centrifuged and dried overnight. Annealing is done in corundum crucibles at 1000 °C for 4 h.

Solid state NMR measurements were performed on a Bruker Avance II spectrometer at 7.05 T. Magic angle spinning (MAS) was done with 4 mm pencil rotors at 10 kHz with a home-built McKay probe head and a dead-time delay of 15 μs. External quantification of the NMR signals was assisted with a micro-balance (Sartorius MC5). The NMR visibility f was calculated as the observed peak area of the ^{31}P NMR signal per mole of the sample normalized by the peak area per mole of non-doped diamagnetic host. Deconvolution of NMR peaks was done with the program deconv2Dxy.[34] The NMR visibility fitting function[27,28] for a homogeneously mono-doped sample is defined as $f(x) = \exp(-ar_0^3 x)$, where r_0 is the blind-sphere radius, a is a parameter related to the number density of dopable sites ($a = 4/3\pi N_{hostUC}/V_{UC}$), N_{hostUC} is the number of "dopable" sites in the unit cell, x is the fraction of atoms substituted by a paramagnetic dopant (see example) and V_{UC} is the volume of the unit cell. For example, for monazite[35] doped with Dy, i.e. $LaPO_4$:Dy or $La_{1-x}Dy_xPO_4$, a is 0.055 Å^{-3}.

Scanning electron microscopy images were obtained in back-scattered electron detection mode (Hitachi S-3400 N). For elemental mapping with EDX, the connected ThermoScientific Noran System 7 was used. CL radiation emitted by the sample was collected for a 256-by-184 grid (dwell time of 100 ms per point) with an optical fiber and delivered to an Acton SP2300 monochromator

This journal is © the Owner Societies 2020

Phys. Chem. Chem. Phys., 2020, **22**, 818–825 | 819

and ProEM 1600EMCCDcamera (Princeton Instruments). CL spectra and intensities were processed off-line. All spectra were measured at room temperature and with an accelerating voltage of 20 kV. To avoid electrical charging of the sample, and the associated image deformations, a low background pressure of 20 Pa was used. For EDX quantification of the lanthanide ion concentrations, the L lines were monitored (La: 4.7 keV, Nd: 5.2 keV, Tm: 7.2 keV).

Results and discussion

To investigate the effects of co-doping on the NMR visibility function, reference compounds are required which are homogeneously doped. To this end LaPO$_4$ was co-doped with Nd/Tm, Gd/Dy and Nd/Ho at different concentrations.

The synthesis recipe had been used before[26,28] to produce single-doped monazite which proved to be homogeneous according to XRD and NMR with respect to the Vegard behavior of the lattice parameters and the NMR visibility function,[27] respectively. In the following the doping homogeneity of co-doped LaPO$_4$ is first tested with energy dispersive X-ray mappings and cathodoluminescence. Finally it is shown how the NMR visibility function needs to be modified for application to co-doped materials.

1. Doping homogeneity according to EDX

Monazite LaPO$_4$ is obtained by dehydration of rhabdophane LaPO$_4$·H$_2$O which in turn is obtained by precipitation from a solution containing lanthanum and monophosphate ions. Depending on washing steps and how fast the precipitation is conducted, impurities by hydrogen phosphates can be observed which after high temperature annealing convert into LaP$_3$O$_9$.[36] This impurity (less than 5% based on NMR peak area quantification results) should not have an influence on the distribution of the lanthanide dopants but may cause the formation of grain boundaries and could give rise to deviations in electron microscopy which is sensitive to the surface of the particles. Powder X-ray diffraction (not shown) indicates a very small impurity of LaP$_3$O$_9$ which is consistent with ^{31}P MAS NMR. Other side phases could not be observed. Nevertheless, given that solubility limits for a solid solution of LaPO$_4$:Ln exist[37] and that light lanthanides prefer to crystallize in the monazite structure type but heavy lanthanides prefer to crystallize in the zircon structure type, it is reasonable to further investigate the distribution of lanthanide dopants.

Energy dispersive X-ray spectroscopy (EDX) in comparison to XRD is a local technique which elucidates sample composition by the emitted X-ray spectrum inside the excitation volume of the electron beam, which at 20 keV amounts to a 1–2 micrometers in LaPO$_4$. In electron micrographs and EDX maps (Fig. 1 and Fig. S1–S3, ESI†) grain boundaries with different composition in terms of the Ln/P ratio could be observed but apparently the total amount was too small to have an impact on the NMR experiments (see below). The element composition ratios for the different lanthanides reflect the batch composition of the starting
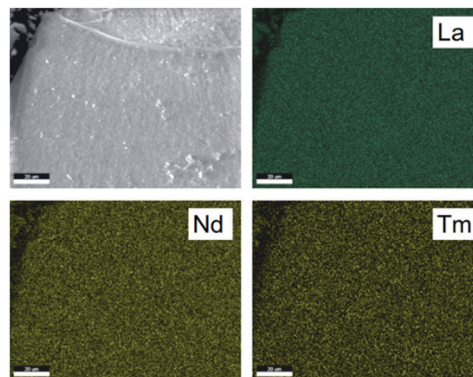
Fig. 1 Electron micrographs detected *via* backscattered electrons (top left) and EDX mappings (top right and bottom) of La$_{0.8}$Nd$_{0.1}$Tm$_{0.1}$PO$_4$. The acceleration voltage is 30 kV.

materials and are consistent with a homogeneous distribution throughout the material, at the sub-micron length scale. To assess the spatial resolution which could potentially be obtained in the studied material system, Monte Carlo simulations using Casino[38,39] have been performed, where the interactions of the incoming electrons with the sample are simulated, including the creation and eventual detection of characteristic X-rays. The chosen electron energy was 20 keV, as a compromise between EDX signal intensity and spatial resolution. Indeed, lowering the electron beam energy reduces the interaction volume, but simultaneously reduces the number of generated X-rays. Specifically for the studied LaPO$_4$:Ln system, the L-lines of the lanthanides are monitored, in order to avoid the strongly overlapping M-lines, which require an electron beam energy of at least 15 keV to have sufficient yield. Given the low concentrations (and thus also the corresponding EDX signal intensities) of the dopants with respect to the La present in the host, this is an experimental constraint. Consequently, it is not obvious what spatial resolution can be obtained if one wants to assess the dopant homogeneity in the co-doped LaPO$_4$ samples. Therefore, La$_{1-x}$(Nd,Tm)$_x$PO$_4$ was simulated as a model system (Fig. 2), where the doping was considered fully inhomogeneous.

A slab of La$_{0.99}$Tm$_{0.01}$PO$_4$ was inserted in between two slabs consisting of La$_{0.99}$Nd$_{0.01}$PO$_4$. The width of the central Tm doped slab was varied from 100 nm to 2 μm, while the (vertical) thickness was taken larger than the penetration depth of the electron beam. Then the electron beam was swept over the sample surface, across the three slabs. For each simulated point of incidence, the obtained EDX signal intensities for Nd and Tm were stored and plotted (Fig. 2). While the lanthanide concentrations follow a step like function, the concentration profile is smoothed by the interaction volume in the sample. For the widest central slab of 2 μm, the concentration profiles show that distinct regions can be found, where *e.g.* no X-rays originating from Nd are found. For narrower central slabs, a further smoothing occurs, and already at a central width of 1 μm, Nd is measured along the entire profile. When the central Tm-doped slab is only 100 nm wide, the Nd signal only drops by about 20% in the middle of the Tm-doped slab, as compared to positions far away from the central slab. Taking into account
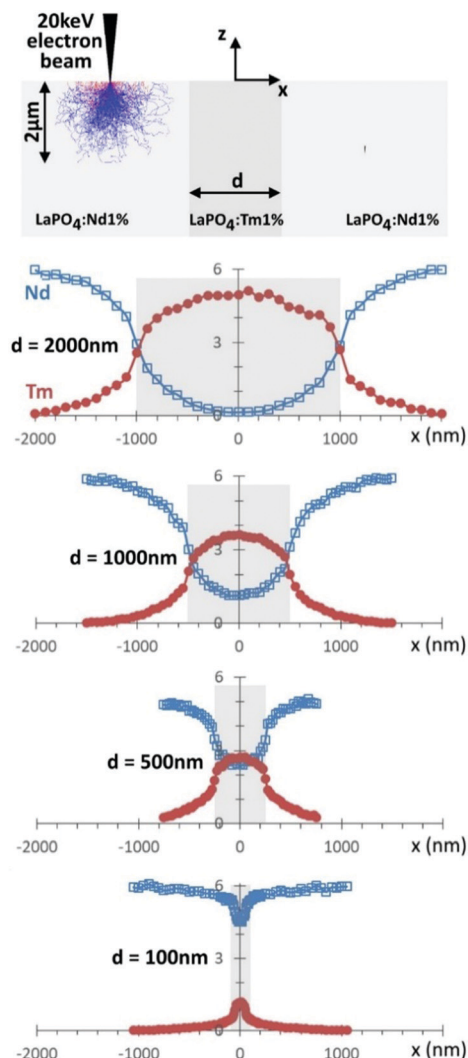
Fig. 2 Monte Carlo simulations of the EDX signal intensities of Nd and Tm were performed for a specific geometry of three slabs next each other, with the outer ones consisting of $La_{0.99}Nd_{0.01}PO_4$ and the central one, with thickness d, being $La_{0.99}Nd_{0.01}PO_4$ (see top schematic, which also includes the underlying electron paths of a typical simulation). The derived concentration profiles along the x direction are shown for different thicknesses d.

2. Fluorescence spectroscopy

When the electron beam hits the sample, also cathodoluminescent radiation is generated in a similar volume as the characteristic X-rays, used for the EDX analysis. The advantage is however that the CL emission can be strong, translating in a high signal intensity, and that the contributions in the emission spectrum can be related to specific luminescent ions, especially in the case of the 4f–4f emitting trivalent lanthanides. In principle, the emission intensity can be related to the local dopant concentration as there is a linear relation between both, until concentration quenching sets in, where the CL intensity increases sublinearly (or even reduces) for increasing dopant concentration.

The CL emission spectra of codoped $La_{0.984}Nd_{0.008}Tm_{0.008}PO_4$ and $La_{0.968}Nd_{0.016}Tm_{0.016}PO_4$, together with those for single doped $La_{0.995}Nd_{0.005}PO_4$ and $La_{0.995}Tm_{0.005}PO_4$, have been measured and compared (Fig. 3). Those spectra were acquired while the electron beam was continuously swept over a large area (100 μm × 100 μm) to find the average emission spectrum. The emission of $La_{0.995}Nd_{0.005}PO_4$ is dominated by the transitions in the infrared (with the $^4F_{3/2} \rightarrow ^4I_{9/2}$ transitions around 900 nm), accompanied by several transitions in the visible part of the spectrum, originating from the higher-lying $^2F(2)_{5/2}$, $^4D_{3/2}$ and $^2P_{3/2}$ levels.[40] For $La_{0.995}Tm_{0.005}PO_4$, the main emission bands are around 345 nm ($^3P_0 \rightarrow ^3F_4$), 360 nm ($^1D_2 \rightarrow ^3H_6$), 455 nm ($^3P_0 \rightarrow ^3H_4$, $^1D_2 \rightarrow ^3F_4$), 475 nm ($^1G_4 \rightarrow ^3H_6$), 650 nm ($^1G_4 \rightarrow ^3F_4$) and from 700 to 800 nm ($^3F_2$, $^3F_3$, $^3H_4 \rightarrow ^3H_6$).[41] No emission peaks related to other lanthanides were found, pointing at good purity of the prepared phosphors. The CL emission spectrum of the Nd, Tm co-doped $La_{0.984}Nd_{0.008}Tm_{0.008}PO_4$ is essentially the sum of the contributions of both Tm^{3+} and Nd^{3+} ions (Fig. 3c), although subtle differences can be spotted as function of the doping concentration, e.g. in the relative intensity of the Tm^{3+} transitions at 345 nm and 360 nm which originate from $^3P_0$ and $^1D_2$, respectively. To assess the degree of energy transfer between Tm^{3+} and Nd^{3+}, the dopant
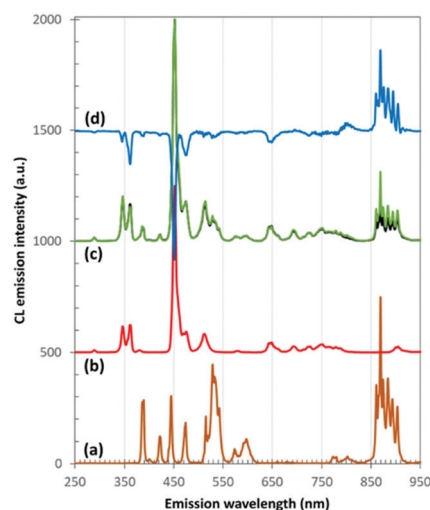
Fig. 3 The average CL emission spectra of (a) $La_{0.995}Nd_{0.005}PO_4$ and (b) $La_{0.995}Tm_{0.005}PO_4$. (c) CL emission spectra of $La_{0.984}Nd_{0.008}Tm_{0.008}PO_4$ (black) and $La_{0.968}Nd_{0.016}Tm_{0.016}PO_4$ (green). (d) Difference between both spectra in (c), multiplied by a factor of five.

the experimental constraints, where the Nd EDX signal will be low given the low doping concentration, the noise on each measured point will likely obscure this small dip in the concentration profile. Similarly, while there is for the central Tm-doped slab of 100 nm a clear increase in the Tm concentration when crossing this slab, the signal intensities will be fairly low (e.g. as when compared to the 2 μm wide slab), because the electrons spread laterally out into the Nd-doped slabs. Consequently, mapping of the dopant concentration by EDX will – under the mentioned constraints of signal intensity – not allow to quantitatively assess the dopant homogeneity on the submicron, or smaller, scale. Of course, if the (vertical) thickness of the sample can be reduced by preparing a thin slab, the spatial resolution increases, as the electrons leave the sample on the bottom side before they can spread too much laterally.

This journal is © the Owner Societies 2020

Phys. Chem. Chem. Phys., 2020, **22**, 818–825 | **821**

concentration of both Tm and Nd was doubled (*i.e.* the phosphor with composition $La_{0.968}Nd_{0.016}Tm_{0.016}PO_4$, Fig. 3c). This doesn't dramatically alter the emission spectrum and to better appreciate the differences, the difference spectrum between both co-doped samples is shown in Fig. 3d.

For $La_{0.968}Nd_{0.016}Tm_{0.016}PO_4$, the Nd^{3+} transitions in the near IR between 850 and 920 nm increase in relative intensity, while the Nd^{3+} transitions in the visible are slightly reduced, compared to $La_{0.984}Nd_{0.008}Tm_{0.008}PO_4$. For the Tm^{3+} emission lines, most of the transitions below 675 nm reduce in intensity, where especially the transitions originating from $^1D_2$ reduce in intensity, which could be due to increased cross-relaxation in Tm^{3+} or to increased energy transfer to Nd^{3+}, as the Tm^{3+} ($^1D_2$) level is at approximately the same energy as the Nd^{3+} ($^4D_{3/2}$) level with respect to their ground states.

Of course, the CL spectra discussed above are only average CL spectra. Therefore, SEM-CL-EDX mapping was used to probe the distribution of both dopant ions on the submicron scale, where for every pixel the full emission spectrum was recorded in the range from 400 to 920 nm. To assess the doping homogeneity, the barycenter emission wavelength λ_{bc}

$$\lambda_{bc} = \frac{\int_{400nm}^{910nm} I(\lambda)\lambda\,d\lambda}{\int_{400nm}^{910nm} I(\lambda)\,d\lambda} \qquad (1)$$

was calculated for the measured spectral window (Fig. 4). Given that the value of λ_{bc} changes from 542 nm for $La_{0.995}Tm_{0.005}PO_4$ to 694 nm $La_{0.995}Nd_{0.005}PO_4$, any change in the relative contribution by both dopants to the total emission spectrum will readily be reflected. This approach is valid as for the studied concentrations the concentration quenching is limited, as well as the energy transfer between the dopant ions. For instance, the barycenter wavelength increases only 10 nm when going from $La_{0.984}Nd_{0.008}Tm_{0.008}PO_4$, to $La_{0.968}Nd_{0.016}Tm_{0.016}PO_4$. The map
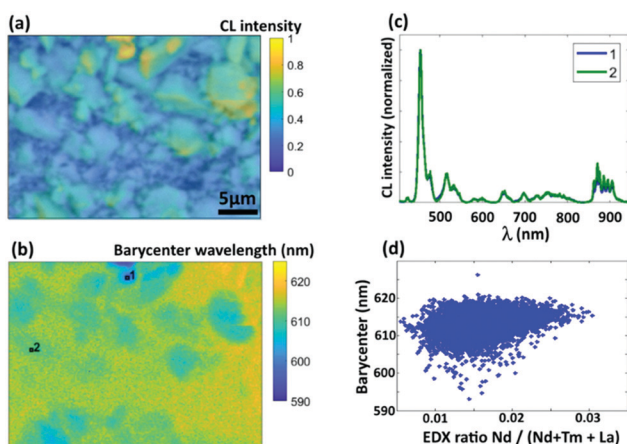
Fig. 4 (a) SEM image of $La_{0.968}Nd_{0.016}Tm_{0.016}PO_4$ obtained by the back-scattered electrons, with the color overlay showing the integrated CL intensity per pixel in the 256 × 192 sampled grid. (b) Barycenter wavelength. (c) Two local CL emission spectra as measured in the two pixels indicated in the barycenter map (b). (d) Scatter plot of the barycenter wavelength as function of the Nd EDX signal intensity, normalized to the lanthanide EDX signal intensity.

shows that the barycenter wavelength is narrowly distributed (Fig. 4b). For instance, no phosphor particles with dominating Tm^{3+} or Nd^{3+} emission were found. Apart from a few small particles with λ_{bc} in the range from 590 to 600 nm (spectrum 1 in Fig. 4c), for most measured points a λ_{bc} between 605 and 620 nm is found. Comparing the CL intensity and topography map in Fig. 4a with the λ_{bc} map in Fig. 4b, there appears a strong correlation between λ_{bc} and the CL intensity. Bigger and smoother particles, protruding from the sample surface, have slightly shorter barycenter wavelength. This is likely related to a lower fraction of reabsorption of emitted light or by a reduced optical path length due to limited scattering, in comparison to lower lying, smaller particles. Clearly, when considering only the bigger particles, the variation on the barycenter wavelength is no more than a few nm. For comparison, a scatter plot was made (Fig. 4d) where the relative EDX intensity of Nd compared to all lanthanides is plotted *versus* λ_{bc}. No clear trend can be found, although the Nd concentration appears to slightly increase for longer barycenter wavelengths, which is not unexpected based on the spectral positions of the Tm^{3+} and Nd^{3+} emission. The low EDX signal intensities for the Nd (and Tm) lines however introduce a great uncertainty and make this an unreliable metric to be used for dopant mapping, at least on this particular phosphor. In that sense the CL spectroscopy is far more sensitive and points at a very homogeneous distribution of both Tm and Nd dopants on the submicron length scale, given the sensitivity of this metric. Of course, it cannot make statements on the average Nd–Tm distance, which is about two orders of magnitude smaller than the spatial resolution of SEM-CL on these powder samples.

3. NMR: visibility function for paramagnetic co-doping of a diamagnetic host

For mono-doped systems, the NMR visibility $f(x)$ for homogeneous doping shows an exponential dependence $f(x) = \exp(-ar_0^3 x)$ on the doping concentration x, the number density parameter a and the radius of the blind sphere r_0. Heterogeneity causes a deviation from the homogeneous curve into the direction of complete phase segregation.[28] The curve for complete phase segregation can be estimated assuming a minimum blind sphere radius, which can be illustrated on the example of $LaPO_4$:Tm, *i.e.* $La_{1-x}Tm_xPO_4$. Given the mixture falls apart into $(1-x)$ $LaPO_4$ and x $TmPO_4$ and the NMR active nuclei in $TmPO_4$ are "invisible" because the blind sphere is covering them, then the maximum possible visibility $f_{max}(x)$ is approaching $f_{max}(x) = 1 - x$.[27]

The exponential visibility function for mono-doped systems was deduced in two different ways for a homogeneous doping scenario. We derived it by an inductive argument, *i.e.* a Taylor expansion for the low-doping regime which allowed to parameterize a decaying exponential function and a numerical verification on discrete, crystalline, statistically doped structures[27] by counting the numbers of atoms in- and outside the blind-spheres, which also allows to qualify when the assumption of a constant dopant number density is not valid anymore. Griffin and coworkers (ref. 33, Supp. Info. p. S10), independently derived it by an elegant probabilistic ansatz.[42] In the latter the idea is to calculate the probability for not finding a small voxel inside any blind-sphere

822 | *Phys. Chem. Chem. Phys.*, 2020, **22**, 818–825

This journal is © the Owner Societies 2020

in a given volume V, where the number density n is the number density of blind spheres. In a given volume V in total $N = nV$ blind spheres are introduced.

$$p_{\text{visible}} = \lim_{N \to \infty} \left(1 - \frac{V_{\text{blind}}}{V}\right)^N = \lim_{N \to \infty} \left(1 - \frac{n \cdot V_{\text{blind}}}{N}\right)^N \tag{2}$$
$$= \exp(-n \cdot V_{\text{blind}})$$

A typical case where this approximation breaks down is when the blind sphere radii become equal or shorter than the smallest possible distance between the detected NMR nucleus and the paramagnetic center.

It is straightforward to extend this approach to a homogeneous co-doping situation with the dopants Q and P.

$$p_{\text{visible}} = \lim_{N_P \to \infty, N_Q \to \infty} \left(1 - \frac{V_{\text{blind}}^P}{V}\right)^{N_P} \cdot \left(1 - \frac{V_{\text{blind}}^Q}{V}\right)^{N_Q} \tag{3}$$
$$= \exp\left(-n_P \cdot V_{\text{blind}}^P - n_Q \cdot V_{\text{blind}}^Q\right)$$

By expressing the blind sphere volume V_{blind} with the blind sphere radius r the visibility function $f(x,y)$ of a co-doped material like $La_{1-x-y}Gd_xDy_yPO_4$ can be written as

$$f(x,y) = \exp(-ar_1^3 x)\exp(-ar_2^3 y) \tag{4}$$

where r_1 and r_2 are the blind sphere radii of the two dopants respectively, and a is a parameter related to the number N_{UC} of dopable sites in the volume V_{UC} of the unit cell equal to the case of the mono-doped system.

$$a = 4/3\pi N_{\text{UC}}/V_{\text{UC}} \tag{5}$$

4. Validation of the NMR visibility function for a co-doping scenario

In the next step this model is to be tested experimentally. For this purpose three co-doped sample series have been prepared: $La_{1-x-y}Gd_xDy_yPO_4$, $La_{1-x-y}Nd_xTm_yPO_4$, and $La_{1-x-y}Nd_xHo_yPO_4$. Given the approximation works it should be possible to predict the 3D visibility function $f(x,y)$ from the blind-sphere radii of Gd(III), Dy(III), Nd(III), Tm(III), Ho(III) obtained from mono-doped systems for the homogeneous case, which in a previous study[26] were estimated to be 13.5, 12.5, 5.5, 9.0 and 10.5 Å, respectively.

The co-doping systems were chosen for three different reasons: first luminescence should be feasible to have another method to disprove homogeneity (see above), second the blind-spheres should have a different origin, *i.e.* relaxation based quenching of the NMR signal leading to homogeneous broadening, as in the case of Gd(III) and inhomogeneous line-broadening as in the case of Nd(III), Dy(III), Tm(III) and Ho(III),[26] and third the radii should differ in size.

To ease the visualization of the NMR visibility $f(x,y)$ the doping concentration of both dopants was increased by an equal amount.

$$f(x) = \exp(-ar_1^3 x)\exp(-ar_2^3 x) = \exp[-a(r_1^3 + r_2^3)x] \tag{6}$$

The NMR visibility can then be shown in a 2D plot. For $La_{1-2x}Gd_xDy_xPO_4$ (Fig. 5) and $La_{1-2x}Nd_xTm_xPO_4$ (Fig. 6) good
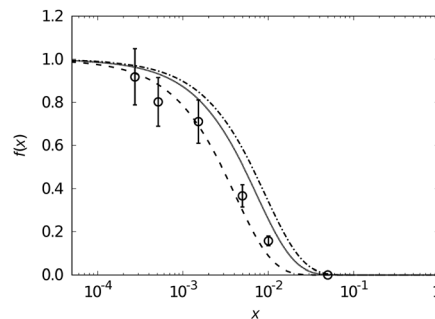
Fig. 5 NMR visibility $f(x)$ (circles with error bars) calculated from ³¹P MAS NMR data plotted against the doping concentration x of $La_{1-2x}Gd_xDy_xPO_4$ on a logarithmic scale. The dashed line features the expected visibility function $f(x) = \exp[-ax(r_{Gd}^3 + r_{Dy}^3)]$ with the values $a = 0.055$ Å^{-3}, $r_{Gd} = 13.5$ Å and $r_{Dy} = 12.5$ Å being the same as for mono-doped LaPO$_4$. The dotted and the dashdotted lines correspond to the $f(x)$ function neglecting Dy and Gd contribution, respectively, *i.e.* $f(x) = \exp(-ar_{Gd}^3 x)$ and $f(x) = \exp(-ar_{Dy}^3 x)$.
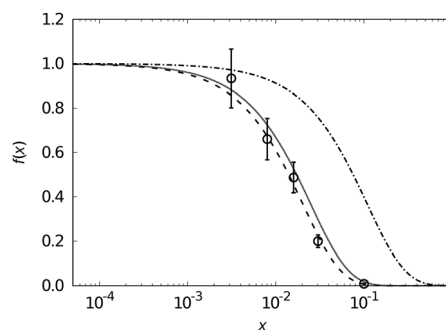
Fig. 6 NMR visibility $f(x)$ (circles with error bars) calculated from ³¹P MAS NMR data plotted against the doping concentration x of $La_{1-2x}Nd_xTm_xPO_4$ on a logarithmic scale. The dashed line features the expected visibility function $f(x) = \exp[-ax(r_{Nd}^3 + r_{Tm}^3)]$ with the values $a = 0.055$ Å^{-3}, $r_{Nd} = 5.5$ Å and $r_{Tm} = 9$ Å being the same as for mono-doped LaPO$_4$. The dotted and the dashdotted lines correspond to the $f(x)$ function neglecting Nd and Tm contribution, respectively, *i.e.* $f(x) = \exp(-ar_{Tm}^3 x)$ and $f(x) = \exp(-ar_{Nd}^3 x)$.

agreement between experimental data and the curve expected from the blind sphere radii obtained from mono-doped systems is observed, which indicates that the dopants are randomly distributed in the host onto the dopable sites.

A point which can be learned from the NMR visibility function $f(x,y)$ is that the sensitivity towards the doping concentrations x and y are scaled by the cubic radius of the corresponding dopants, which means that in case of a significant difference in radius like for Nd(III) and Tm(III) the bigger ion will dominate the visibility curve.

For this reason it makes sense to also test the visibility function $f(x,y)$ without imposing a linear dependence of x and y. Such a 3D plot, the "NMR visibility map", is shown for $La_{1-x-y}Nd_xHo_yPO_4$ in Fig. 7, where the contour-levels have be chosen according to the expected value for $f(x,y)$ at the point (x,y). Again the experimental data showed good agreement with the assumed model. For the $La_{1-x-y}Gd_xDy_yPO_4$ and $La_{1-x-y}Nd_xTm_yPO_4$ series they are shown in the ESI† (Fig. S4 and S5).

This journal is © the Owner Societies 2020

Phys. Chem. Chem. Phys., 2020, **22**, 818–825 | **823**
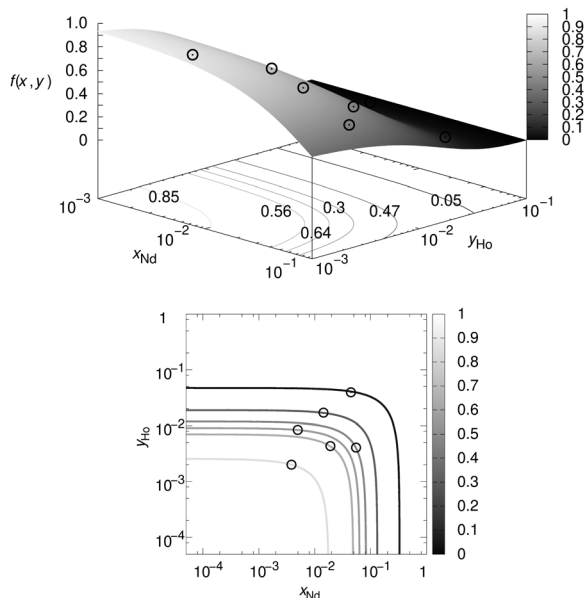
Fig. 7 NMR visibility map $f(x,y)$ calculated from ^{31}P MAS NMR data plotted against the substitution degree x and y in $La_{1-x-y}Nd_xHo_yPO_4$ on a logarithmic scale. The dashed 3D plot (upper) and its contour plot (lower) feature the expected visibility function $f(x,y) = \exp[-a(r_{Nd}^3 x + r_{Ho}^3 y)]$ with the values $a = 0.055$ Å^{-3}, $r_{Nd} = 5.5$ Å and $r_{Ho} = 10.5$ Å being the same as for mono-doped $LaPO_4$. The contour levels were chosen according to the expected value for $f(x,y)$ at the point (x,y).

Which advantages and disadvantages does the NMR visibility approach have in comparison to other techniques?

An advantage is that the NMR visibility tests doping homogeneity on a length scale which is of the same order of magnitude as the critical energy transfer distance, which indicates it could have relevance to applications in luminescence.

The NMR visibility function is not directly sensitive to the distribution of the two co-dopants relative to each other on the other hand. For two co-dopants with similar blind-sphere radius, it is possible that the NMR visibility of a system where the co-dopants do not mix, looks the same as a homogeneously co-doped system. The proposed formula provides a simple criterion to test doping homogeneity in co-doped systems, nevertheless.

Conclusions

Doping homogeneity has been evaluated from Å to μm scales by a combination of different techniques: solid-state NMR, EDX and SEM-CL. $LaPO_4$ doped with Tm^{3+} and/or Nd^{3+} was studied as a model system. For the co-doped samples, the doping homogeneity was very high at the submicron scale, as witnessed by the almost invariable emission spectrum over the evaluated sample area. It could be shown that the NMR visibility function can be predicted in case of homogeneous doping for co-doped systems given that the blind-sphere radii do not influence each other. This approximation seems to be valid in case of lanthanide dopants Ln(III). The NMR visibility

function may thus be used to study doping homogeneity in co-doped systems to achieve higher light yields. The study shows that it is often necessary to apply different techniques to study doping homogeneity: bulk techniques like NMR have the advantage that a deviation from an expected ideal curve can be qualified in a simple number, while microscopic techniques with local resolution power may give qualitative evidence for heterogeneous distributions of dopants.

Conflicts of interest

There are no conflicts to declare.

References

1 J. Zhang, K. Tse, M. Wong, Y. Zhang and J. Zhu, A brief review of co-doping, *Front. Phys.*, 2016, **11**, 117405.

2 H. Kanno, Y. Hamada and H. Takahashi, Development of OLED with high stability and luminance efficiency by co-doping methods for full color displays, *IEEE J. Sel. Top. Quantum Electron.*, 2004, **10**, 30–36.

3 H. S. Jang, W. B. Im, D. C. Lee, D. Y. Jeon and S. S. Kim, Enhancement of red spectral emission intensity of $Y_3Al_5O_{12}$:Ce^{3+} phosphor *via* Pr co-doping and Tb substitution for the application to white LEDs, *J. Lumin.*, 2007, **126**, 371–377.

4 K. Arai, H. Namikawa, K. Kumata, T. Honda, Y. Ishii and T. Handa, Aluminum or phosphorus co-doping effects on the fluorescence and structural properties of neodymium-doped silica glass, *J. Appl. Phys.*, 1986, **59**, 3430–3436.

5 G. Blasse, Energy transfer in oxidic phosphors, *Phys. Lett. A*, 1968, **28**, 444–445.

6 G. Blasse and B. C. Grabmaier, *Luminescent Materials*, Springer-Verlag, Berlin Heidelberg, 1994.

7 K. Van den Eeckhout, P. F. Smet and D. Poelman, Persistent Luminescence in Eu^{2+}-Doped Compounds: A Review, *Materials*, 2010, **3**, 2536–2566.

8 P. F. Smet, K. Van den Eeckhout, O. Q. De Clercq and D. Poelman, Persistent Phosphors, *Handbook on the Physics and Chemistry of Rare Earths, including Actinides*, Elsevier, 2015, ch. 274, vol. 48, pp. 1–108.

9 W. Horwitz, Nomenclature for sampling in analytical chemistry (Recommendations 1990), *Pure Appl. Chem.*, 1990, **62**, 1193–1208.

10 L. Vegard, Die Konstitution der Mischkristalle und die Raumfüllung der Atome, *Z. Phys.*, 1921, **5**, 17–26.

11 S. J. L. Billinge, Th. Proffen, V. Petkov, J. L. Sarrao and S. Kycia, Evidence for charge localization in the ferromagnetic phase of $La_{1-x}Ca_xMnO_3$ from high real-space-resolution x-ray diffraction, *Phys. Rev. B: Condens. Matter Mater. Phys.*, 2000, **62**, 1203–1211.

12 T. Susi, T. Pichler and P. Ayala, X-ray photoelectron spectroscopy of graphitic carbon nanomaterials doped with heteroatoms, *Beilstein J. Nanotechnol.*, 2015, **6**, 177–192.

824 | *Phys. Chem. Chem. Phys.*, 2020, **22**, 818–825

This journal is © the Owner Societies 2020

13 F. Sidiroglou, A. Roberts and G. Baxter, Contributed Review: A review of the investigation of rare-earth dopant profiles in optical fibers, *Rev. Sci. Instrum.*, 2016, **87**, 041501.

14 G. Servanton, R. Pantel, M. Juhel and F. Bertin, Two-dimensional quantitative mapping of arsenic in nanometer-scale silicon devices using STEM EELS–EDX spectroscopy, *Micron*, 2009, **40**, 543–551.

15 K. Van den Eeckhout, P. F. Smet and D. Poelman, Persistent luminescence in rare-earth codoped $Ca_2Si_5N_8$:Eu^{2+}, *J. Lumin.*, 2009, **129**, 1140–1143.

16 T. Coenen and N. M. Haegel, Cathodoluminescence for the 21st century: Learning more from light, *Appl. Phys. Rev.*, 2017, **4**, 031103.

17 D. Poelman and P. F. Smet, Time resolved microscopic cathodoluminescence spectroscopy for phosphor research, *Phys. B*, 2014, **439**, 35–40.

18 D. Ghica, I. D. Vlaicu, M. Stefan, V. A. Maraloiu, A. C. Joita and C. Ghica, Tailoring the Dopant Distribution in ZnO:Mn Nanocrystals, *Sci. Rep.*, 2019, **9**, 6894.

19 H. Deters, J. F. de Lima, C. J. Magon, A. S. S. de Camargo and H. Eckert, Structural models for yttrium aluminium borate laser glasses: NMR and EPR studies of the system $(Y_2O_3)_{0.2}$–$(Al_2O_3)_x$–$(B_2O_3)_{0.8-x}$, *Phys. Chem. Chem. Phys.*, 2011, **13**, 16071–16083.

20 N. Pathak, S. K. Gupta, P. S. Ghosh, A. Arya, V. Natarajan and R. M. Kadam, Probing local site environments and distribution of manganese in $SrZrO_3$:Mn; PL and EPR spectroscopy complimented by DFT calculations, *RSC Adv.*, 2015, **5**, 17501–17513.

21 T. Harazono, R. Adachi, N. Kijima and T. Watanabe, ^{89}Y MAS NMR in Red Phosphor, Eu-Doped Y_2O_2S. Assignment of Peaks Shifted by Paramagnetic Eu^{3+}, Spin Lattice Relaxation Time, and Eu Distribution, *Bull. Chem. Soc. Jpn.*, 1999, **72**, 2655–2664.

22 S. Maron, G. Dantelle, T. Gacoin and F. Devreux, NMR and ESR relaxation in Nd- and Gd-doped $LaPO_4$: towards the accurate determination of the doping concentration, *Phys. Chem. Chem. Phys.*, 2014, **16**, 18788–18798.

23 S. Maron, N. Ollier, T. Gacoin and G. Dantelle, Determination of paramagnetic concentrations inside a diamagnetic matrix using solid-state NMR, *Phys. Chem. Chem. Phys.*, 2017, **19**, 12175–12184.

24 T. Harazono, E. Yokota, H. Uchida and T. Watanabe, ^{89}Y-Static and MAS NMR, and ^{27}AlMAS NMR in Green Phosphor, Tb-Doped $Y_3Al_5O_{12}$ and Luminous Characteristics, *Bull. Chem. Soc. Jpn.*, 1998, **71**, 2797–2805.

25 T. Harazono, E. Yokota, H. Uchida and T. Watanabe, Luminous Characteristics and ^{89}Y-Static NMR in Red Phosphor, Eu-Doped Y_2O_3, *Bull. Chem. Soc. Jpn.*, 1998, **71**, 825–829.

26 W. Li, Q. Zhang, J. J. Joos, P. F. Smet and J. Schmedt auf der Günne, Blind spheres of paramagnetic dopants in solid state NMR, *Phys. Chem. Chem. Phys.*, 2019, **21**, 10185–10194.

27 W. Li, V. R. Celinski, J. Weber, N. Kunkel, H. Kohlmann and J. Schmedt auf der Günne, Homogeneity of doping with paramagnetic ions by NMR, *Phys. Chem. Chem. Phys.*, 2016, **18**, 9752–9757.

28 W. Li, M. Adlung, Q. Zhang, C. Wickleder and J. Schmedt auf der Günne, A guide to brighter phosphors – linking luminescence properties to doping homogeneity probed by NMR, *ChemPhysChem*, 2019, **20**, 3245–3250.

29 C. D'Agostino and P. Bräuer, Exploiting enhanced paramagnetic NMR relaxation for monitoring catalyst preparation using T_1–T_2 NMR correlation maps, *React. Chem. Eng.*, 2019, **4**, 268–272.

30 A. J. Pell, G. Pintacuda and C. P. Grey, Paramagnetic NMR in solution and the solid state, *Prog. Nucl. Magn. Reson. Spectrosc.*, 2019, **111**, 1–271.

31 I. Bertini, C. Luchinat, G. Parigi and E. Ravera, *NMR of Paramagnetic Molecules*, 2nd edn, Elsevier, Boston, 2017.

32 H. Lueken, *Magnetochemie*, ed. B. G. Teubner, Stuttgart/Leipzig, 1999.

33 B. Corzilius, L. B. Andreas, A. A. Smith, Q. Z. Ni and R. G. Griffin, Paramagnet induced signal quenching in MAS–DNP experiments in frozen homogeneous solutions, *J. Magn. Reson.*, 2014, **240**, 113–123.

34 D. Jardón-Álvarez and J. Schmedt auf der Günne, Reduction of the temperature gradients in laser assisted high temperature MAS NMR, *Solid State Nucl. Magn. Reson.*, 2018, **94**, 26–30.

35 Y. Ni, J. M. Hughes and A. N. Mariano, Crystal chemistry of the monazite and xenotime structures, *Am. Mineral.*, 1995, **80**, 21–26.

36 C. Penot, E. Champion and P. Goursat, Synthesis and Characterisation of Lanthanum Phosphate Powders, *Phosphorus Res. Bull.*, 1999, **10**, 307–312.

37 N. Clavier, R. Podor and N. Dacheux, Crystal chemistry of the monazite structure, *J. Eur. Ceram. Soc.*, 2011, **31**, 941–976.

38 D. Drouin, A. R. Couture, D. Joly, X. Tastet, V. Aimez and R. Gauvin, CASINO V2.42—A Fast and Easy-to-use Modeling Tool for Scanning Electron Microscopy and Microanalysis Users, *Scanning*, 2007, **29**, 92–101.

39 H. Demers, N. Poirier-Demers, A. R. Couture, D. Joly, M. Guilmain, N. de Jonge and D. Drouin, Three-dimensional electron microscopy simulation with the CASINO Monte Carlo software, *Scanning*, 2011, **33**, 135–146.

40 M. F. Joubert, B. Jacquier, C. Linares and R. M. Macfarlane, Relaxation of the high lying states and coordination numbers of Nd^{3+} ions in fluorides, *J. Lumin.*, 1992, **53**, 477–482.

41 M. Quintanilla, N. O. Núñez, E. Cantelar, M. Ocaña and F. Cussó, Tuning from blue to magenta the up-converted emissions of YF_3:Tm^{3+}/Yb^{3+} nanocrystals, *Nanoscale*, 2011, **3**, 1046–1052.

42 H. L. Weissberg, Effective Diffusion Coefficient in Porous Media, *J. Appl. Phys.*, 1963, **34**, 2636–2639.

This journal is © the Owner Societies 2020

Phys. Chem. Chem. Phys., 2020, **22**, 818–825 | 825

Doping Homogeneity in Co-doped Materials Investigated at Different Length Scales

Wenyu Li, [a] Philippe F. Smet, [*b] Lisa I.D.J. Martin, [b] Christian Pritzel [c] and Jörn Schmedt auf der Günne [*a]

[a] Inorganic Materials Chemistry, University of Siegen, Adolf-Reichwein-Str. 2, 57076 Siegen, Germany.
[b] Department of Solid State Sciences, Ghent University, Krijgslaan 281-S1, 9000 Gent, Belgium.
[c] Construction and Materials Chemistry, University of Siegen, Paul-Bonatz-Str. 9-11, 57076 Siegen, Germany.
*Corresponding authors:
Jörn Schmedt auf der Günne gunnej@chemie.uni-siegen.de,
Philippe F. Smet Philippe.Smet@UGent.be

Supporting information
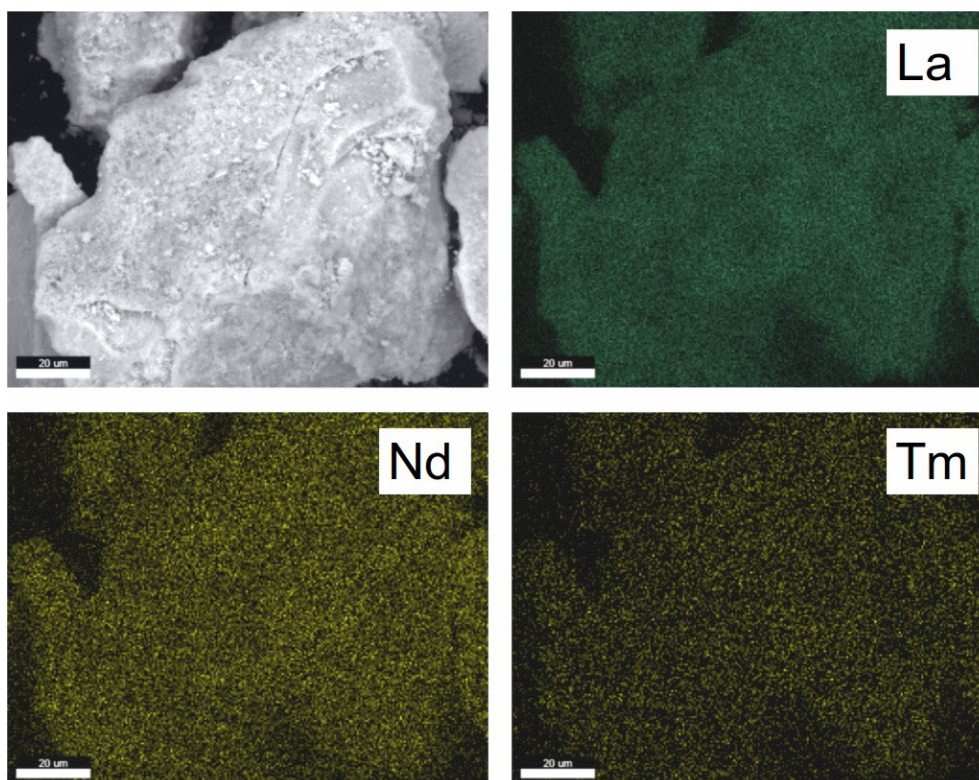
1. EDX mappings

Figure S1: Electron micrographs detected via backscattered electrons (top left) and EDX mappings (top right and bottom) of $La_{0.94}Nd_{0.03}Tm_{0.03}PO_4$. The acceleration voltage is 30 kV.
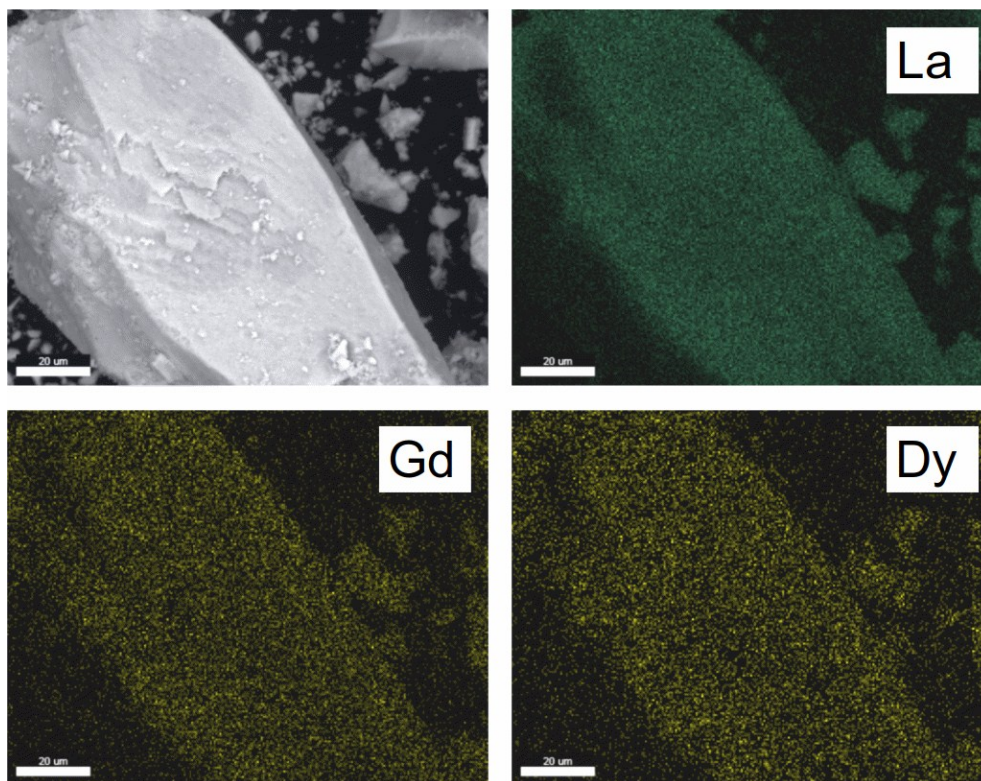
Figure S2: Electron micrographs detected via backscattered electrons (top left) and EDX mappings (top right and bottom) of $La_{0.9}Gd_{0.05}Dy_{0.05}PO_4$. The acceleration voltage is 30 kV.
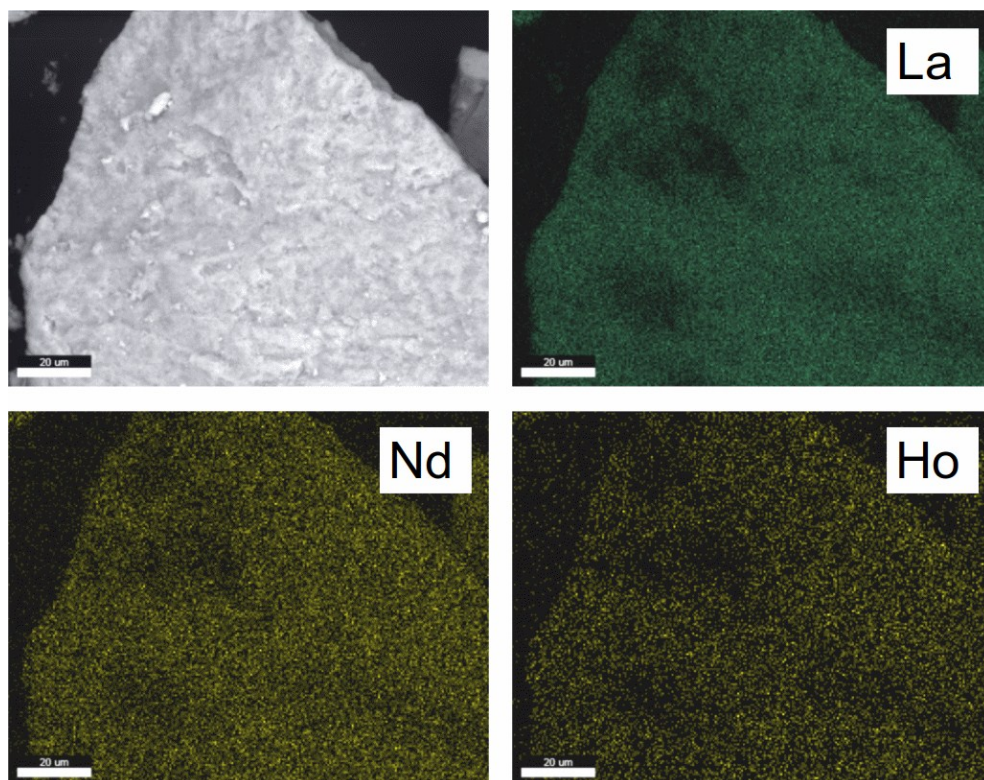
Figure S3: Electron micrographs detected via backscattered electrons (top left) and EDX mappings (top right and bottom) of $La_{0.92}Nd_{0.04}Ho_{0.04}PO_4$. The acceleration voltage is 30 kV.

2. NMR visibility maps
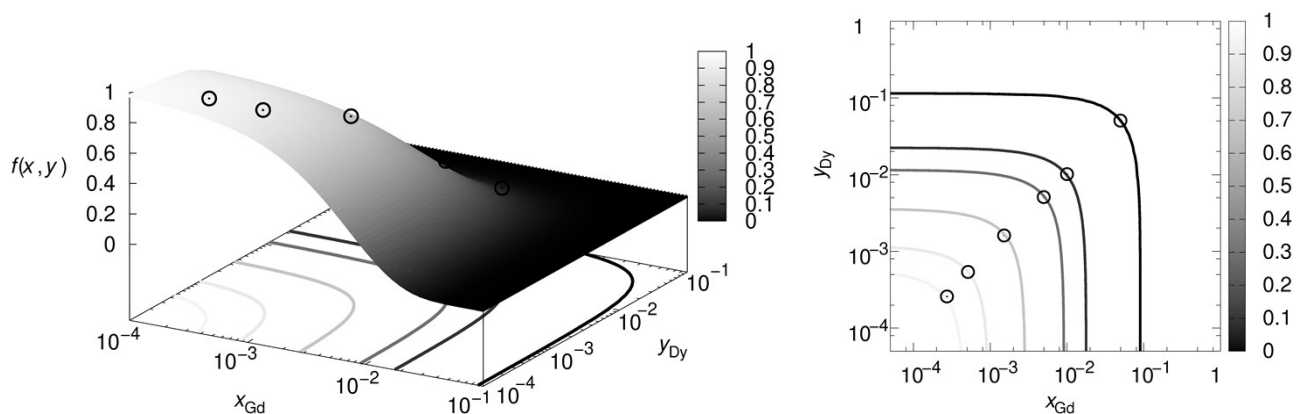
Figure S4: the NMR visibility map calculated from ^{31}P MAS NMR data plotted against the substitution degree x and y in $La_{1-x-y}Gd_xDy_yPO_4$ on a logarithmic scale. The dashed 3D plot (left) and its contour plot (right) feature the expected visibility function $f(x,y) = \exp[-a(r_{Gd}^3x+r_{Dy}^3y)]$ with the values $a = 0.055/Å^3$, $r_{Gd} = 13.5$ Å and $r_{Dy} = 12.5$ Å being the same as for mono-doped LaPO4. The contour levels were chosen according to the expected value for $f(x,y)$ at the point (x,y).
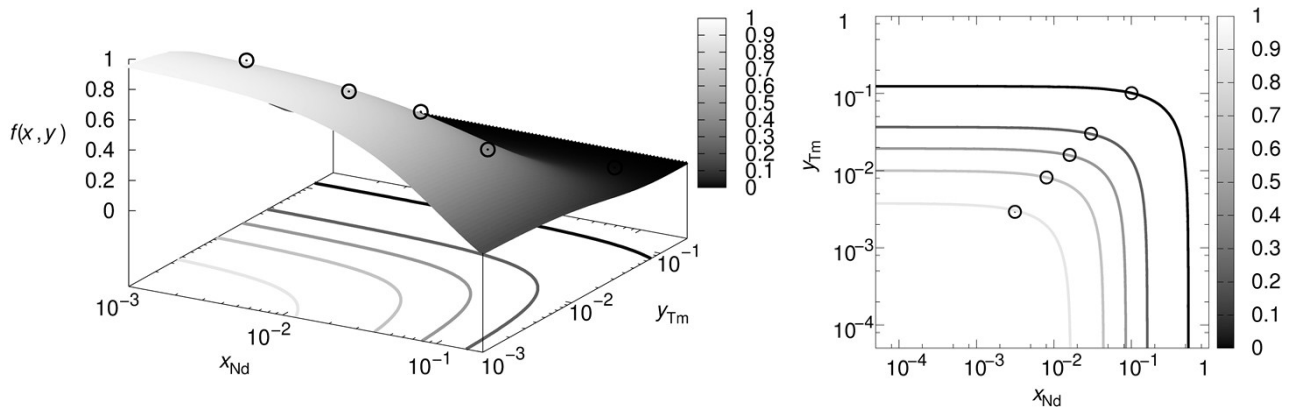
Figure S5: the NMR visibility map calculated from ^{31}P MAS NMR data plotted against the substitution degree x and y in La$_{1-x-y}$Nd$_x$Tm$_y$PO$_4$ on a logarithmic scale. The dashed 3D plot (left) and its contour plot (right) feature the expected visibility function $f(x,y) = \exp[-a(r_{Nd}^3 x + r_{Tm}^3 y)]$ with $a = 0.055/\text{Å}^3$, $r_{Nd} = 5.5$ Å and $r_{Tm} = 9$ Å being the same as for mono-doped LaPO4. The contour levels were chosen according to the expected value for $f(x,y)$ at the point (x,y).

4 Summary of Articles

The aim of this chapter is to organize and make connections between the series of articles, which shared the same research interest. A main question was raised at the beginning of this work: was it possible to determine doping homogeneity based on only simple measurements of NMR peak areas? The question was answered in this cumulative thesis by the establishment of the "NMR visibility" method and the resulting "NMR homogeneity". The stepwise attempt at this problem was explained in the following subsections, which also acted as a summary of the manuscripts presented in the chapter 3.

4.1 Summary of the NMR Visibility Method

In section 3.1, the first trial of the idea of "NMR visibility" was presented and the "NMR visibility function" $f(x) = \exp(-ar_0^3 x)$ was developed, which laid the foundation of this work. The NMR visibility $f(x)$ was defined as the molar peak area of the doped sample normalized by that of the non-doped host, which was a function of doping fraction x. It is a dimensionless quantity ranging from 0 to 1. The parameter a in the visibility function is the number density parameter related to the host structure and the r_0 is the radius of the blind sphere. Such visibility function was able to determine the doping homogeneity for XRD homogeneous sample series $Sr_{1-x}Eu_xH_2$. However, at this step it was unclear whether the visibility function could be used as a general solution to determine doping homogeneity.

In section 3.2, the visibility function $f(x) = \exp(-ar_0^3 x)$ was tested on different sample series, including $Sr_{1-x}Eu_xGa_2S_4$, $(Zn_{1-x}Mn_x)_3(PO_4)_2 \cdot 4H_2O$ and $La_{1-x}Ln_xPO_4$ (Ln = Nd, Sm, Gd, Dy, Ho, Er, Tm, Yb). For all sample series, doping homogeneity could be determined, as the NMR visibility decayed exponentially like the visibility function. The radii r_0 of blind spheres were extracted for all paramagnetic dopants based on the visibility function. The exception case was $La_{1-x}Sm_xPO_4$, for which NMR visibility $f(x)$ stayed around 100% despite the increasing doping level x. As a result, the r_0 of Sm(III) was refined within the

shortest La to P distance (about 3 Å), but the numerical value was not clear from NMR visibility function. To solve this problem, an alternative method was developed, which was based on the second moment analysis of the ^{31}P MAS NMR spectra of $La_{1-x}Sm_xPO_4$. Taking the probe head dead time delay into consideration, the second moment could be treated as a function which linearly dependent on the doping level x. The blind sphere radius of Sm(III) calculated from such method was 0.45 Å, which was as expected within the shortest La to P distance (about 3 Å). However, the radii obtained from the two methods were not comparable because the later method assumed that the line shape should be perfect Gaussian, which in reality is hardly the case for paramagnetic doped samples especially in high doping level. In section 3.2, the linear dependence equation of second moment or linewidth on doping level x was developed for Gaussian and Lorentzian lineshapes, respectively. The open question was that whether a linewidth relation to doping level could be developed for a more general lineshape for example Voigt lineshape. The correlations of blind sphere radii to the gyromagnetic ratio and effective magnetic moment were consistent with the dipolar part of the Solomon–Bloembergen–Morgan relaxation model. Unexpectedly, the blind sphere radii also showed correlation with the pseudo-contact shift when comparing with reduced coupling constants, although in the NMR spectra no significant shifts were observed for all $La_{1-x}Ln_xPO_4$ except $La_{1-x}Sm_xPO_4$. It was shown that both relaxation and pseudo-contact shift gave an explanation to the origins of blind spheres.

In section 3.3, it was shown that the NMR visibility $f(x)$ as a function of doping level x behaved differently for homogeneously and inhomogeneously doped samples. Only the $f(x)$ of homogeneously doped samples showed consistency with the exponential visibility function $f(x)=\exp(-ar_0^3x)$ and decayed to a small value close to zero (signal invisible in NMR spectra) at high doping level. For the inhomogeneously doped samples, even at high doping level there could be visible signals and $f(x)$ decayed to reach a plateau at a nonzero value, which varied for individual sample series. A schematic presentation is shown in the figure 4.1-1.
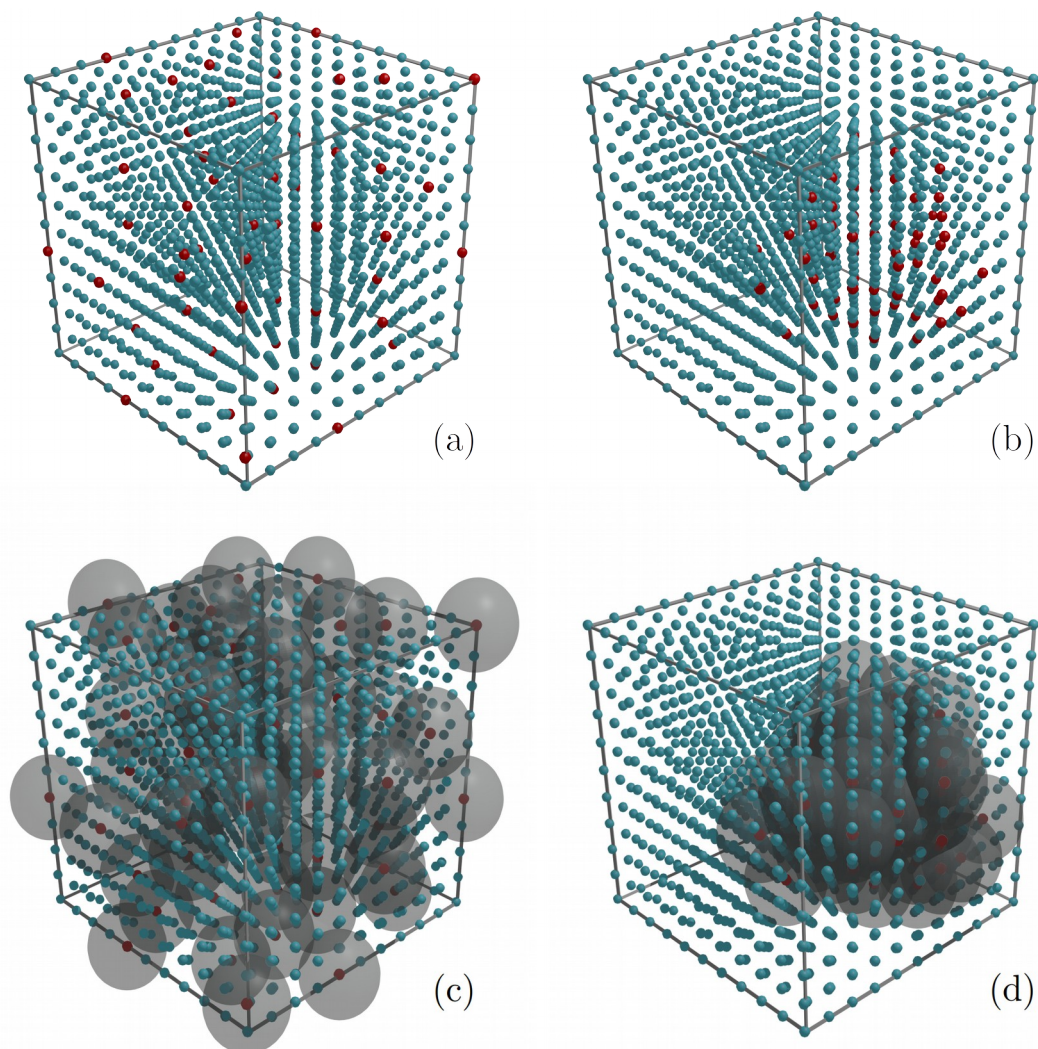
Figure 4.1-1 Schematic sketch of homogeneous (a) and heterogeneous (b) doping scenarios. The small blue and red spheres represent host and dopant atoms, for example La and Ln (Ln = Nd, Gd, Dy, Ho, Er, Tm, Yb), respectively. The large gray spheres (c,d) are the NMR blind spheres which are around the paramagnetic dopants. At the same doping level, more volume fraction, which means more NMR nuclei, is covered by the blind spheres for the homogeneous case (c) as compared to the heterogeneous case (d). Thus, less NMR signal is expected to be observed for homogeneous samples, which means smaller NMR visibility. At high doping level, for homogeneously doped sample (c) the NMR visibility decayed to a small value close to zero (signal invisible in NMR spectra) because the whole volume could almost be covered by the blind spheres. For the heterogeneously doped sample (d), the NMR nuclei in the uncovered volume are not or less affected by the paramagnetic effects, thus contribute to the residue signal even at a high doping level.

The advantage of such NMR visibility method was that the length scale on which the NMR homogeneity was checked is of the same order of magnitude as the critical energy transfer distance, indicating a relevance to the applications in luminescence. To test whether the NMR determined homogeneity agreed with the material performance, quantitative excitation and emission spectra and decay

timed have been measured for the two $La_{1-x}Ln_xPO_4$ series. The results showed that the samples with higher NMR homogeneity demonstrated better performance regarding decay time as well as excitation and emission intensity.

In section 3.4, a 3D visibility map was developed based on the extended version of the NMR visibility function $f(x,y)=\exp(-ar_1^3 x)\exp(-ar_2^3 y)$ for the co-doped systems. The model compounds were co-doped sample series $La_{1-x-y}Gd_xDy_yPO_4$, $La_{1-x-y}Nd_xTm_yPO_4$ and $La_{1-x-y}Nd_xHo_yPO_4$, which were homogeneously doped according to the EDX mapping and the SEM-CL results. The consistency of the measured NMR visibility with the predicted visibility map indicated that the above method was not only applicable for systems with single dopant species but also for co-doped systems. However, the application of such method was to detect heterogeneity rather than to confirm homogeneity. The reason is that the NMR visibility function is not directly sensitive to the distribution of the two co-dopants relative to each other. In addition, for two co-dopants with similar blind sphere radii, it is possible that the NMR visibility of a system where the co-dopants do not mix, looks the same as a homogeneously co-doped system. Together with SEM-EDX mapping and SEM-CL techniques, it was shown that co-doping homogeneity or heterogeneity can be systematically studied from μm to nm range.

Overall, the main question raised in the introduction section, i.e. whether the doping homogeneity that correlated to the material performance can be determined by a peak area related novel NMR methodology, was answered.

4.2 A Short Comment on NMR Homogeneity

In this thesis, a novel NMR methodology for doping homogeneity analysis has been established with the ideas of the NMR visibility, NMR visibility function and the NMR homogeneity. The NMR visibility made use of the visible signal (peak area) as well as the lost signals inside blind spheres, while the NMR visibility function provides the possibility to extract numerical values of blind sphere radii. The homogeneous and heterogeneous doping scenarios can be

differentiated by the NMR visibility method. The samples that were determined to be homogeneous by this method possess higher NMR homogeneity on the length scale of Å to nm range, which was consistent with better luminescence properties. Such method has been shown to be applicable in single dopant systems as well as co-doped ones.

The concept of "NMR homogeneity" used in this thesis specifically referred to the doping homogeneity determined by the NMR visibility method, which is not to be confused with NMR lab slang, for example magnetic field or frequency homogeneity in NMR. In addition, it is also different from homogeneous or inhomogeneous line broadening in the section 3.2.

As introduced in the chapter 1, the IUPAC definition of "homogeneity"[29] ("the degree to which a property or a constituent is uniformly distributed throughout a quantity of material") reveals the importance of clarifying specific length or volume scale while making the statement of homogeneity or heterogeneity.

Because the concept of "NMR homogeneity" was based on the NMR visibility method, the length scale that relates to "NMR homogeneity" can be narrowed to the radius of the blind sphere of the paramagnetic dopant involved, which is Å to nm. The NMR visibility which relates to the visible peak area change as a function of doping level can also provide inside into dopant distribution, as the consistency or inconsistency with the NMR visibility function indicates the doping is homogeneous or heterogeneous, respectively. The formula of the visibility function has also been independently derived by Griffin and coworkers (reference [61], SI). It should be made clear that the "NMR homogeneous" specifically refers to a random distribution of dopants. In addition, as pointed out in the section 3.4, for co-doped systems, the NMR visibility method is not a method to "prove" homogeneity. Instead, it acts as a tool that could disprove heterogeneity on the Å to nm length scale. This is because if two co-dopants share a similar blind sphere radius, it is possible that the NMR visibility looks the same for a homogeneously co-doped system and a system in which the co-dopants do not mix. Another potential problem of applying the NMR visibility

method could be triggered when the blind sphere is very small. In this case the visibility method might not be applicable due to the absence of the visibility variation. An example was presented in section 3.2, as a small NMR blind sphere was observed for Sm(III). Therefore, besides the NMR visibility method, other methods such as diffraction, EDX and SEM-CL were also applied to confirm a homogeneous doping (section 3). Overall a comment on the NMR visibility method should be made: a technique may be remarkable to disprove doping heterogeneity on a certain length scale, but for the comprehensive study on different length and volume scales, a combination of different techniques is required.

5   Overall Discussions

In the previous chapters 3 and 4, the main question of the thesis was answered and the method was explained. This chapter of overall discussions aimed to highlight the potential contributions to the NMR blind sphere theory as well as to provide evidence for a reasonable interpretation of blind sphere radius. In the following subsections, first the main results about NMR blind spheres were presented, subsequently each result was compared with previous publications respectively, and finally the possible change of the NMR blind sphere radius upon magnetic field, temperature and MAS frequency, was speculated based on publications in related fields.

5.1 Main Results about NMR Blind Spheres

The visibility function developed in this thesis not only contributed to the homogeneity determination, but also to the aspect of the paramagnetic NMR theories, as the visibility function $f(x) = \exp(-a r_0^3 x)$ provided a general method to extract blind sphere radii in different systems for different paramagnetic dopants. The radii of Eu(II), Mn(II), Nd(III), Sm(III), Gd(III), Dy(III), Er(III), Ho(III), Tm(III) and Yb(III) have been determined (see table 5.1-1).

Table 5.1-1 Sum of the numerical values of the blind sphere radii r_0 values obtained from the NMR visibility method.

Dopants	NMR nuclei	Hosts	r_0 / Å
Eu(II)	^{1}H	SrH_2	17
Eu(II)	^{71}Ga	$SrGa_2S_4$	13
Mn(II)	^{1}H	$Zn_3(PO_4)_2 \cdot 4H_2O$	10
Mn(II)	^{31}P	$Zn_3(PO_4)_2 \cdot 4H_2O$	7
Nd(III)	^{31}P	$LaPO_4$	5.5
Gd(III)	^{31}P	$LaPO_4$	13.5
Dy(III)	^{31}P	$LaPO_4$	12.5
Ho(III)	^{31}P	$LaPO_4$	10.5
Er(III)	^{31}P	$LaPO_4$	10.0
Tm(III)	^{31}P	$LaPO_4$	9.0
Yb(III)	^{31}P	$LaPO_4$	5.8

It was shown that for the same paramagnetic dopant, the blind sphere radius related to the cubic root of gyromagnetic ratio of different NMR nuclei, and such conversion formula was also adoptable within error limit in different hosts. In addition, from the study of different Ln(III) dopants in the same host, it was shown that apart from relaxation, which was assumed in the past to be the major contribution to blind sphere, the pseudo-contact shielding is also empirically correlated with the size of the blind sphere for Ln(III) dopants except Gd(III). In particular, Sm(III) has a blind sphere so small that all signals are visible for $La_{1-x}Sm_xPO_4$ ($0 \leq x \leq 1$). In this case a supplementary method based on the analysis of second moment change as a function of doping level was developed and its mathematical basis was also validated. Such method is the first trial of applying second moment analysis on the study of doping homogeneity and blind sphere radii. It is also a good supplement to the visibility method when the signal loss is small or when the signal overlapping is severe. To the best of my knowledge, this is the first systematic publication on the blind sphere sizes in inorganic solids, which not only contributes to database of blind sphere radii, but also to the future study of the theory of blind sphere in paramagnetic NMR and potentially also in DNP. It may also provide a better estimation of the possibility that a sample is NMR visible or NMR blind (see section 3.2). In addition, a better estimation of the critical doping level at which a sample becomes NMR blind could also be made.

5.2 Main Results Compared with Previous Studies

A simple picture of blind sphere is typically depicted as figure 5.2-1, which is a spherical volume around a paramagnetic ion. The size of blind sphere depends on the gyromagnetic ratio of the observed NMR nuclei and on the paramagnetic species.[89] Additionally, in solution NMR r_0 increases with increasing molecular size.[89] The fundamental difference between the blind sphere size difference in solution and in solid state NMR is that in solids the molecular tumbling is abolished therefore the contribution from Curie spin relaxation is absent. Only in

special circumstances, for example in extremely anisotropic lanthanide complexes,[90,91] the magnetic susceptibility can be modulated by the small fluctuations of the coordination environment and the possibility of Curie spin relaxation can't be ruled out.[27] In such cases, the relaxation is no longer dependent on the molecular tumbling time but on the characteristic timescale of the distortion of the coordination environment.[27]
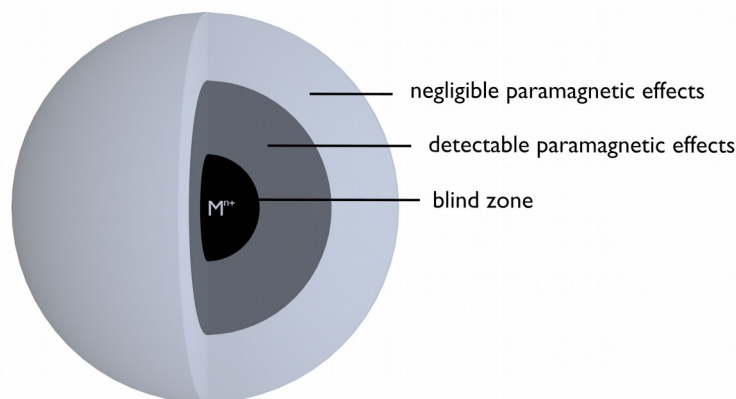
Figure 5.2-1 Schematic sketch of the blind zone,[58] which is typically treated as a spherical volume around a paramagnetic ion M^{n+}.

In this thesis, the observed dependence of blind sphere radius r_0 on gyromagnetic ratio γ as $r_0 \propto \sqrt[3]{\gamma}$ is consistent with previous studies.[89,92–94] In previous studies this dependence was explained as a result of dipolar PRE, which has a dependence on gyromagnetic ratio γ and distance r as $\gamma^2 r^{-6}$.[27,89,92–94] The $r_0 \propto \sqrt[3]{\gamma}$ relation was shown to be very useful for the choice of NMR nuclei in the structure solution of metalloproteins, as direct detection of low γ NMR nucleus for example ^{13}C or ^{15}N could provide more information on structure constrains in the proximity of the metal ion than proton NMR due to smaller blind sphere.[92,93]

A more detailed picture about NMR blind spheres around different metal ions is presented in the figure 5.2-2. The figure 5.2-2 also provides a closer look into the detectable paramagnetic effect region (figure 5.2-1), which points out the difference between metal ions that have isotropic (or near isotropic) magnetic susceptibility tensor such as Gd(III) and Mn(II), and metal ions that possess large anisotropic susceptibility such as Dy(III). This is consistent with the exchange spectroscopy (EXSY) data in the section 3.2. This detectable paramagnetic effect region is especially interesting for distance related structure

constrains such as the application in NMR crystallography,[89] whereas the information of blind sphere was only obtained as a piece of distance information that defines the lower limit of detectable region.

Nevertheless, in both descriptions (figure 5.2-1 and 5.2-2) the origin of blind sphere was assumed to be related to line broadening and specifically to T_2 relaxation. The longer the electron relaxation time, the larger the nuclear R_2 (equation 2.2.3-9 in section 2.2.3) and the more severe broadening of the NMR lines of the observed nuclei, and thus the size of the blind sphere should be bigger around the metal ion.
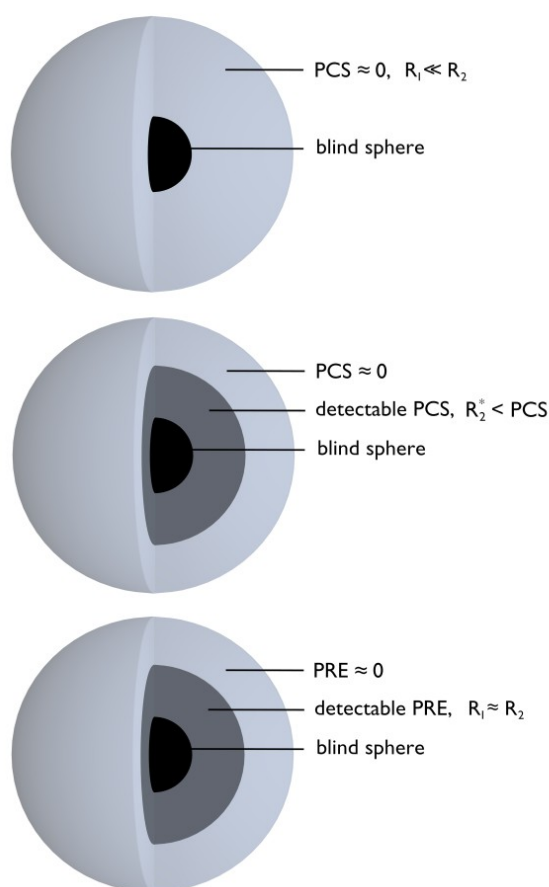
Figure 5.2-2 Schematic sketch of the effect of different paramagnetic centers on blind sphere, PCS and PRE. The three pictorial descriptions from the bottom to the top are related to three types of paramagnetic centers: radicals with $\tau_e >10$ ns and $\Delta\chi \approx 0$, metals with large $\Delta\chi$ (such as Co^{2+}, Tb^{3+}, Tm^{3+}, Dy^{3+}) and metals with large τ_e ($\tau_e <10$ ns) (such as Cu^{2+}, Mn^{2+}, Gd^{3+}), respectively.[89] The $\Delta\chi$ is the magnetic susceptibility anisotropy, τ_e is the electron relaxation time, R_1 and R_2 are the spin-lattice and spin-spin relaxation rates, respectively.

In section 3.2, the pseudo-contact shielding was also shown to be, though empirically, correlated with the size of the blind sphere for Ln(III) dopants except Gd(III). This triggered a second thought into the origin of blind sphere and the γ-dependence. Although the pseudocontact shift δ_{PCS} itself has no γ-dependence (but a distance dependence of r^{-3}), the pseudocontact interaction has a dependence of γr^{-3}. If the assumption in this thesis is true that an overall interaction strength is responsible for the boundary condition of blind sphere, then it is not likely (at least based on the current data) to distinguish the contribution form PRE or PCS simply from the gyromagnetic ratio dependence of blind sphere radius. In a word, the $r_0 \propto \sqrt[3]{\gamma}$ relation itself does not rule out the possibility of PCS contribution.

Indeed, it was pointed out in a study of superconductor that the NMR wipeout effect can result from "static effects" or "dynamic effects" or both.[95] For static origin, the signal loss was considered to be caused by a large spread of resonance frequencies out of a given spectral window,[95,96] which is consistent with the interpretation based on the EXSY data and inhomogeneous broadening in section 3.2. In the dynamic case, T_2 relaxation time becomes shorter than the dead time delay and thus signals from such nuclei becomes unobservable,[95,96] as was also described in section 3.2. A typical example for wipeout due to static effects is metal doped with non-magnetic impurity.[97] Wipeout effects due to dynamic reason were observed in studies[96] of canonical spin glass systems,[98] stripe-ordered cuprates,[99] doped lanthanum manganites[65] and so forth.

From the previously mentioned examples it can be seen that the application of blind sphere or wipeout effect is not just limited to the systems studied in this work, namely inorganic materials with paramagnetic dopants. In fact, it also finds applications in biochemistry studies especially metalloproteins[58,100,101] as well as in alloys and magnetic materials.[102–105]

In dilute alloys, a concept in analog to the blind sphere is the "wipeout number", which represents the neighboring host atoms affected sufficiently by the

impurity,[104] or in other words, the number of neighbors whose contribution to the intensity is made unobservable.[104] The wipeout number is defined as the difference between the number of host atoms in the alloy and the number of host atoms in a pure host metal required to give the same intensity of the resonance spectrum divided by the number of impurity atoms.[104,105] The measurement of wipeout numbers gives the size of quadrupole interactions and thus of the electric field gradient (EFG).[103,104]

In magnetic materials especially single molecule magnets and magnetic molecular rings or clusters, the dynamic effect induced wipeout effect was studied along with relaxation behavior and temperature dependence, because it could provide information about the spin dynamics.[96] The wipeout effect was shown to become more pronounced as the temperature decreases, which was explained by the simultaneous enhancement of the spin-spin relaxation.[68,96] A formula (equation 5.2-1) was provided based on the Redfield equation,[68,96] and by replacing the T_2 by the spectrometer dead time delay τ_d, the r_0 can be written as equation 5.2-2. The $\langle \delta B_z^2 \rangle$ is the longitudinal fluctuating field originating from a magnetic moment sitting at a distance r from the NMR nucleus. The δ symbol here indicates fluctuations and it is not to be confused with the chemical shift.

$$\frac{1}{T_2} = \gamma_I^2 \langle \delta B_z^2 \rangle \tau(T) = \frac{1}{r^6} \gamma_I^2 \langle \delta \mu_e^2 \rangle \tau(T) \qquad (5.2\text{-}1)$$

$$r_0 = \sqrt[6]{\tau_d \gamma_I^2 \langle \delta \mu_e^2 \rangle \tau(T)} \qquad (5.2\text{-}2)$$

Calculation of the blind sphere radius from equation 5.2-2 is nontrivial because the correlation time τ is not a constant but a function of temperature T. Nevertheless, such equation may shed light on the temperature dependence of wipeout effect. In the case studies of single molecule magnets,[68,96] the correlation time τ was shown to become longer as temperature decreased and as a result, the T_2 was shortened. When T_2 of some nuclear spins reached the τ_d, signals from those spins became undetectable by the spectrometer, which is the previously

mentioned wipeout effect by the dynamic reason. The gradual loss of signal intensity ceased until the T_2 of all nuclear spins in the sample became shorter than τ_d, which means no signal can be observed anymore. As a consequence, the wipeout effect was shown to be more pronounced at low temperatures than at high temperatures. Although without further studies it is unknown whether the same dependence could be observed in the paramagnetic doped samples as in the single molecule magnets, such dependence may still be inspiring for the future study of blind spheres in general and particularly, for the application in low temperature NMR.

The MAS frequency may also play a role in the size of blind sphere, as shown by a solid state ^{13}C NMR study of the Co^{II}-replaced catalytic domain of matrix metalloproteinase 12 (CoMMP-12) that the blind sphere around the Co^{II} at spinning frequency of 22 kHz is larger than and at 60 kHz.[100] The change of blind sphere size upon MAS frequency may also be traceable from DNP studies on the spinning-induced bleaching effect.[61,63] For a sample of glycerol : H_2O 1 : 1 (v : v) doped with TOTAPOL or TEMPOL,[*] the spinning-induced bleaching effect was more pronounced at higher spinning frequencies, while the same sample doped with $DyCl_3$ was not as sensitive to the change of spinning frequency in the range of 6 to 12 kHz, at 100 K and 9.4 T.[63] This is consistent with the observation in the NMR measurements of the samples in this thesis that at the spinning frequency range of 8 to 12.5 kHz no significant change of signal visibility can be detected. In addition, for radicals it was shown that the bleaching effect should be less severe at higher temperatures.[63,106] However, it should be pointed out that the conclusions drawn from the studies of spinning induced bleaching effect in DNP are not completely comparable with the blind sphere results in inorganic solid state NMR, because for DNP the role of microwave and the cross effect[61,63,107] for biradicals need to be taken into account in extra.

---

[*]TOTAPOL and TEMPOL are radical polarizing agents in DNP. TOTAPOL is a biradical 1-(TEMPO-4-oxy)-3-(TEMPO-4-amino)propan-2-ol. TEMPO is a stable nitroxyl radical 2,2,6,6-Tetramethyl-1-piperidinyloxy. TEMPOL is 4-hydroxy-TEMPO.

At this stage, based on the results in this thesis as well as the examples discussed so far, it is very convincing that the signal bleaching effect around paramagnetic centers can be observed in numerous paramagnetic systems and the signal intensity in general decays as the concentration of paramagnetic species increases. Surprisingly, however, in some special cases even at very high concentration of paramagnetic species the NMR signals can still be well observed, which almost conveys the impression that blind spheres are absent. In this thesis an example of $La_{1-x}Sm_xPO_4$ was presented in the section 3.2. Besides Sm(III), Ce(III) and Eu(III) were also shown to have small blind spheres in the ^{31}P MAS NMR study of $La_{1-x}Eu_xPO_4$[108] and the solution ^{13}C NMR study of cerium(III) metalloproteins,[92] respectively. These systems are potentially good candidates for the systematic studies of paramagnetic effects because signals can be observed in wide concentration window, and especially interesting for obtaining signal in the first coordination sphere of the metal ion.

In this work the systematic change of blind sphere radii for the lanthanide Ln(III) ions has been discussed. Despite the difference in absolute values due to difference in experimental conditions and choice of NMR nucleus, the trend in radii of Ln(III) that the radius descends in the order of "Gd(III) Dy(III) Tm(III) Yb(III) Nd(III)", is in good agreement with the prediction of blind sphere radii for solution ^{1}H NMR at 900 MHz proton Larmor frequency in the reference [27]. The difference in the blind sphere radii for different Ln(III) is comparably larger for the predicted ^{1}H NMR in reference [27] than for ^{31}P NMR in table 5.1-1, which could be partially attributed to γ-dependence.

In section 3.2 and in table 5.1-1, a conversion formula of blind sphere radii based on the γ-dependence was shown to be adoptable between different NMR nuclei as well as different hosts within error limit. For this comparison, it was assumed that the size of blind spheres for Eu(II) and Gd(III) is similar, as they are isoelectronic thus share similar electronic relaxation behavior. However, this assumption is not necessarily true for every system. For example, in solution the electronic relaxation times T_{1e} and T_{2e} of Eu(II) were shown to be longer compared to the T_{1e} and T_{2e} of Gd(III).[27,109,110] Such studies were mainly

performed in solution state as Eu(II) complexes are potential magnetic resonance imaging (MRI) contrast agent.[110–112] The situation could be different in solids, because in solution the water exchange kinetics should be considered in extra for auqa ions $[Eu(H_2O)_8]^{2+}$ and $[Gd(H_2O)_8]^{3+}$.[109] Overall, though similar electronic properties are usually assumed for isoelectronic ions[27] and the EPR spectra of Eu(II) and Gd(III) were similar in glass, ceramics and zeolites,[113] due to the difference in ionic radii[114] and ground state splittings,[115] whether the electron relaxation times are the same for Eu(II) and Gd(III) in solids and whether this assumption about blind sphere works for every host or at different temperatures pend for further research.

In table 5.2-1 and 5.2-2, brief summaries of published numerical values in solid state and solution NMR are provided, respectively. It can be seen from the summaries that size of blind sphere could be suppressed by detecting low γ nuclei instead of high γ ^1H, or by increasing spinning frequency especially by ultrafast MAS. Measurements at higher fields also tend to show smaller blind spheres, however, it is difficult to trace the cause down to one single reason, because measurements at higher magnetic field are usually accompanied by better hardware such as probes with shorter dead time or MAS unit with higher spinning possibility. Finally, it's worth pointing out that although the concept of blind sphere was developed originally in inorganic crystalline systems (section 5.3), the numerical values collected in such systems are rather limited, as compared to in metalloproteins, for example.

Table 5.2-1 Published values of blind sphere radii in solid state NMR and DNP MAS NMR

Paramagnetic species	Techniques	Hosts or samples	NMR nuclei	r_0 / Å	Sample temperature/K	Field/T	MAS frequency/kHz	Reference
Trityl OX063	DNP MAS NMR		^{13}C	19	84	4.98	5	[61] SI
4-amino-TEMPO	DNP MAS NMR	d_8-glycerol/D_2O/H_2O +	^{13}C	21	84	4.98	5	[61] SI
TOTAPOL	DNP MAS NMR	^{13}C-urea, frozen solution	^{13}C	29	84	4.98	5	[61] SI
Gd-DOTA (S=7/2)	DNP MAS NMR		^{13}C	32	84	4.98	5	[61] SI
TMP-V-T[*]	DNP MAS NMR	dihydrofolate reductase	^{1}H	10.5	111±2.5	14.1	11	[64]
TOTAPOL	DNP MAS NMR	proline	^{1}H	10	101	9.4	8.889	[59]
TEMPOL	DNP MAS NMR	glycerol：H_2O 1：1 (v：v)	^{1}H	<10	100	9.4	static	[63]
Co(II)	soild state NMR	CoMMP-12[**]	^{13}C	9-10	280	20	22	[100,101]
Co(II)	soild state NMR	CoMMP-12	^{13}C	5.6	280	21.1	60	[100,101]
Cu(II)	soild state NMR	Cu^{2+}, Zn^{2+}-SOD[***]	^{13}C	5	348.15	16.44	15	[101,116]
Cu(II)	soild state NMR	Cu^{2+}, Zn^{2+}-SOD	^{1}H	10	286.15	19.9	60	[101,117]
Co(II)	soild state NMR	Co^{2+}-SOD	^{1}H	5	not specified	18.8	60	[101,118]

[*]TMP-V-T is a biradical with trimethoprim(TMP) covalently linked to TOTAPOL.[64]

[**]MMP-12 is matrix metalloproteinase 12. CoMMP-12 is Co(II) replaced catalytic domain of MMP-12, ZnMMP-12 is Zn(II) replaced, and so forth.

[***]SOD is superoxide dismutase.

Table 5.2-2 Published values of blind sphere radii in solution NMR

Paramagnetic species	Techniques	Hosts/samples	NMR nuclei	r_0 / Å	Sample temperature/K	Field/T	Reference
Gd(III)	solution NMR	^{Gd}CLaNP[*]	^{1}H	20±3	303	14.1	[27,119]
Yb(III)	solution NMR	^{Yb}CLaNP-3[*]	^{1}H	10	303	14.1	[27,119]
Tm(III)	solution NMR	CaTmCb protein[**]	^{1}H	15	300	21.1	[27,120]
Tm(III)	solution NMR	CaTmCb protein[**]	^{13}C	5	300	16.4	[27,120]
Tm(III)	solution NMR	CaTmCb protein[**]	^{15}N	4.2	300	9.4	[27,120]
Cu(II)	solution NMR	protein αB-crystallin	^{1}H	12	268	16.4	[60]
Cu(II)	solution NMR	protein αB-crystallin	^{13}C	6	268	16.4	[60]
Cu(II)	solution NMR	CopC[***]	^{1}H	11	298	16.4	[121,122]
Cu(II)	solution NMR	CopC[***]	^{13}C	6	298	16.4	[121,122]
Cu(II)	solution NMR	CopC[***]	^{15}N	5	298	16.4	[121,122]
Cu(II)	solution NMR	CopC[***]	^{13}C	4[****]	298	11.7	[121]
Cu(II)	solution NMR	CopC[***]	^{1}H	10	298	11.7	[123]
Cu(II)	solution NMR	Cu^{2+}, Zn^{2+}-SOD	^{1}H	10	298	21.1	[58,124]
Cu(II)	solution NMR	Cu^{2+}, Zn^{2+}-SOD	^{1}H	11.5	298	16.4	[124]
Cu(II)	solution NMR	Cu^{2+}, Zn^{2+}-SOD	^{13}C	<9	298	16.4	[124]

[*]CLaNP is short for caged lanthanide NMR probe, which is a caged DOTA-based (DOTA=1,4,7,10-tetraazacyclododecane-*N*,*N′*,*N″*,*N‴*-tetraacetic acid) lanthanide chelate that is attached to a protein through two disulfide bridges. The superscripts denote the type of lanthanide ions, for example ^{Gd}CLaNP and ^{Yb}CLaNP-3 correspond to Gd(III) and Yb(III), respectively.

**CaTmCb is thulium(III) substituted Calbindin D$_{9K}$, which is a di-calcium binding protein of 75 aminoacid. The substitution of the Tm(III) to the calcium(II) is at site II.
***CopC is a Cu(II)-binding protein.
****The ^{13}C signals 4 Å away from the copper(II) can be detected but only on condition that they do not experience Fermi contact contribution.

5.3 Blind or Wipeout? A Brief Overview on the Keywords, the History and the Future of the NMR Blind Spheres

In section 5.2, the results about blind spheres from different research fields such as metalloproteins, alloys and molecular magnets were compared with the results in this work. One may notice that different names or keywords were used in different works for the same concept that no NMR signal can be observed inside a volume around a paramagnetic center. For consistency the term "blind sphere" is adopted in this thesis, however, if one restricts oneself to single keyword it is highly possible that useful information is omitted. In addition, it is interesting to find out that the concept of blind sphere was originally developed in paramagnetically doped inorganic crystals, just as what were studied in this thesis. Based on these observations, the author decided to add a small final section 5.3 to the overall discussions, which includes all possible keywords that lead to publications in different fields, and a brief story of how this concept was historically developed as a side dish in the study of spin diffusion. In parallel, possible drawbacks on the previous and current blind sphere models have been discussed, which may enlighten future improvements on the theory. This section was intended to act as a small extra piece of information.

Table 5.3-1 summarized typical examples of different keywords for different research interests. In the studies of metalloproteins by solution NMR and DNP, the terms of "blind sphere" and "quenching/bleaching" are often used, as the blind sphere and the detectable paramagnetic effects (figure 5.2-1 and 5.2-2) are useful information for structure constrains.[27,58] For the studies of magnetisms in solids the terms "wipe-out/wipeout" and "critical radius" are used and the research

interests lean towards relaxation rate and temperature dependence, as such studies gives hint to the stripe order.[70] Yet there are more terminologies for the same concept, the keywords include but are not limited to "signal bleaching", "signal quenching", "bleaching effect", "bleached zone", "paramagnetic quenching", "paramagnetic bleaching" and so forth (references for each keyword see table 5.3-1).

It is interesting to see how the keywords "navigated" themselves into different research fields and even more intriguing to find the development of the idea of blind sphere in fact may portend this navigation.

Historically, the concept of blind sphere can be traced back, though indirectly, to the studies of nuclear relaxation caused by paramagnetic impurities in solids.[49,125–135] The research interest of these studies was about spin diffusion, which was pointed out as the means to transport nuclear energy to paramagnetic centers.[125] For this purpose, the shell-of-influence model was proposed, in order to give reference to the partitions of cases with different diffusion rates.[49,136]

Although the mathematical model of this thesis (section 3.1) was derived from the well-established shell-of-influence model[136] and its variations (also referred to as the sphere of influence model,[130] and modified versions were the single-center model[49] and one-paramagnetic-center approximation[134]), it should be made clear that the shells and the sphere mentioned in these models were in fact not the blind sphere in this thesis. The radii of the two shells related to the distance between paramagnetic species and NMR nuclei, and the average spacing between paramagnetic species, respectively.[136] Whereas the sphere of influence referred to a region in which only one paramagnetic center determines the total nuclear spin-lattice relaxation rate, and its radius R was the average separation of the paramagnetic centers.[49] In the model of this thesis, the blind sphere referred to a volume around a paramagnetic center, inside of which signals from all NMR nuclei are invisible, regardless of the invisibility reasons such as line broadening or shift.

Table 5.3-1 Examples of keywords and applications of the concept blind sphere.

Paramagnetic species	Techniques	Keywords	Related explanation	Reference
TOTAPOL	DNP MAS NMR, solution NMR	signal bleach, paramagnetic bleaching, blind zone	PRE, first shell contact shift	[64]
Gd-DOTA, 4-amino-TEMPO, TOTAPOL, Trityl OX063	DNP MAS NMR	quenching radius	dipolar relaxation, cross relaxation	[61] SI
SPIROPOL, TOTAPOL	DNP MAS NMR	paramagnetic quenching, signal quenching	relaxation	[62]
TOTAPOL	DNP MAS NMR	bleached volume, quench	PRE	[59]
Cu(II)	solution NMR	paramagnetic quenching, bleaching	PRE	[60]
Cu(II)	solution NMR	blind sphere	dipolar and Fermi contact relaxation	[121]
Er(III), Dy(III)	NMR, μ^+SR	wipeout effect	dipolar and Fermi contact relaxation	[69]
ferromagnetic clusters with Mn or Fe ions	NMR	wipeout effect, critical radius	dipolar relaxation	[96]
Single-ion magnet $[Er(W_5O_{18})_2]^{9-}$	NMR	wipe-out effect, critical radius	dipolar relaxation	[68]
cuprate superconductors $La_{1.875}Ba_{0.125}CuO_4$	NMR, NQR	wiped-out, wipeout	relaxation	[67]
antiferromagnetic molecular rings Cr_8Zn	NMR	wipe-out, critical radius	dipolar relaxation	[66]

A partially comparable radius was another parameter b_0, which was defined as "a radius about each paramagnetic center, inside of which the nuclei have such broadened resonance lines that their contributions to a measured signal are unobserved".[49] This definition made by Lowe and Tse[49] in 1968 might be a hint

of the first blind sphere prototype. It may be comparable to the critical radius[68,96] in those studies that attributed the wipeout effect to T_2 relaxation (see section 5.2). But why is this definition only partially comparable? Cautiously speaking it is because only the relaxation portion of blind sphere possibilities was emphasized. Indeed, most of the descriptions/definitions in the early models[49,129–131,134,136] gave prominence to relaxation, for example "a behavior of prohibiting neighboring nuclei from participating macroscopic relaxation",[131] with only rare exception case being stated as "shift out of the resonance line".[133] There was also study that suggested first-shell contact shifts may also contribute to the blind sphere,[64] which supports the definition of blind sphere in this thesis.

It must also be pointed out that in the very first publication (section 3.1) one sentence, which was an assumption for $Sr_{1-x}Eu_xH_2$, is not correct. The original text was: "the paramagnetic shift of atoms is the dominant reason why a nucleus becomes 'invisible' in the above sense, and we neglect the relaxation effects which can make the signal of a nucleus vanish in the dead time delay of the probehead". The reason is that Eu(II) has nearly isotropic magnetic susceptibility tensor (isoelectronic as Gd(III), $4f^7$ configuration) and relatively long electronic relaxation time, as discussed in section 3.2 as well as section 5.2. Therefore, the relaxation effects for $Sr_{1-x}Eu_xH_2$ should not be neglected. The importance of relaxation effects that can make the signal vanish in the dead time delay was addressed in the second manuscript about blind spheres (section 3.2).

In 1968 Lowe and Tse[49] gave a first definition of the radius to the invisible volume, but it is not until 1971 that the NMR terminology for this radius was clearly denominated — in two separate contributions from Giovannini and Punkkinen the size of the invisible volume was both described as the "wipe-out radius"[131,134]. Another name for the invisible volume was referred to as the "blind-zone" (figure 5.2-1),[58] however mainly after 21th century, possibly started by a publication on metalloproteins from Bertini.[58] As already discussed in section 5.2, the theoretical explanation for blind zone was mainly based on r^{-6} dependent dipolar relaxation, which leads to a mathematical convenience of treating the blind volume as a sphere, therefore it's also referred to as the blind sphere. In a

way the name "sphere" is misleading, because the shape of the invisible volume is not necessarily spherical. In rare case the blind zone can also be treated in other forms for example as a rod-shaped volume.[59]

The spherical treatment could be questionable because if shifts (potentially could be paramagnetic shift or Knight shift depending on systems) were also taken into account as possible contributions to blind sphere, the anisotropy and the angular dependence of the hyperfine interaction should be important. In addition, the border of blind sphere was assumed to be stiffly rectangular and discontinuous between the visible and invisible status, which helped simplify the mathematical treatment but was unrealistic. Furthermore, the spheres were treated as hard spheres and no mutual influence was possible. In section 3.1, it was also pointed out that this assumption might be questionable because of possibility of multiple interactions among different Eu(II) spheres, which could mutually cancel each other out. This question is partially answered by the experimental fact that no signal within the spectral window (100 kHz, same as series measurements for $La_{1-x}Ln_xPO_4$) was observed for $GdPO_4$. Another supportive experimental result is the co-doping study (section 3.4) that blind spheres of different dopants could be treated independently. However, further measurements on wider concentration range, on different dopants (for example transition metal ions instead of lanthanide ions) and at different temperatures should be done before jumping into certain conclusion and if necessary, the contributions from the multi-paramagnetic-centers[49] should be considered.

6   Conclusions

The aims of this work were to establish a novel NMR methodology for dopant distribution analysis, and to check whether the NMR determined doping homogeneity correlated to the material performance.

The main results of this thesis included the followings: a function ("visibility function") which allowed extracting the blind volume ("blind sphere radius") for a statistical doping scenario (section 3.1); the discussions on the relations between blind volumes for different lanthanide ions and NMR nuclei (section 3.2); the correlation of the doping homogeneity determined by NMR ("NMR homogeneity") and luminescence (section 3.3); and the development of an extended function for co-doped materials (section 3.4). Based on these results, it could be concluded that the developed NMR visibility method acts as a useful tool for doping homogeneity determination of paramagnetic ions.

The potential applications of this novel NMR methodology in the future may be in the following areas.

First of all, as doping homogeneity on Å to nm scale could be determined, such method may serve as a tool in the development of synthesis pathways which lead to less clustering and a more efficient use of lanthanides. Such methodology can be applied in principle in any systems with paramagnetic species and NMR nuclei.

Second possible application mainly relies on the simplicity of this approach. As majorly simple NMR experiments especially single pulsed measurements were used in this method, neither high restrictions on instrumental levels nor requirements on complicated computational calculations were required. Therefore, on condition of known blind sphere radius, in principle a single measurement point would be sufficient to determine doping homogeneity. For example, it is potentially interesting for industrial fast sample batch quality inspection and quality control regarding doping homogeneity, which avoids excessive consumption of dopants while ensuring the material property. In this way, it offers a potential solution for the rational utilization of RE elements.

Besides potential values in high throughput testing, this NMR method may be also interesting for scientific researches because it provides a better estimation of the critical doping level at which a sample becomes NMR blind. Additionally, whether a sample is NMR visible or NMR blind could be speculated or maybe even predicted without experimental measurements, which offers convenience for the choice of NMR model compounds. For example for a NMR research that aims at observing paramagnetic effect at high doping level, Sm(III) is a good choice because the blind sphere radius was estimated to be small.
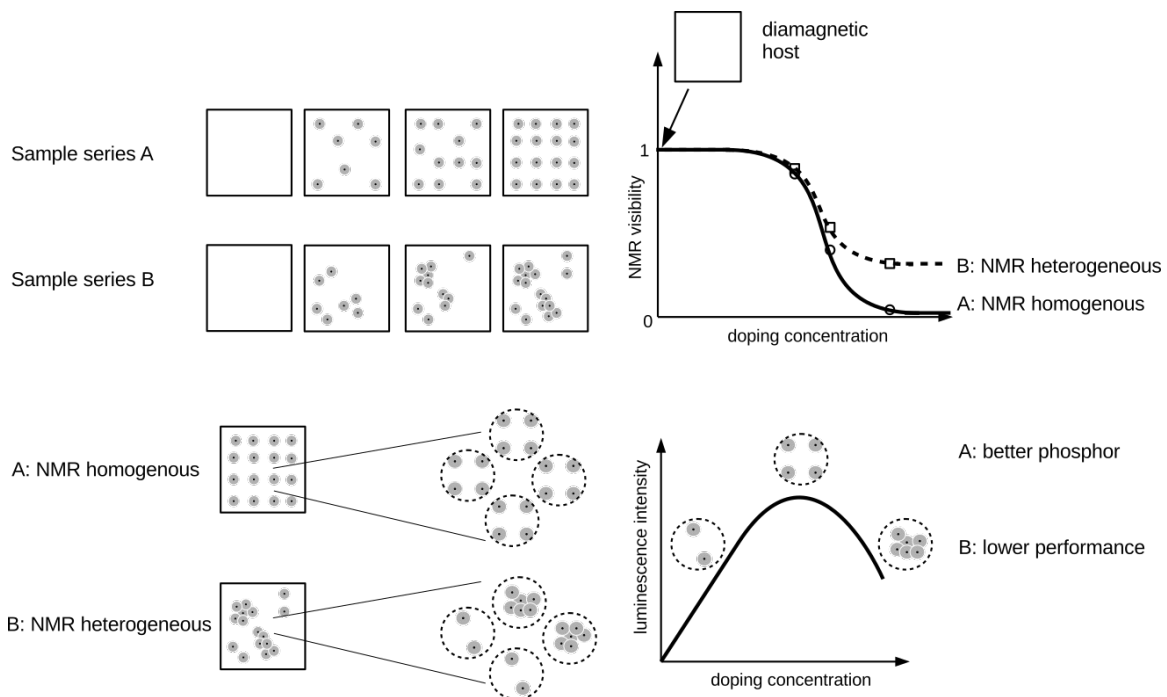
Figure 6.1: Schematic sketch demonstrating (1) how NMR visibility curves help to differentiate the homogeneous (i.e. random) doping scenario from the heterogeneous one that has clusters in this picture and (2) how the luminescence property of the two sample series should differ, because at the same doping level the heterogeneous sample contains clustering domains as well as deficient domains that show poorer luminescence performance. The gray circles around black points represent the blind spheres around paramagnetic centers. The dashed circles represent domains with different levels of doping homogeneity.

Bibliography

[1]   J. Maier, *Z. Anorg. Allg. Chem.* **2017**, *643*, 2083–2087.

[2]   J. Haber, *Pure Appl. Chem.* **1991**, *63*, 1227–1246.

[3]   J. Zhang, K. Tse, M. Wong, Y. Zhang, J. Zhu, *Front. Phys.* **2016**, *11*, 117405.

[4]   J. Lucas, P. Lucas, T. L. Mercier, A. Rollat, W. Davenport, *Rare Earths: Science, Technology, Production and Use*, Elsevier Inc., Amsterdam, **2014**.

[5]   V. Balaram, *Geosci. Front.* **2019**, *10*, 1285–1303.

[6]   B. Tansel, *Environ. Int.* **2017**, *98*, 35–45.

[7]   J. C. G. Bünzli, *Trends Chem.* **2019**, *1*, 751–762.

[8]   M. Bottrill, L. Kwok, N. J. Long, *Chem. Soc. Rev.* **2006**, *35*, 557–571.

[9]   K. Smith Stegen, *Energy Policy* **2015**, *79*, 1–8.

[10]   E. Apergis, N. Apergis, *Energy Econ.* **2017**, *62*, 33–42.

[11]   J. Zhou, J. L. Leaño, Z. Liu, D. Jin, K.-L. Wong, R.-S. Liu, J.-C. G. Bünzli, *Small* **2018**, *14*, 1801882.

[12]   T. Zhong, P. Goldner, *Nanophotonics* **2019**, *8*, 2003–2015.

[13]   H. Zhao, J. Xia, D. Yin, M. Luo, C. Yan, Y. Du, *Coord. Chem. Rev.* **2019**, *390*, 32–49.

[14]   J. A. Cotruvo, *ACS Cent. Sci.* **2019**, *5*, 1496–1506.

[15]   A. J. Kenyon, *Prog. Quant. Electron.* **2002**, *26*, 225–284.

[16]   M. J. F. Digonnet, *Rare-Earth-Doped Fiber Lasers and Amplifiers, Revised and Expanded*, CRC Press, Boca Raton, **2001**.

[17]   M. Sato, S. W. Kim, Y. Shimomura, T. Hasegawa, K. Toda, G. Adachi, *Handbook on the Physics and Chemistry of Rare Earths, Chapter 278 - Rare Earth-Doped Phosphors for White Light-Emitting Diodes*, Elsevier, Amsterdam, **2016**.

[18]   S. Massari, M. Ruberti, *Resour. Policy* **2013**, *38*, 36–43.

[19]   G. Charalampides, K. I. Vatalis, B. Apostoplos, B. Ploutarch-Nikolas, *Procedia Econ. Financ.* **2015**, *24*, 126–135.

[20]   N. Haque, A. Hughes, S. Lim, C. Vernon, *Resources* **2014**, *3*, 614–635.

[21]   S. Wen, J. Zhou, K. Zheng, A. Bednarkiewicz, X. Liu, D. Jin, *Nat. Commun.* **2018**, *9*, 1–12.

[22]   D. L. Dexter, J. H. Schulman, *J. Chem. Phys.* **1954**, *22*, 1063–1070.

[23]   H. G. Danielmeyer, M. Blätte, P. Balmer, *Appl. Phys.* **1973**, *1*, 269–274.

[24]   X. Li, R. Wang, F. Zhang, D. Zhao, *Nano Lett.* **2014**, *14*, 3634–3639.

[25]   A. Pilch, C. Würth, M. Kaiser, D. Wawrzyńczyk, M. Kurnatowska, S. Arabasz, K. Prorok, M. Samoć, W. Strek, U. Resch-Genger, et al., *Small* **2017**, *13*, 1701635.

[26]   H. Lueken, *Magnetochemie*, Vieweg+Teubner Verlag, Stuttgart/Leipzig, **1999**.

[27]   I. Bertini, C. Luchinat, G. Parigi, E. Ravera, *NMR of Paramagnetic Molecules: Applications to Metallobiomolecules and Models*, Elsevier Science, Amsterdam, **2016**.

[28]   A. J. Pell, G. Pintacuda, C. P. Grey, *Prog. Nucl. Magn. Reson. Spectrosc.* **2019**, *111*, 1–

271.

[29] W. Horwitz, *Pure Appl. Chem.* **1990**, *62*, 1193–1208.

[30] J. E. Shelby, *Introduction to Glass Science and Technology*, Royal Society Of Chemistry, London, **2005**.

[31] K. Hirota, J. P. Hill, S. M. Shapiro, G. Shirane, Y. Fujii, *Phys. Rev. B* **1995**, *52*, 13195–13205.

[32] F. Sidiroglou, A. Roberts, G. Baxter, *Rev. Sci. Instrum.* **2016**, *87*, 041501.

[33] R. Pantel, G. Servanton, *Transmission Electron Microscopy in Micro-Nanoelectronics*, John Wiley & Sons Ltd., Hoboken, **2013**.

[34] M. S. J. Marshall, D. T. Newell, D. J. Payne, R. G. Egdell, M. R. Castell, *Phys. Rev. B* **2011**, *83*, 035410.

[35] P. F. Smet, J. E. V. Haecke, D. Poelman, *J. Microsc.* **2008**, *231*, 1–8.

[36] L. I. D. J. Martin, D. Poelman, P. F. Smet, J. J. Joos, *ECS J. Solid State Sci. Technol.* **2017**, *7*, R3052.

[37] A. Hartridge, A. K. Bhattacharya, R. E. Dunin-Borkowski, J. L. Hutchison, *Journal of Nanoparticle Research* **2001**, *3*, 431–439.

[38] G. Servanton, R. Pantel, M. Juhel, F. Bertin, *Micron* **2009**, *40*, 543–551.

[39] H. Hantsche, *Scanning* **1989**, *11*, 257–280.

[40] T. Harazono, E. Yokota, H. Uchida, T. Watanabe, *Bull. Chem. Soc. Jpn.* **1998**, *71*, 2797–2805.

[41] T. Harazono, E. Yokota, H. Uchida, T. Watanabe, *Bull. Chem. Soc. Jpn.* **1998**, *71*, 825–829.

[42] T. Harazono, R. Adachi, N. Kijima, T. Watanabe, *Bull. Chem. Soc. Jpn.* **1999**, *72*, 2655–2664.

[43] A. C. Palke, J. F. Stebbins, L. A. Boatner, *Inorg. Chem.* **2013**, *52*, 12605–12615.

[44] R. J. McCarty, J. F. Stebbins, *Solid State Nucl. Magn. Reson.* **2016**, *79*, 11–22.

[45] Y. J. Lee, S.-H. Park, C. Eng, J. B. Parise, C. P. Grey, *Chem. Mater.* **2002**, *14*, 194–205.

[46] R. J. McCarty, J. F. Stebbins, *Solid State Nucl. Magn. Reson.* **2016**, *79*, 11–22.

[47] Y. J. Lee, C. P. Grey, *J. Phys. Chem. B* **2002**, *106*, 3576–3582.

[48] W. Huang, M. Schopfer, C. Zhang, R. C. Howell, B. A. Gee, L. C. Francesconi, T. Polenova, *J. Phys. Chem. B* **2006**, *110*, 12340–12350.

[49] I. J. Lowe, D. Tse, *Phys. Rev.* **1968**, *166*, 279–291.

[50] S. Maron, G. Dantelle, T. Gacoin, F. Devreux, *Phys. Chem. Chem. Phys.* **2014**, *16*, 18788–18798.

[51] S. Maron, N. Ollier, T. Gacoin, G. Dantelle, *Phys. Chem. Chem. Phys.* **2017**, *19*, 12175–12184.

[52] C. D'Agostino, P. Bräuer, *React. Chem. Eng.* **2019**, *4*, 268–272.

[53] W. Li, V. R. Celinski, J. Weber, N. Kunkel, H. Kohlmann, J. Schmedt auf der Günne,

Phys. Chem. Chem. Phys. **2016**, *18*, 9752–9757.

[54] W. Li, Q. Zhang, J. J. Joos, P. F. Smet, J. Schmedt auf der Günne, *Phys. Chem. Chem. Phys.* **2019**, *21*, 10185–10194.

[55] W. Li, M. Adlung, Q. Zhang, C. Wickleder, J. Schmedt auf der Günne, *ChemPhysChem* **2019**, *20*, 3245–3250.

[56] H. Deters, J. F. de Lima, C. J. Magon, A. S. S. de Camargo, H. Eckert, *Phys. Chem. Chem. Phys.* **2011**, *13*, 16071–16083.

[57] G. Galleani, C. Doerenkamp, S. Santagneli, C. J. Magon, A. S. S. de Camargo, H. Eckert, *J. Phys. Chem. C* **2019**, DOI 10.1021/acs.jpcc.9b10851.

[58] I. Bertini, C. Luchinat, G. Parigi, R. Pierattelli, *ChemBioChem* **2005**, *6*, 1536–1549.

[59] S. Lange, A. H. Linden, Ü. Akbey, W. Trent Franks, N. M. Loening, B.-J. van Rossum, H. Oschkinat, *J. Magn. Reson.* **2012**, *216*, 209–212.

[60] A. Mainz, B. Bardiaux, F. Kuppler, G. Multhaup, I. C. Felli, R. Pierattelli, B. Reif, *J. Biol. Chem.* **2012**, *287*, 1128–1138.

[61] B. Corzilius, L. B. Andreas, A. A. Smith, Q. Z. Ni, R. G. Griffin, *J. Magn. Reson.* **2014**, *240*, 113–123.

[62] E. Ravera, B. Corzilius, V. K. Michaelis, C. Luchinat, R. G. Griffin, I. Bertini, *J. Phys. Chem. B* **2014**, *118*, 2957–2965.

[63] A. J. P. Linde, S. Chinthalapalli, D. Carnevale, G. Bodenhausen, *Phys. Chem. Chem. Phys.* **2015**, *17*, 6415–6422.

[64] R. Rogawski, I. V. Sergeyev, Y. Zhang, T. H. Tran, Y. Li, L. Tong, A. E. McDermott, *J. Phys. Chem. B* **2017**, *121*, 10770–10781.

[65] G. Papavassiliou, M. Belesi, M. Fardis, C. Dimitropoulos, *Phys. Rev. Lett.* **2001**, *87*, 177204.

[66] F. Adelnia, A. Chiesa, S. Bordignon, S. Carretta, A. Ghirri, A. Candini, C. Cervetti, M. Evangelisti, M. Affronte, I. Sheikin, et al., *J. Chem. Phys.* **2015**, *143*, 244321.

[67] D. Pelc, H. J. Grafe, G. D. Gu, M. Požek, *Phys. Rev. B* **2017**, *95*, 054508.

[68] M. Mariani, F. Borsa, M. J. Graf, S. Sanna, M. Filibian, T. Orlando, K. P. V. Sabareesh, S. Cardona-Serra, E. Coronado, A. Lascialfari, *Phys. Rev. B* **2018**, *97*, 144414.

[69] E. Lucaccini, L. Sorace, F. Adelnia, S. Sanna, P. Arosio, M. Mariani, S. Carretta, Z. Salman, F. Borsa, A. Lascialfari, *Phys. Rev. B* **2019**, *100*, 174416.

[70] M. H. Julien, A. Campana, A. Rigamonti, P. Carretta, F. Borsa, P. Kuhns, A. P. Reyes, W. G. Moulton, M. Horvatić, C. Berthier, et al., *Phys. Rev. B* **2001**, *63*, 144508.

[71] M. H. Levitt, *Spin Dynamics: Basics of Nuclear Magnetic Resonance*, John Wiley & Sons, Chichester, **2008**.

[72] A. Abragam, *The Principles of Nuclear Magnetism*, Clarendon Press, Oxford, **1961**.

[73] K. Schmidt-Rohr, H. W. Spiess, *Multidimensional Solid-State NMR and Polymers*, Academic Press, San Diego, **2012**.

[74]   R. K. Harris, E. D. Becker, S. M. Cabral de Menezes, R. Goodfellow, P. Granger, *Pure Appl. Chem.* **2001**, *73*, 1795–1818.

[75]   R. K. Harris, E. D. Becker, S. M. Cabral de Menezes, P. Granger, R. E. Hoffman, K. W. Zilm, *Pure Appl. Chem.* **2008**, *80*, 59–84.

[76]   J. H. Van Vleck, *Phys. Rev.* **1948**, *74*, 1168–1183.

[77]   G. W. Parker, F. Lado, *Phys. Rev. B* **1973**, *8*, 3081–3092.

[78]   B. Herreros, A. W. Metz, G. S. Harbison, *Solid State Nucl. Magn. Reson.* **2000**, *16*, 141–150.

[79]   D. Jardón-Álvarez, J. Schmedt auf der Günne, *Solid State Nucl. Magn. Reson.* **2018**, *94*, 26–30.

[80]   J. D. Satterlee, *Concepts Magn. Reson.* **1990**, *2*, 119–129.

[81]   I. Solomon, *Phys. Rev.* **1955**, *99*, 559–565.

[82]   I. Solomon, N. Bloembergen, *J. Chem. Phys.* **1956**, *25*, 261–266.

[83]   N. Bloembergen, *J. Chem. Phys.* **1957**, *27*, 572–573.

[84]   N. Bloembergen, L. O. Morgan, *J. Chem. Phys.* **1961**, *34*, 842–850.

[85]   *Chemistry International -- Newsmagazine for IUPAC* **2005**, *27*, 25–26.

[86]   R. M. Hartshorn, K.-H. Hellwich, A. Yerin, T. Damhus, A. T. Hutton, *Pure Appl. Chem.* **2015**, *87*, 1039–1049.

[87]   B. Bleaney, *J. Magn. Reson.* **1972**, *8*, 91–100.

[88]   B. Bleaney, C. M. Dobson, B. A. Levine, R. B. Martin, R. J. P. Williams, A. V. Xavier, *J. Chem. Soc., Chem. Commun.* **1972**, *0*, 791b–7793.

[89]   A. Bhaumik, C. Luchinat, G. Parigi, E. Ravera, M. Rinaldelli, *CrystEngComm* **2013**, *15*, 8639–8656.

[90]   G. Cucinotta, M. Perfetti, J. Luzon, M. Etienne, P.-E. Car, A. Caneschi, G. Calvez, K. Bernot, R. Sessoli, *Angew. Chem. Int. Ed. Engl.* **2012**, *51*, 1606–1610.

[91]   M.-E. Boulon, G. Cucinotta, J. Luzon, C. Degl'Innocenti, M. Perfetti, K. Bernot, G. Calvez, A. Caneschi, R. Sessoli, *Angew. Chem. Int. Ed. Engl.* **2013**, *52*, 350–354.

[92]   I. Bertini, Y.-M. Lee, C. Luchinat, M. Piccioli, L. Poggi, *ChemBioChem* **2001**, *2*, 550–558.

[93]   I. Bertini, C. Luchinat, G. Parigi, R. Pierattelli, *Dalton Trans.* **2008**, *0*, 3782–3790.

[94]   I. Bertini, C. Luchinat, G. Parigi, *Coord. Chem. Rev.* **2011**, *255*, 649–663.

[95]   M.-H. Julien, A. Campana, A. Rigamonti, P. Carretta, F. Borsa, P. Kuhns, A. P. Reyes, W. G. Moulton, M. Horvatic, C. Berthier, et al., *Phys. Rev. B* **2001**, *63*, 144508.

[96]   M. Belesi, A. Lascialfari, D. Procissi, Z. H. Jang, F. Borsa, *Phys. Rev. B* **2005**, *72*, 014440.

[97]   N. Bloembergen, T. J. Rowland, *Acta Metall.* **1953**, *1*, 731–746.

[98]   D. A. Levitt, R. E. Walstedt, *Phys. Rev. Lett.* **1977**, *38*, 178–181.

[99]   A. W. Hunt, P. M. Singer, K. R. Thurber, T. Imai, *Phys. Rev. Lett.* **1999**, *82*, 4300–4303.

[100] I. Bertini, L. Emsley, M. Lelli, C. Luchinat, J. Mao, G. Pintacuda, *J. Am. Chem. Soc.*

2010, *132*, 5558–5559.

[101]   M. J. Knight, I. C. Felli, R. Pierattelli, L. Emsley, G. Pintacuda, *Acc. Chem. Res.* **2013**, *46*, 2108–2116.

[102]   N. Bloembergen, *J. Phys. Radium* **1962**, *23*, 658–664.

[103]   Y. Fukai, K. Watanabe, *Phys. Rev. B* **1970**, *2*, 2353–2360.

[104]   J. S. Galsin, *Impurity Scattering in Metallic Alloys*, Springer US, Boston, MA, **2002**.

[105]   P. L. Sagalyn, A. Paskin, R. J. Harrison, *Phys. Rev.* **1961**, *124*, 428–437.

[106]   K. R. Thurber, R. Tycko, *J. Chem. Phys.* **2014**, *140*, 184201.

[107]   H. Takahashi, C. Fernández-de-Alba, D. Lee, V. Maurel, S. Gambarelli, M. Bardet, S. Hediger, A.-L. Barra, G. De Paëpe, *Journal of Magnetic Resonance* **2014**, *239*, 91–99.

[108]   L. Martel, A. Rakhmatullin, J. J. Baldoví, M. Perfetti, K. Popa, M. Deschamps, T. Gouder, E. Colineau, A. Kovács, J.-C. Griveau, *Phys. Rev. B* **2019**, *100*, 054412.

[109]   P. Caravan, É. Tóth, A. Rockenbauer, A. E. Merbach, *J. Am. Chem. Soc.* **1999**, *121*, 10403–10409.

[110]   É. Tóth, L. Burai, A. E. Merbach, *Coordination Chemistry Reviews* **2001**, *216–217*, 363–382.

[111]   G. Han, Y. Deng, J. Sun, J. Ling, Z. Shen, *Exp. Ther. Med.* **2015**, *9*, 1561–1566.

[112]   L. A. Basal, M. D. Bailey, J. Romero, M. M. Ali, L. Kurenbekova, J. Yustein, R. G. Pautler, M. J. Allen, *Chem. Sci.* **2017**, *8*, 8345–8350.

[113]   M. N. Brekhovskikh, S. P. Solodovnikov, L. V. Moiseeva, I. A. Zhidkova, V. A. Fedorov, *Inorg. Mater.* **2018**, *54*, 713–715.

[114]   R. D. Shannon, *Acta. Cryst. A* **1976**, *32*, 751–767.

[115]   M. M. Abraham, L. A. Boatner, Y. Chen, J. L. Kolopus, R. W. Reynolds, *Phys. Rev. B* **1971**, *4*, 2853–2857.

[116]   G. Pintacuda, N. Giraud, R. Pierattelli, A. Böckmann, I. Bertini, L. Emsley, *Angew. Chem., Int. Ed.* **2007**, *46*, 1079–1082.

[117]   M. J. Knight, A. J. Pell, I. Bertini, I. C. Felli, L. Gonnelli, R. Pierattelli, T. Herrmann, L. Emsley, G. Pintacuda, *PNAS* **2012**, *109*, 11095–11100.

[118]   M. J. Knight, I. C. Felli, R. Pierattelli, I. Bertini, L. Emsley, T. Herrmann, G. Pintacuda, *J. Am. Chem. Soc.* **2012**, *134*, 14730–14733.

[119]   M. D. Vlasie, C. Comuzzi, A. M. C. H. van den Nieuwendijk, M. Prudêncio, M. Overhand, M. Ubbink, *Chem. Eur. J.* **2007**, *13*, 1715–1723.

[120]   S. Balayssac, B. Jiménez, M. Piccioli, *J Biomol NMR* **2006**, *34*, 63–73.

[121]   W. Bermel, I. Bertini, I. C. Felli, R. Kümmerle, R. Pierattelli, *J. Am. Chem. Soc.* **2003**, *125*, 16423–16429.

[122]   F. Arnesano, L. Banci, I. Bertini, I. C. Felli, C. Luchinat, A. R. Thompsett, *J. Am. Chem. Soc.* **2003**, *125*, 7200–7208.

[123]   F. Arnesano, L. Banci, I. Bertini, S. Mangani, A. R. Thompsett, *PNAS* **2003**, *100*, 3814–

3819.

[124] I. Bertini, I. C. Felli, C. Luchinat, G. Parigi, R. Pierattelli, *ChemBioChem* **2007**, *8*, 1422–1429.

[125] N. Bloembergen, *Physica* **1949**, *15*, 386–426.

[126] A. Abragam, *Phys. Rev.* **1955**, *98*, 1729–1735.

[127] W. E. Blumberg, *Phys. Rev.* **1960**, *119*, 79–84.

[128] H. E. Rorschach Jr., *Physica* **1964**, *30*, 38–48.

[129] G. R. Khutsishvili, *Sov. Phys. Usp.* **1966**, *8*, 743.

[130] G. R. Khutsishvili, *Sov. Phys. Usp.* **1969**, *11*, 802.

[131] B. Giovannini, P. Pincus, G. Gladstone, A. J. Heeger, *J. Phys. Colloq.* **1971**, *32*, C1-163-C1-171.

[132] J. I. Kaplan, *Phys. Rev. B* **1971**, *3*, 604–608.

[133] M. R. McHenry, B. G. Silbernagel, J. H. Wernick, *Phys. Rev. Lett.* **1971**, *27*, 426–429.

[134] M. Punkkinen, *Phys. kondens. Materie.* **1971**, *13*, 79–88.

[135] H. A. P Bernier, *J. Phys. F: Met. Phys.* **1973**, *3*, 869.

[136] T. J. Schmugge, C. D. Jeffries, *Phys. Rev.* **1965**, *138*, A1785–A1801.

Appendix

The Fortran90 code used in the section 3.1 for $Sr_{0.995}Eu_{0.005}H_2$ is shown as an example in this appendix. The simulation of other systems such as $La_{1-x}Ln_xPO_4$ required adapting the code to different crystal structure.

The example for $Sr_{0.995}Eu_{0.005}H_2$ consists the following files: Makefile, SrH2_0.5percent.f90, mod_ATOM_TYPE.f90, mod_SHIFT_TYPE.f90, mod_RANG_COUNTER.f90, distance.f90, sub_random.f90 and unitcell_atom12.txt, which is a text file with crystallographic information of the host lattice.

Makefile

GNUmakefile to build and execute ACML example programs

F90 := gfortran

FLINK := $(F90)

FFLAGS := -m64 -lrt -O3

#-g for debugging, -O3 for optimization

FLINKFLAGS :=

FLINKLIBS :=

obj := o

.SUFFIXES: .f .$(obj) .exe

all: SrH2_0.5percent

Source code of F90 programs

SOURCE := mod_ATOM_TYPE.o mod_SHIFT_TYPE.o distance.o sub_random.o mod_RANGE_COUNTER.o SrH2_0.5percent.o

mod_ATOM_TYPE.o:mod_ATOM_TYPE.f90

    $(F90) $(FFLAGS) -c mod_ATOM_TYPE.f90

mod_SHIFT_TYPE.o:mod_SHIFT_TYPE.f90

    $(F90) $(FFLAGS) -c mod_SHIFT_TYPE.f90

mod_RANGE_COUNTER.o:mod_RANGE_COUNTER.f90

    $(F90) $(FFLAGS) -c mod_RANGE_COUNTER.f90

distance.o:distance.f90

    $(F90) $(FFLAGS) -c distance.f90

sub_random.o:sub_random.f90

    $(F90) $(FFLAGS) -c sub_random.f90

SrH2_0.5percent.o:SrH2_0.5percent.f90

    $(F90) $(FFLAGS) -c SrH2_0.5percent.f90

SrH2_0.5percent: $(SOURCE)

    $(F90) $(FFLAGS) -o SrH2_0.5percent.exe $(SOURCE) $(FLINKLIBS)

clean:

```
    rm -f $(SOURCE)

    rm -f atom_type_module.mod

    rm -f ATOM_TYPE_module.o

    rm -f SHIFT_TYPE_module.o

    rm -f shift_type_module.mod

    rm -f sub_random.o

    rm -f mod_RANGE_COUNTER.o

    rm -f range_counter_module.mod

    rm -f SrH2_0.5percent.exe

    rm -f SrH2_0.5percent.o
```

SrH2_0.5percent.f90

```
PROGRAM SrH2_05percent

USE ATOM_TYPE_module

USE SHIFT_TYPE_module

USE RANGE_COUNTER_module

IMPLICIT NONE

INTEGER :: I, J, M, N  ! variable without real meaning

INTEGER, ALLOCATABLE, DIMENSION(:) :: dummy  ! variable without real meaning

INTEGER :: IOstatus

INTEGER :: N_loop  ! number of calling RANGE_COUNTER

INTEGER :: N_cut ! calculate the sdv using results from loops after N_cut

INTEGER :: size_range

INTEGER, POINTER, DIMENSION(:) :: COUNT_RESULT

INTEGER, ALLOCATABLE, DIMENSION (:,:) :: BLA  ! result from a single loop

DOUBLE PRECISION, ALLOCATABLE, DIMENSION(:,:) :: AVE  ! average from loops

DOUBLE PRECISION, ALLOCATABLE, DIMENSION(:) :: SUM_AVE, MEAN

DOUBLE PRECISION, ALLOCATABLE, DIMENSION(:) :: SUM_DEV, STANDARD_DEV

CALL RANGE_COUNTER(COUNT_RESULT,size_range)

! number of loops is adjustable

N_loop = 6000

ALLOCATE(BLA(N_loop,size_range))

ALLOCATE(AVE(N_loop,size_range))

ALLOCATE(dummy(size_range))

! define the 1st values
```

```fortran
   BLA(1,:) = COUNT_RESULT

   AVE(1,:) = DBLE(BLA(1,:))

   dummy = BLA(1,:)

! start calling and looping

DO I = 2, N_loop

!   PRINT *, "Now we are in loop number", I

   CALL RANGE_COUNTER(COUNT_RESULT,size_range)

     BLA(I,:) = COUNT_RESULT

   DO J = 1, size_range

     dummy(J) = dummy(J) + BLA(I,J)

     AVE(I,:) = DBLE(DBLE(dummy(:))/I)

   END DO

END DO

ALLOCATE(SUM_AVE(size_range))

ALLOCATE(MEAN(size_range))

ALLOCATE(SUM_DEV(size_range))

ALLOCATE(STANDARD_DEV(size_range))

N_cut=N_loop*4/5

OPEN(988, FILE="stdev_05percent.txt")

DO J= 1, size_range

SUM_AVE(J)=SUM(AVE(N_cut:N_loop,J), DIM=1)

MEAN(J) = DBLE(SUM_AVE(J)/(N_loop-N_cut+1))

END DO

DO J=1,size_range

   WRITE(988,*) "sum ave", SUM_AVE(J)

   WRITE(988,*) "mean", MEAN(J)

END DO

DO I = N_cut, N_loop

DO J=1,size_range

  SUM_DEV(J) = (AVE(I,J)-MEAN(J))**2 + SUM_DEV(J)

END DO

END DO

DO J = 1, size_range

    STANDARD_DEV(J) = DBLE(SQRT(SUM_DEV(J)/(N_loop-N_cut)))

END DO

DO J=1,size_range
```

```
   WRITE(988,*) "standard deviation", STANDARD_DEV(J)

END DO

CLOSE (988)

OPEN (789, FILE = "result_loops.txt")

DO I = 1, N_loop

WRITE (789,*) "BLA", BLA(I,:)

END DO

DO I=1, N_loop

WRITE (789,*) "AVE", AVE(I,:)

END DO

CLOSE (789)

DEALLOCATE(COUNT_RESULT)

DEALLOCATE(BLA)

DEALLOCATE(AVE)

DEALLOCATE(dummy)

DEALLOCATE(SUM_AVE)

DEALLOCATE(MEAN)

DEALLOCATE(SUM_DEV)

DEALLOCATE(STANDARD_DEV)

END PROGRAM SrH2_05percent
```

mod_ATOM_TYPE

```
MODULE ATOM_TYPE_module

PRIVATE

PUBLIC :: ATOM_TYPE !,UnitCellAtoms

TYPE ATOM_TYPE

   CHARACTER (len=5) :: site_symbol

   DOUBLE PRECISION :: x,y,z

   INTEGER :: site_id

END TYPE ATOM_TYPE

END MODULE ATOM_TYPE_module
```

mod_SHIFT_TYPE.f90

```
MODULE SHIFT_TYPE_module

USE ATOM_TYPE_module

PRIVATE
```

PUBLIC :: SHIFT_TYPE

TYPE SHIFT_TYPE

   INTEGER :: ax, by, cz ! Box Origin

   TYPE(ATOM_TYPE), ALLOCATABLE, DIMENSION (:) :: SrAtomPos

END TYPE SHIFT_TYPE

END MODULE SHIFT_TYPE_module

mod_RANGE_COUNTER

MODULE RANGE_COUNTER_module

PRIVATE

PUBLIC :: RANGE_COUNTER

CONTAINS

SUBROUTINE RANGE_COUNTER(COUNT_RESULT,size_range)

USE ATOM_TYPE_module

USE SHIFT_TYPE_module

IMPLICIT NONE

INTEGER :: I, J, M, N, SA, SB, SC ! variables with no real meanings

INTEGER :: IOstatus

CHARACTER(LEN=50):: buffer ! variables with no real meanings

REAL :: random

DOUBLE PRECISION :: dummydistance

DOUBLE PRECISION, ALLOCATABLE, DIMENSION(:) :: dummy_min_distance

INTEGER :: Nr_UnitCellAtoms

INTEGER :: Nr_atoms ! total number of all atoms

INTEGER :: Nr_boxes ! total number of shifted unit cells

INTEGER :: BoxNr

INTEGER :: Nr_BoxesXDimension=41 !adjust the number to have more boxes in X

INTEGER :: Nr_BoxesYDimension=67 !adjust the number to have more boxes in Y

INTEGER :: Nr_BoxesZDimension=35 !adjust the number to have more boxes in Z

INTEGER :: Nr_H_unitcell ! number of H atoms inside unit cell

INTEGER :: Nr_Sr_unitcell ! number of Sr atoms inside unit cell

INTEGER :: Nr_Sr   ! number of all Sr atoms

INTEGER :: Nr_Eu   ! = Eu Nr given by calling random

INTEGER :: Nr_Eu_ideal ! = doping concentration * total Sr Nr

INTEGER :: Nr_Eu_around_H = 10 ! number of nearest neighbour Eu atoms per H atom

DOUBLE PRECISION :: doping = 0.0050d0 ! doping concentration of Eu

```fortran
DOUBLE PRECISION, ALLOCATABLE, DIMENSION(:,:) :: min_distance

INTEGER :: range_min = 2 ! define the min of interested distance range

INTEGER :: range_max = 32 ! define the max of interested distance range

INTEGER :: size_range

INTEGER :: d_range

INTEGER, ALLOCATABLE, DIMENSION(:,:) :: RANGE_COUNT

INTEGER, POINTER, DIMENSION(:) :: COUNT_RESULT

! from functions

DOUBLE PRECISION :: distance

! from TYPE modulse

TYPE(ATOM_TYPE), ALLOCATABLE, DIMENSION (:) :: UnitCellAtoms

TYPE(SHIFT_TYPE), ALLOCATABLE, DIMENSION(:) :: box

TYPE(ATOM_TYPE), ALLOCATABLE, DIMENSION (:) :: H_unitcell

TYPE(ATOM_TYPE), ALLOCATABLE, DIMENSION (:) :: Sr_unitcell

!TYPE(ATOM_TYPE), ALLOCATABLE, DIMENSION (:) :: Sr_atoms

TYPE(ATOM_TYPE), ALLOCATABLE, DIMENSION (:) :: Eu_atoms

!read unit cell fractional coordinates from list

Nr_UnitCellAtoms=0

PRINT *, "start reading unitcell info"

OPEN (001, file="unitcell_atom12.txt", ACCESS="SEQUENTIAL", status="OLD",&
    BLANK="NULL", POSITION="ASIS", action="read", IOSTAT=IOstatus)

DO WHILE (IOstatus==0)
  READ (001,*,IOSTAT=IOstatus) buffer

! count the number of atoms in the unit cell

IF (IOstatus==0) THEN
  Nr_UnitCellAtoms=Nr_UnitCellAtoms+1

END IF

END DO

PRINT *, "number of atoms in unit cell", Nr_UnitCellAtoms

ALLOCATE(UnitCellAtoms(Nr_UnitCellAtoms))

REWIND 001

DO I=1, Nr_UnitCellAtoms

READ (001,*) UnitCellAtoms(I)%site_symbol, &
    UnitCellAtoms(I)%x, UnitCellAtoms(I)%y, UnitCellAtoms(I)%z, &
    UnitCellAtoms(I)%site_id

END DO
```

```
CLOSE (001)

PRINT *, "Unit Cell Atoms read in"

! total number of atoms in the big box can be calculated from shift units

!PRINT *, Nr_atoms

Nr_boxes=(Nr_BoxesXDimension*2+1)*&

      (Nr_BoxesYDimension*2+1)*&

      (Nr_BoxesZDimension*2+1)

Nr_atoms=Nr_boxes*SIZE(UnitCellAtoms)

PRINT *, Nr_boxes

PRINT *, Nr_atoms

! count the total number of H atoms inside the unit cell

Nr_H_unitcell = 0

DO I=1, SIZE(UnitCellAtoms)

  IF (UnitCellAtoms(I)%site_symbol=="H1" .OR. &

    UnitCellAtoms(I)%site_symbol=="H2")  THEN

        Nr_H_unitcell =  Nr_H_unitcell + 1

  END IF

END DO

PRINT *, Nr_H_unitcell

! create array of H atoms inside unit cell from UnitCellAtoms

ALLOCATE (H_unitcell(Nr_H_unitcell))

Nr_H_unitcell = 0

DO I=1, SIZE(UnitCellAtoms)

  IF (UnitCellAtoms(I)%site_symbol=="H1" .OR. &

    UnitCellAtoms(I)%site_symbol=="H2")  THEN

    Nr_H_unitcell =  Nr_H_unitcell + 1

    H_unitcell(Nr_H_unitcell)=UnitCellAtoms(I)

  END IF

END DO

! count the number of Sr atoms inside unit cells

Nr_Sr_unitcell = 0

DO I=1, SIZE(UnitCellAtoms)

  IF (UnitCellAtoms(I)%site_symbol=="Sr")  THEN

        Nr_Sr_unitcell =  Nr_Sr_unitcell + 1

  END IF

END DO
```

```fortran
PRINT *, Nr_Sr_unitcell

! create array of Sr atoms inside unit cell from UnitCellAtoms

ALLOCATE (Sr_unitcell(Nr_Sr_unitcell))

Nr_Sr_unitcell = 0

DO I=1, SIZE(UnitCellAtoms)

  IF (UnitCellAtoms(I)%site_symbol=="Sr")  THEN

     Nr_Sr_unitcell =  Nr_Sr_unitcell + 1

     Sr_unitcell(Nr_Sr_unitcell)=UnitCellAtoms(I)

  END IF

END DO

!BoxNr is the identifier of each small "box" (shifted unit cell)

BoxNr=0

PRINT *, "start creating Sr atoms list!"

! create a permanent list of all Sr atom positions

ALLOCATE (box(Nr_Boxes))

 DO I=1,Nr_boxes

    ALLOCATE(box(I)%SrAtomPos(Nr_Sr_unitcell))

 END DO

DO  SA= -Nr_BoxesXDimension, Nr_BoxesXDimension

  DO  SB=-Nr_BoxesYDimension, Nr_BoxesYDimension

    DO  SC=-Nr_BoxesZDimension, Nr_BoxesZDimension

      BoxNr=BoxNr+1

       box(BoxNr)%ax = SA

       box(BoxNr)%by = SB

       box(BoxNr)%cz = SC

      ! Now follows an ARRAY-assignment

       box(BoxNr)%SrAtomPos%site_symbol=Sr_unitcell%site_symbol

       box(BoxNr)%SrAtomPos%site_id=Sr_unitcell%site_id

       box(BoxNr)%SrAtomPos%x=Sr_unitcell%x+SA

       box(BoxNr)%SrAtomPos%y=Sr_unitcell%y+SB

       box(BoxNr)%SrAtomPos%z=Sr_unitcell%z+SC

    END DO

  END DO

END DO

PRINT *, BoxNr

PRINT *, "atom list created!"
```

```
DEALLOCATE(Sr_unitcell)

Nr_Eu_ideal = INT(CEILING(doping * Nr_atoms/3))

Nr_Sr = Nr_atoms/3

PRINT *, Nr_Eu_ideal

! count the real Nr_Eu

Nr_Eu = 0

PRINT *, "start creating Eu atoms!"

ALLOCATE(Eu_atoms(Nr_Sr))
  DO I=1, Nr_boxes
    DO J=1, SIZE(box(1)%SrAtomPos)
        CALL INIT_RANDOM_SEED()
        CALL RANDOM_NUMBER(random)
        IF (random<=doping) THEN
          !box(I)%SrAtomPos(J)%site_symbol="Eu"
           Nr_Eu = Nr_Eu +1
           Eu_atoms(Nr_Eu) = box(I)%SrAtomPos(J)
           ! Sr_atoms(Nr_Eu)= box(I)%SrAtomPos(J)
           !ELSE IF (random>doping) THEN
           ! box(I)%AtomPos(J)%site_symbol="Sr"
        END IF
    END DO
  END DO
PRINT *, "real Eu number", Nr_Eu

PRINT *, "ideal Eu number", Nr_Eu_ideal

PRINT *, "start calculating distance Eu-H"

! create a list of min distance of Eu-H for each H atoms in unit cell

OPEN (1234, FILE ="min_distancelist.txt")

PRINT *, Nr_Eu_around_H

ALLOCATE (min_distance(SIZE(H_unitcell),Nr_Eu_around_H))

min_distance=HUGE(min_distance(1,1))

ALLOCATE (dummy_min_distance(Nr_Eu_around_H))

dummy_min_distance=HUGE(dummy_min_distance(1))

DO I = 1, SIZE(H_unitcell)
  DO J = 1, Nr_Eu
    ! use distance function
    dummydistance=distance(H_unitcell(I),Eu_atoms(J))
```

```fortran
        IF (dummydistance<MAXVAL(min_distance(I,:))) THEN

          min_distance(I,MAXLOC(min_distance(I,:))) = dummydistance

        END IF

      END DO

      dummy_min_distance=min_distance(I,:)

      WRITE (1234,*) "10 min distance for H", I
!SORT Eu-distances  per H-Atom according to size
      DO M=1,Nr_Eu_around_H

        DO N=M,Nr_Eu_around_H

          IF(dummy_min_distance(N)<dummy_min_distance(M)) THEN

            dummydistance=dummy_min_distance(M) ! store M to dummy

            dummy_min_distance(M)=dummy_min_distance(N) ! write N to M

            dummy_min_distance(N)=dummydistance ! write dummy (M) TO N

          END IF

        END DO

      END DO

      WRITE (1234,*) min_distance(I, 1:10)

2222 END DO

CLOSE (1234)

DEALLOCATE(box)

DEALLOCATE(Eu_atoms)

DEALLOCATE(UnitCellAtoms)

DEALLOCATE(dummy_min_distance)

PRINT *, "start range counter"

PRINT *, "number of nearest Eu we calculated here for each H" ,Nr_Eu_around_H

PRINT *, "min Eu-H of all = ", MINVAL(min_distance)

size_range = range_max-range_min+1

PRINT *, size_range

ALLOCATE (RANGE_COUNT(SIZE(H_unitcell),size_range))

RANGE_COUNT = 0

OPEN (189, FILE = "result_semi.txt")

DO I = 1, SIZE(H_unitcell)

  DO d_range = range_min, range_max

    IF (MINVAL(min_distance(I,:))<=d_range) THEN

      RANGE_COUNT(I,(d_range-range_min+1)) = 1

    END IF
```

```
    END DO
    WRITE(189,*)  RANGE_COUNT(I,:)
END DO
WRITE(189,*)  SUM(RANGE_COUNT,DIM=1)
CLOSE (189)
ALLOCATE(COUNT_RESULT(size_range))
COUNT_RESULT=SUM(RANGE_COUNT,DIM=1)
DEALLOCATE (H_unitcell)
DEALLOCATE (RANGE_COUNT)
DEALLOCATE (min_distance)
END SUBROUTINE RANGE_COUNTER
END MODULE RANGE_COUNTER_module
```

distance.f90

```
DOUBLE PRECISION FUNCTION distance(atoms1,atoms2)
USE ATOM_TYPE_module
IMPLICIT NONE
TYPE (ATOM_TYPE) :: atoms1,atoms2
DOUBLE PRECISION :: a, b, c
a=6.3540d0
b=3.8540d0
c=7.2860d0
distance=SQRT(((atoms1%x-atoms2%x)*a)**2+((atoms1%y-atoms2%y)*b)**2+((atoms1%z-atoms2%z)*c)**2)
RETURN
END FUNCTION distance
```

sub_random.f90

The sub_random.f90 was adopted from the RANDOM_SEED in the online documentation of the GNU Fortran compiler (Copyright (C) Free Software Foundation, Inc., https://gcc.gnu.org/), from which the verbatim copying and distribution is permitted provided the notice of copyright is preserved.

unitcell_atom12.txt

```
H1  0.64484       0.25000          0.92759          1
```

H1	0.85516	0.75000	0.42759	2
H1	0.14484	0.25000	0.57241	3
H1	0.35516	0.75000	0.07241	4
H2	0.97365	0.75000	0.82183	5
H2	0.52635	0.25000	0.32183	6
H2	0.02635	0.25000	0.17817	7
H2	0.47365	0.75000	0.67817	8
Sr	0.76083	0.25000	0.61070	9
Sr	0.23917	0.75000	0.38930	10
Sr	0.26083	0.25000	0.88930	11
Sr	0.73917	0.75000	0.11070	12